
High resolution temperature observations to identify different runoff processes.
Martijn Westhoff

High resolution temperature observations to identify different runoff processes

Martijn Westhoff

High resolution temperature observations to identify different runoff processes

Proefschrift

ter verkrijging van de graad van doctor
aan de Technische Universiteit Delft,
op gezag van de Rector Magnificus prof.ir. K.C.A.M. Luyben,
voorzitter van het College voor Promoties,

in het openbaar te verdedigen op maandag 10 oktober 2011 om 15:00 uur

door

Martijn Carel WESTHOFF

civiel ingenieur
geboren te Zwolle.

Dit proefschrift is goedgekeurd door de promotor:
Prof. dr. ir. **H.H.G. Savenije**

Copromotor: Dr. **T.A. Bogaard**

Samenstelling promotiecommissie:
Rector Magnificus, *voorzitter*
Prof. dr. ir. **H.H.G. Savenije**, *Technische Universiteit Delft, promotor*
Dr. **T.A. Bogaard**, *Technische Universiteit Delft, copromotor*
Prof. dr. **E. Zehe**, *Karlsruher Institut für Technologie, Duitsland*
Prof. dr. ir. **R. Uijlenhoet**, *Universiteit Wageningen*
Prof. dr. **S. Uhlenbrook**, *Technische Universiteit Delft en UNESCO-IHE*
Dr. **S. Krause**, *Keele University, Verenigd Koninkrijk*
Prof. dr. ir. **N.C. van de Giesen**, *Technische Universiteit Delft*
Prof. dr. ir. **T.N. Olsthoorn**, *Technische Universiteit Delft*, reservelid

The research described in this dissertation was performed at the Water Resources Section, Faculty of Civil Engineering and Geosciences, Delft University of Technology. This research is partly funded by Delft Cluster, the Netherlands.

ISBN: 978-94-6182-025-9
Dataset doi:10.4121/uuid:57acdc8d-5c86-478a-9ada-c075cc30b0a

Keywords: DTS, stream water temperature, energy balance modelling, hyporheic exchange

"Nothing tends so much to the advancement of knowledge as the application of a new instrument"

Sir Humphry Davy (1778-1829)

Preface

On June 30, 2011, I abandoned the Maisbich: a small stream in Central Luxembourg where I performed most of my fieldwork. In the six years I worked there, I got to know the stream intimately. I have seen the course of the stream change during large storm events; I have seen the stream completely dry in summer; I have been there when the catchment was covered with snow; I hated the hundreds of flies buzzing around my head in the blazing heat and I cursed the stinging nettles and blackberry bushes that left scratches on my face. But the scratches and flies will be soon forgotten, leaving only sweet memories about the Maisbich: the stream I always talked about as "My Stream".

Although I started my fieldwork in the Maisbich in 2005, my first acquaintance with science was two years earlier. During spring 2003, I spent a couple of days in Luxembourg for my BSc thesis. Until that moment, I thought of scientists as people in white coats dripping fluids in tubes, worrying about the sixth digit behind the dot. But during these few days in Luxembourg, I noticed that, at least in hydrology, this was different. I witnessed the installation of a weir in a small stream, where a large plastic sheet was buried to in order to let most of the water pass over the weir. The supervisor explained that with an uncertainty of 10% it would offer excellent measurements. That made me realize that science was not about the sixth digit behind the dot, but that it was about understanding processes and quantifying them as good as possible.

Still it took until my MSc thesis before my scientific mindset was really triggered. Trying to do hydrograph separation based on natural tracers, I realized that the assumption of conservative tracer concentrations was always violated in this stream. Given this fact, Jeff McDonnell suggested to use temperature as a tracer instead. Temperature is also not conservative, but it was much easier to collect than the samples that had to be taken for other tracers. Shortly after I start working on temperature as tracer, John Selker crossed my path with a fibre optic cable that could measure temperature. This - for hydrology - new measurement technique, could measure temperature not only at high temporal resolution, but also at high spatial resolution. Soon the decision was made: we would try this new technique during a full week in the Maisbich as part of my MSc thesis. This tryout appeared to be very successful with three scientific publications as a result. This was my introduction to the hydrological scientific community.

But hydrology is more than just measuring something. The data should be analyzed and interpreted while modelling is often needed to distinguish between different processes that make

up the measured quantity. What is often said about creativity also counts for science: 10% is inspiration and 90% is perspiration. In my case, the new measurement technique could be seen as the inspiration, and the extensive fieldwork, the analysis and interpretation of the data combined with energy balance modelling as the perspiration. This is exactly what I did during my PhD: I measured stream water temperature, analyzed the large quantity of data, interpreted it and built a temperature model to cut down the signal into different processes that influence in-stream temperature. The effort of four years of work resulted in this dissertation.

Summary

Headwater catchments are important contributors to streamflow. They are small, but all combined they influence river flow significantly. To be able to make proper runoff predictions under different climate conditions and changing land use, it is important to have detailed understanding of the discharge processes in the headwater catchments.

In this thesis we explore the possibilities of fibre optic Distributed Temperature Sensing (DTS) to obtain more insight in temporal and spatial discharge dynamics during stormflow. DTS is a technique capable of measuring temperature with high spatial and temporal resolution. It was developed in the 1980's by the oil industry but only recently (in 2006) it has been introduced into the field of hydrology. The technique relies on short laser pulses that are sent through a fibre optic cable. Throughout the fibre optic cable small parts of the pulses are reflected by disturbances in the glass fibre, of which the exact position is obtained by measuring the travel time of the reflected light. The frequency shifts of the reflected light are then used to calculate the temperature of the fibre optic cable at the point of reflection. The DTS system used in this thesis has a spatial resolution of 2 m and a temporal resolution of 3 min. With these settings a precision of $\sim$0.1°C is obtained.

All experiments described in this thesis were done in the Maisbich: a 565 m long, first order stream in Central Luxembourg. The lithology of the Maisbich consists of schist which is covered with a layer of loose rock clasts with variable clay content of a few meters thick and a thin layer of fine sediments. Summer baseflow in the Maisbich can be <1 l s^{-1}, while the annual maximum discharge is in the order of 50-100 l s^{-1}. The stream reach has six distinct sources and two areas of significant infiltration losses.

In order to be able to quantify the hydrological fluxes within the Maisbich headwater using temperature as a tracer, we had to calculate the temperature of the stream water independently. Therefore, we coupled an energy balance model with a routing and advection-dispersion model. Through this coupling we could treat temperature as a high resolution conservative tracer. The difference between observed and simulated temperature should then be caused by different exchange fluxes, which subsequently can be quantified. For an adequate temperature model many processes need to be included and described. Therefore a large part of this thesis consists of the quest for a perfect temperature model. During this quest a couple of new insights were gained.

First of all, heat exchange with in-stream rock clasts appeared to be important. The many abundant rock clasts present on top of the streambed store heat, resulting in retarded heat transport. We showed that during winter flow the heat was retarded for more than 30 min after being transported over 565 m. By using a pin-meter we were able to observe the amount of rock clasts present in the cross-sectional area of the stream. Due to the fast heat exchange between water and rock clasts, we could simplify the model by assuming that the temperature of in-stream rock clasts is always the same as the water temperature.

During the quest for the perfect model, we also developed a new method to quantify surface water-groundwater interactions (or hyporheic exchange). Stream water infiltrates into the subsurface (hyporheic zone) where it remains for a while before it returns to the stream. This process influences in-stream temperature, making it possible to quantify this flux. Because of the high resolution temperature observations, we were able to show the large spatial variability in hyporheic exchange. Compared to many other in-stream tracer studies that use conventional stream tracers, we could quantify hyporheic exchange at a high resolution with more flexibility in experimental design.

After the inclusion of heat exchange with in-stream rock clasts and hyporheic exchange, observed daily temperature fluctuations could be adequately simulated during steady state discharge conditions. In the last step we extended the model to unravel spatial and temporal dynamics in discharge during a short but intensive summer rainstorm. Using the model as a learning tool, we showed that for such an event, gains of water remained constant over the event, stream losses increased with increasing discharge, and hyporheic exchange appeared to increase with discharge for part of the stream. From the modelling results, we also concluded that a side channel becomes active several hours after the start of the rainfall event.

Although we were able to quantify discharge dynamics at high temporal and spatial resolution, which was the main objective and trigger for this research, we were only able to do this for low flow conditions during summer. During higher flows, larger rainstorms or less favourable meteorological conditions, observed temperature differences appeared to be too small to distinguish between different fluxes.

A higher accuracy in temperature observation would decrease this problem. At this moment, DTS systems with a spatial resolution of 25 cm are already available while advanced calibration techniques improve the accuracy significantly. These developments make it possible to quantify sources even when there are small temperature differences in the stream. Another way forward is to artificially heat up or cool down the stream water although this would require large amounts of energy which may have their practical limitations as well.

This study has shown that high resolution temperature observations can be instrumental in understanding detailed processes in hydrological systems. With the advance of this and other high resolution tracer techniques more new breakthroughs in understanding hillslope processes

may be expected in the near future.

Samenvatting

De bovenlopen van rivieren leveren een belangrijk aandeel in de totale rivierafvoer. De gebieden zijn klein, maar samen beïnvloeden ze de afvoer aanzienlijk. Om goede afvoervoorspellingen te maken onder een veranderend klimaat of landgebruik, is het belangrijk om de verschillende afvoerprocessen in de brongebieden tot in detail te begrijpen.

In dit proefschrift verkennen we de mogelijkheden van *fibre optic Distributed Temperature Sensing* (DTS) om meer inzicht te krijgen in temporele en ruimtelijke afvoer dynamiek tijdens piekafvoeren. DTS is een techniek waarmee temperatuur met een hoge temporele en ruimtelijke resolutie gemeten kan worden. De techniek is ontwikkeld in de tachtiger jaren van de vorige eeuw voor de olie-industrie, maar slechts sinds kort (2006) is het in het vakgebied van de hydrologie geïntroduceerd. Het principe van DTS bestaat uit korte laserpulsen die door een glasvezelkabel gezonden worden. Overal in de kabel wordt een minieme hoeveelheid licht weerkaatst door kleine oneffenheden in de glasvezel. De exacte positie waar een lichtdeeltje weerkaatst kan berekend worden door de reistijd van het gereflecteerde licht te meten. Als gevolg van de weerkaatsing treden er kleine veranderingen op in de golflengte van het gereflecteerde licht en deze veranderingen kunnen gebruikt worden om de temperatuur te bepalen op de plek van de weerkaatsing.

Alle metingen die in deze thesis zijn beschreven zijn gedaan in de Maisbich: een klein eerste orde beekje in het hart van Luxemburg. De bodem bestaat uit leisteen, bedekt met een enkele meters dikke laag los gesteente vermengd met wat klei waar nog een dunne laag fijn sediment bovenop ligt. De typische zomerafvoer in de Maisbich kan minder zijn dan 1 l s^{-1}, terwijl de jaarlijkse maximum afvoer rond de 50 á 100 l s^{-1} ligt. In de beek bevinden zich zes geconcentreerde bronnen die bijdragen aan de afvoer, en twee locaties waar een significant gedeelte van het water weer in de bodem infiltreert.

Om de verschillende hydrologische fluxen in de Maisbich te kunnen kwantificeren met behulp van temperatuur als tracer, moesten we de temperatuur van het water berekenen. Hiervoor hebben we een energiebalans model gekoppeld aan een advectie-dispersie model. Door deze koppeling is temperatuur een conservatieve tracer geworden: de verschillen tussen gemeten en berekende temperatuur worden dan veroorzaakt door verschillende water fluxen, die vervolgens dus gekwantificeerd kunnen worden. Maar voor een adequaat temperatuur model moeten vele processen meegenomen worden die dan ook nog gekwantificeerd moeten worden. Daarom bestaat

dit proefschrift voor een groot deel uit het optuigen van een zo perfect mogelijk temperatuur model. Tijdens dit proces dienden zich een aantal nieuwe inzichten aan.

Allereerst hebben we aangetoond dat warmte-uitwisseling met de in de beek aanwezige stenen belangrijk was. Deze stenen lagen bovenop de bodem van de beek en doordat ze ook warmte opslaan, was het warmtetransport in de beek, vergeleken met dat van water, vertraagd. We laten zien dat gedurende winterafvoeren, een puls van koud water meer dan 30 min langer over 565 m doet dan het water zelf. Met behulp van een zelf gefabriceerd 2D pinbord konden we voor ieder waterstand de hoeveelheid stenen bovenop de bodem bepalen en door de snelle uitwisseling van warmte tussen water en stenen konden we het model vereenvoudigen door aan te nemen dat de temperatuur van de stenen altijd hetzelfde is als dat van het omringende water.

Tijdens de zoektocht naar het perfecte temperatuur model hebben we ook een nieuwe methode ontwikkeld om oppervlaktewater-grondwater interactie te kwantificeren. Oppervlaktewater infiltreert in de bodem, wat het na een bepaalde tijd weer verlaat om terug te stromen naar de beek. Dit teruggekeerde water beïnvloedt de temperatuur van het oppervlaktewater, wat het mogelijk maakt om deze flux te kwantificeren. Omdat we hoge resolutie temperatuur metingen hadden, konden we ook de grote ruimtelijk spreiding in deze uitwisseling aantonen. Vergeleken met veel andere studies waar conventionele tracers gebruikt worden, konden we de oppervlaktewater-grondwater interactie met een hogere ruimtelijke resolutie kwantificeren, terwijl de experimentele opzet flexibeler is.

Nadat we de warmte-uitwisseling met stenen en de oppervlaktewater-grondwater interacties geïntegreerd hadden in het model, konden we de gemeten dagelijkse temperatuur fluctuaties met hoge nauwkeurigheid reproduceren gedurende constante afvoer condities. Als laatste hebben het model uitgebreid om temporele en ruimtelijke variaties in afvoer te kunnen bepalen tijdens een kleine maar intensieve zomerse regenbui. Door stapsgewijs het model aan te passen, toonden we aan dat voor deze bui de bronnen een constante hoeveelheid water gaven, de infiltratie verliezen groter werden naarmate de afvoer hoger werd en dat voor ongeveer de helft van de beek de oppervlaktewater-grondwater interactie groter lijkt te worden met hogere afvoeren. Uit de modelleer resultaten konden we ook concluderen dat een kleine nevengeul actief werd enkele uren na de regenbui.

Ofschoon we de fluctuaties in afvoer met hoge resolutie konden kwantificeren - wat het hoofddoel en aanzet was voor dit proefschrift - lukte dit alleen tijdens lage zomerse afvoeren. Tijdens hogere afvoeren, grotere regenbuien of minder warme dagen, bleken de fluctuaties in water temperatuur te klein om verschillende water fluxen te kunnen onderscheiden.

Hogere nauwkeurigheid in de temperatuur metingen zouden dit probleem kleiner maken. Op dit moment zijn er al DTS systemen beschikbaar met een ruimtelijke resolutie van 25 cm terwijl nieuwe geavanceerdere kalibreer technieken de nauwkeurigheid significant groter kunnen maken. Deze nieuwe ontwikkelingen zorgen ervoor dat zelfs bij kleine temperatuur verschillen, bronnen

al gekwantificeerd kunnen worden. Een ander manier om meer inzicht te krijgen tijdens hogere afvoeren is om kunstmatig het water op te warmen of af te koelen. Daarvoor is echter veel energie nodig, waardoor deze optie ook zijn praktische limitaties heeft.

Al met al heeft deze studie aangetoond dat hoge resolutie temperatuur observaties instrumenteel kunnen zijn in het tot in detail begrijpen van hydrologische systemen. Met de opmars van deze, en andere hoge resolutie tracer technieken, is het slechts een kwestie van tijd dat er nieuwe inzichten komen waardoor we hydrologische processen nóg beter begrijpen.

List of Symbols

A	Cross sectional area of the stream (m^2)
A_o	Surface area of the stream as seen from the above (m^2)
B_c	Brunt coefficient (-)
B_r	Bowen ratio (-)
C	Salt concentration (kg m^{-3})
C_f	Hydraulic friction of streambed (-)
C_L	Ratio between observed and clear sky solar radiation (-)
C_{shadow}	Shadow fraction (-)
D	Longitudinal dispersion coefficient (m^2 s^{-1})
D_{diff}	Fraction of solar radiation that is diffuse (-)
D_f	Fraction of solar radiation which reaches the stream bed (-)
E	Open water evaporation (m s^{-1})
H	Relative humidity (-)
K_{soil}	Thermal conductivity (W m^{-1} $°C^{-1}$)
L	Distance between tracer input and observation point (m)
N_{DaI}	Damkohler number (-)
P	Wetted perimeter of stream (m)
P_a	Adiabatic atmospheric pressure (kPa)
Q	Discharge (m^3 s^{-1})
R	Hydraulic radius (m)
T	Temperature (°C)
U_{wind}	Wind speed (m s⁻1)
V	Volume of stream (m^3)
W	Width of stream (m)
a_1	Empirical constant (0.094 $kPa^{-1/2}$)
c	Heat capacity (J kg^{-1} $°C^{-1}$)
d_{hz}	Thickness of hyporheic zone (m)
e_a	Actual vapour pressure (kPa)
e_s	Saturation vapour pressure (kPa)
g	Gravity (m s^{-2})
q	Discharge per unit stream length (m^3 m^{-1} s^{-1})
q_{hyp}	Hyporheic flux per unit stream length (m^3 m^{-1} s^{-1})
r	relative error (%)
r_a	Aerodynamic resistance (s m^{-1})
r_c	Ratio between total and conducting cross-sectional area (-)
s	Slope of saturated vapour pressure (kPa $°C^{-1}$)
t	Time (s)
u	Stream velocity (m s^{-1})

x	Distance (x)
z	Depth (m)
Φ_{atm}	Net energy exchange between water and atmosphere (W m^{-2})
Φ_{bed}	Net radiation reaching the streambed (W m^{-2})
Φ_{cond}	Riverbed conduction (W m^{-2})
$\Phi_{diffuse}$	Diffuse solar radiation (W m^{-2})
Φ_{direct}	Direct solar radiation (W m^{-2})
Φ_{latent}	Latent heat flux (W m^{-2})
Φ_{LW}	Net long wave radiation (W m^{-2})
Φ_{LWa}	Atmospheric longwave radiation (W m^{-2})
Φ_{LWb}	Back radiation from the water surface (W m^{-2})
Φ_{LWc}	Land cover longwave radiation (W m^{-2})
Φ_{obs}	Observed solar radiation (W m^{-2})
Φ_{sens}	Sensible heat flux (W m^{-2})
Φ_{solar}	Net incoming solar radiation (W m^{-2})
α	Exchange coefficient between stream and transient storage (s^{-1})
β	Albedo (-)
ϵ_{atm}	Emissivity of the atmosphere (-)
ϵ_{veg}	Emissivity of the vegetation (-)
γ	Psychometric constant (kPa $°C^{-1}$)
η	Fraction of rock clasts in the stream (-)
λ	Latent heat of vaporization (J kg^{-1})
θ_{vts}	View to sky coefficient (-)
ρ	Density (kg m^{-3})
σ_{SB}	Stefan Boltzman constant (W m^{-2} $°C^{-4}$)
ζ	Altitude above mean sea level (m)

List of Subscripts

BF	Base flow
L	Lateral
R	Rain
S	Transient storage
air	Air
b	Bulk of water and in-stream rock clasts
d	Downstream of lateral inflow
$down$	Downstream V-notch weir
hz	Hyporheic zone

new	New external water
r	In-stream rock clasts
soil	Soil
tot	Total
u	Upstream of lateral inflow
up	Upstream V-notch weir
w	Water

Contents

Chapter 1

Introduction

1.1 Background

1.1.1 The importance of headwater catchments for discharge generation

Headwater catchments are small but important contributors to streamflow. Headwaters are the origin of streams and rivers and function as a first filter between natural and unnatural inputs from the landscape into forms that downstream ecosystems are adapted to utilize [Bishop et al., 2008]. It dampens floodwaves and buffers polutants and nutrients. Biodiversity in headwaters is large, since they offer refuge and a water network suitable for migration. The headwaters are the veins in the landscape. They are small, but all combined they are one of the most important contributors to river flow. For example, more than 90% of the stream length in Sweden has catchment areas under 15 km^2 [Bishop et al., 2008].

A very common behaviour in discharge generation processes, that has been observed in many headwaters, are threshold processes [Zehe and Sivapalan, 2009]. This means that, before a catchment responds to rainfall, first a certain threshold has to be exceeded. Beside the quantification of the threshold itself, also the mechanism responsible for this threshold was and is the focus of many discharge generation studies.

An important threshold in (semi-)arid or urban areas is the infiltration capacity: if the rainfall intensity is higher than the infiltration capacity, so-called 'Horton overland flow' occurs [e.g. Kirkby and Chorley, 1967], which means that excess water that cannot infiltrate flows directly over the surface, leading to very fast runoff responses. On the other hand, in temperate climates or forested catchments – where this study has been done – the infiltration capacity is often much higher and other thresholds come into play. In such areas, overland flow only occurs when the groundwater level reaches the surface [Dunne and Black, 1970].

In most of these headwaters, 'subsurface stormflow' is the main process responsible for the fast and high runoff response. Subsurface stormflow also occurs after a certain threshold has exceeded, but it happens out of sight, making it difficult to identify the mechanism responsible for the threshold behaviour. In the European temperate climate, this mechanism is dominant,

Animation 2: Observed (black line) and simulated (grey line) temperature with hyporheic exchange (see Chapter 5).

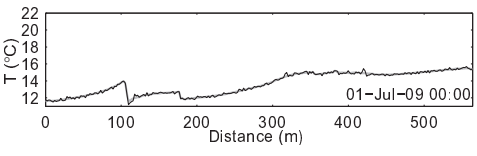

but the different mechanisms can occur in combination, depending on the landscape features and saturation levels [Savenije, 2010].

Nevertheless, because of its importance to stormflow, many researchers try to find specific mechanisms causing threshold behaviour and many different mechanisms have been proposed in literature such as:

- Groundwater ridging [Ragan, 1968] or capillary fringe effect [Gillham, 1984]. This mechanism explains the threshold by the fact that in areas with a shallow groundwater table (often located close to the stream), the unsaturated soil is very close to saturation resulting in a rapid increase in groundwater level after only a small amount rainfall.
- Pipeflow or macropore flow [e.g. McDonnell, 1990]. In this mechanism, the discharge generating process switches from matrix flow during low moisture states, to macropore flow during wet conditions, which is more efficient in discharging water.
- Transmissivity feedback [e.g. Bishop, 1991], which may happen in soils where hydraulic conductivity increases towards the surface. When the groundwater level rises during a rainstorm, the saturated zone reaches better conductive layers, leading to a faster response.
- The fill and spill hypothesis [Tromp-van Meerveld and McDonnell, 2006b], during which uphill hollows in the bedrock should be filled first, before it spills water into a downstream direction. When all (micro)hollows are connected to the stream the discharge generation is highest.

All these mechanisms explain the observed threshold behaviour at different sites and scales. However, processes occurring on small scales cannot be simply summed up to describe processes on larger scales (e.g. overland flow that occurs in an uphill area, can infiltrate before it reaches the stream). On the other hand, observations of lumped processes cannot be broken down to describe small scale processes. What is needed to overcome these scale issues, are continuous descriptions of small scale processes on the km scale [Beven, 2006; Zehe and Sivapalan, 2009; Savenije, 2010].

Measurements are needed to understand the discharge generating processes. The first things to measure are discharge and precipitation, which are relatively easy to measure. But before the rain turns into runoff most water flows through the subsurface which functions as a filter and dampens the runoff peaks. Therefore it necessary to know what happens in the subsurface. However, measurements done in the subsurface are often point measurements from boreholes. Due to the heterogeneity of the soil, these point measurements do not give a lot of information about nearby points. To be able to still get an idea what is going on in the subsurface, indirect measurements should be done.

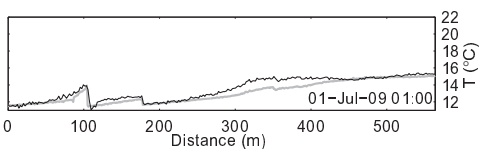

Animation 1: Observed (black line) and simulated (grey line) temperature without hyporheic exchange (see Chapter 5).

1.1.2 The use of tracers in catchment hydrology

One way to indirectly measure subsurface processes is the use of (natural) tracers. Tracers are solute concentrations or other state variables of the water that differ in time or space. Natural tracers refer to tracers that are already present in the water. The most common used natural tracers in hydrology are isotopes (e.g. deuterium, tritium or oxygen-18), dissolved silica and anions or cations (such as Cl^-, Na^+, K^+, Ca^+ and Mg^+), while a less common used tracer is temperature, which we use in this thesis.

In the first place, tracers are water quality parameters, but they can be linked to water quantity by means of an 'end-member mixing analysis' [Sklash and Farvolden, 1979]. With this widely used method a hydrograph is, based on their tracer concentrations, separated into parts originating from different sources, where 'end-member' refers to the representative concentration of a source. The hydrograph is separated by solving, for each time step, a set of mass balance equations:

$$\begin{aligned} Q_{stream} &= Q_{S1} + Q_{S2} + \ldots + Q_{Sn} \\ Q_{stream}C1_{stream} &= Q_{S1}C1_{S1} + Q_{S2}C1_{S2} + \ldots + Q_{Sn}C1_{Sn} \\ Q_{stream}Cn_{stream} &= Q_{S1}Cn_{S1} + Q_{S2}Cn_{S2} + \ldots + Q_{Sn}Cn_{Sn} \end{aligned}$$

where Q is discharge, C_n is tracer concentration of tracer n and the subscripts $_{stream}$, $_{S1}$, $_{S2}$ and $_{Sn}$ stands for stream, source 1, source 2 and source n. For each additional source an extra tracer and an extra equation is needed. When Q_{stream} and all source concentration are known this set of equations can be solved.

The different fractions to which a hydrograph is separated can be in space (or source based), such as groundwater, rapid subsurface flow or rainfall, or it can be separated into event ('new') and pre-event ('old') water, which is a time based separation. The latter is performed using isotope concentrations, while source based separations can be done with chemical tracers or a combination of chemical tracers and isotopes. Uhlenbrook and Hoeg [2003] made an even more pronounced distinction, using chemical tracers for a source based separation, after which isotopes were used to separate the different sources into event and pre-event water.

Many hydrograph separation studies showed that during a rainfall event the majority of the stream water consists of groundwater or pre-event water that is mobilized by the current rain water, while only a small portion consist of the fresh fallen rain water. This is also known as the 'old-water paradox' [Kirchner, 2003; McDonnell, 2003] which is subject to many studies in combination with threshold processes.

Hydrograph separation is a useful technique but there are some features a good tracer should have, making not all tracers suitable. First of all a tracer should be conservative (i.e. the concentration of each source of water should be constant over time and it should not react with its surroundings). Secondly, the concentrations of the different water sources should be sufficient different from each other, and third, they should be easy to measure and preferably not too

Animation 2: Observed (black line) and simulated (grey line) temperature with hyporheic exchange (see Chapter 5).

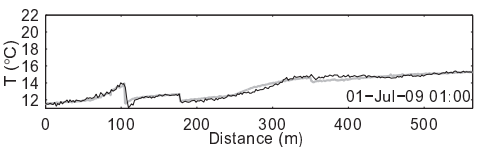

expensive. Due to practical issues, such as measurement errors, non-conservative behaviour of the tracer or the lack of enough suitable tracers, errors in hydrograph separation can become high [Genereux, 1998; Rice and Hornberger, 1998; Uhlenbrook and Hoeg, 2003]. Therefore a hydrograph can only be accurately separated in two or three components, which means that different sources have to be lumped.

So far, hydrograph separation studies were not able to solve the scale issues mentioned in Section (1.1.1). This is mainly caused by a too low spatial resolution of the measurements. In this thesis we aim to solve this problem by using temperature as a tracer, measured at high spatial and temporal resolution.

1.1.3 Temperature as a tracer

Temperature can also be used as a tracer, since it appears to contain information on soil moisture states [Steele-Dunne et al., 2010] and for a wide variety of hydrological processes (e.g. evaporation, groundwater flow, infiltration and stream flow). The big advantage of temperature is that, compared to many other tracer, it is relatively easy to measure, but it has the disadvantage that it is not conservative, since heat can be easily exchanged with its surroundings.

However, in the subsurface, the heat exchanges are relatively easy to determine, making temperature a suitable tracer in (shallow) groundwater systems. Therefore it is often used to quantify upwelling or downwelling fluxes in riverbeds or to identify flow patterns in aquifers [see Constantz, 2008, for an extensive review of heat as a groundwater tracer]. As a stream tracer, temperature has also been applied [e.g. Kobayashi, 1985; Shanley and Peters, 1988; Kobayashi et al., 1999]. But their results should be interpreted in a qualitative way only, since they did not determine the energy balance, which takes heating or cooling of the stream into account. Also transport processes such as advection and dispersion were lacking in their studies. So basically, they treated temperature just as any other tracer.

To really take advantage of the fact that temperature is easy to measure, one should measure it at higher spatial scales than classical tracer studies. In this thesis we do that with fibre optic Distributed Temperature Sensing (DTS). This technique was developed in the 1980's for industrial applications, but only recently Selker et al. [2006b] introduced this technique into the field of hydrology. It consists of a fibre optic cable, through which short pulses of laser light are send. While most of the light leaves the cable at the far end, everywhere in the cable a small fraction of light is reflected. Because the velocity of light is known, it is possible to determine at which distance in the cable a certain photon was reflected. The temperature at the point of reflection is then hidden in the frequency shifts of the reflected light (see Chapter 2 for a detailed description of this technique). Depending on the measurement device, the spatial resolution can be 1 m and the temporal resolution can be as short as 10 s. This offers the opportunity to measure high resolution temperature profiles along a stream.

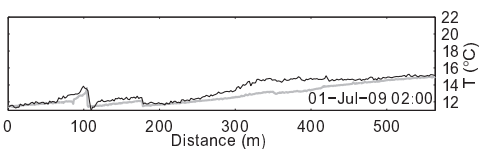

Animation 1: Observed (black line) and simulated (grey line) temperature without hyporheic exchange (see Chapter 5).

But, as said before, the disadvantage of temperature as a tracer is that it is not conservative. However, when all energy fluxes are determined, temperature becomes a conservative tracer. Such an energy balance model should then be coupled with a transport model and eventually with a river routing model to account for all flow processes as well. If all energy fluxes are adequately determined, the difference between observed temperature and simulated temperature is then due to different water fluxes, such as incoming (ground)water or surface water-groundwater interactions, which can then be determined. Also losses of stream water can be determined, since it influences temperature as well, but only indirect (i.e. a small amount of water heats up or cools down faster than a large amount of water).

For a good temperature model many parameters are needed, which are often spatially distributed. This makes it difficult to get a good model. Therefore a large part of this thesis, is the quest for a perfect temperature model. Although a perfect model is impossible, the quest for it resulted in some trade offs. First of all we found that heat exchange with in-stream rock clasts is an important heat flux influencing transport of heat, and secondly, we showed the advantage of using DTS to quantify groundwater surface water interactions. With the final temperature model we were able to quantify spatial and temporal dynamics in discharge during a summer rainstorm.

1.2 Objectives

This thesis fits in the long term objective to better understand discharge generation processes in headwater catchments. Among other studies, tracer studies already gained decent understanding of the different discharge generating mechanisms. However, the different fluxes that have been distinguished were lumped, making it difficult to determine at which points along the stream there are lateral inflows.

In this thesis we explore the suitability of using high resolution temperature observations to identify different lateral inflows at higher resolution. The focus lies on developing and combining methods to better interpret the observed temperature signal (in space and time) and to quantify fluxes that influence in-stream temperature.

The following three objectives have been defined for this research:

- To explore opportunities and limitations of DTS in the field of hydrology.
- To model all flow and energy processes (including hyporheic exchange) during steady state flow using combined transport and energy balance models.
- To quantify discharge dynamics during stormflow.

All these objectives have a specific focus on high spatial and temporal resolution.

Animation 2: Observed (black line) and simulated (grey line) temperature with hyporheic exchange (see Chapter 5).

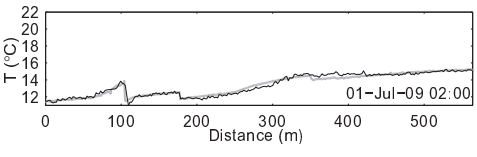

1.3 Outline of thesis

In Chapter (2) the study area has been described. In the same Chapter all measurements have been described and the DTS technique is explained in detail. Two sprinkling tests, performed on a small plot next to the stream, have been described and interpreted to get a general idea of how the catchment functions and to get an idea of the heterogeneity of the subsurface.

The temperature model has been described in Chapter (3). The used transport formulas are shown and all fluxes of the energy balance model are explained. However, in Chapters (4) and (5), the temperature model is improved, by adding more processes to the model.

In Chapter (4) the influence in-stream rock clasts have on water temperature has been explored and quantified. This has been done by releasing cold water, with a salt tracer, from a small basin into the stream. By comparing breakthrough curves of salt and heat the effect of in-stream rock clasts could be quantified. Also a method to quantify stream losses is presented in this Chapter.

In Chapter (5) the focus lies on hyporheic exchange. Here we developed a method to quantify hyporheic exchange at high resolution using DTS, while also being able to estimate the location of the hyporheic zone. The proposed method offers more freedom to experimental setup, compared to studies using other tracers.

With the improvements made in Chapter (4) and (5), in-stream temperature could be adequately simulated during steady state discharge conditions. In the next step (Chapter 6) the same model has been applied to quantify spatial and temporal dynamics of discharge during a summer rainstorm. Here we showed that stream losses are a function of discharge and different hypotheses have been tested about the location of extra, by rain induced, lateral inflow. Also the change in hyporheic exchange fluxes during this summer rainfall has been tested.

In Chapter (7) we performed long term simulations of full months to show the information hidden in longer simulation periods, without going to much into the details. Subsequently we discuss how they can be used for developing hypotheses about the causes of mismatches between observed and simulated temperature.

Finally, all results are brought together and the case studies are synthesized in Chapter (8). Some practical issues concerning the DTS measurement device are discussed as well as the limitations of the method to quantify discharge generation processes. We show that large temperature variations of a few degrees are needed to quantify different fluxes. In the study area, where our measurements have been done, the temperature variations are only sufficient during low flow and warm summer days. However, possible ways forward to overcome this problem have been discussed as well.

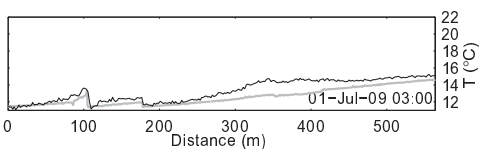

Animation 1: Observed (black line) and simulated (grey line) temperature without hyporheic exchange (see Chapter 5).

Chapter 2

Site description and measurements

2.1 Site description

All field experiments and data collection took place in a branch of the Maisbich, a first order stream located in central Luxembourg; latitude 49°53' N and longitude 6°02' E.

The Maisbich is located in the Oesling region, which covers the Northern third of Luxembourg. The Oesling is underlain by Palaeozoic rocks of Lower Devonian age[1] (Fig. 2.1). The most common rock type in this area is 'schist' or 'Schiefer'. These fine-to-medium near-shore deposits with a low degree of metamorphosis are slates (http://www.geology.lu) although others classify it as shales. The Oesling is a generally NE-SW-trending fold system; the Maisbich is located in the Wiltz syncline structure (Fig. 2.1).

During the Pleistocene, a general uplift of the region occurred, which was then transected by rivers. This resulted in many small plateaus at an altitude of 470-490 m above sea level, from which long, gentle slopes lead to steeply incised valleys with maximum valley side slope of more than 58% [Kwaad and Mücher, 1977]. Generally the slopes in the Oesling region have undergone creep processes and important erosion resulting in colluvial deposits along the slope. At the bottom of the slope it is gradually replaced with alluvial valley deposits.

The soils in the Oesling part of Luxembourg are generally (very) young. Detailed soil evolution studies describe polygenetic soil evolution [Kwaad and Mücher, 1977]. In the higher regions soil development from the Holocene period is available in the Weichselien[2] mass-wasting deposits. Often these soils were truncated or totally eroded after especially late medieval and later human induced forest clearing. Reafforestation started after 1800 reducing the soil erosion process to slow normal rates [Kwaad and Mücher, 1977]. Generally, the Oesling soils classify as dystric cambisols (FAO classification), a soil with weak soil horizons and a low base saturation.

A hydrological interpretation of the schist area was published by Van den Bos et al. [2006]. They stated that significant runoff occurred before the top surface layer was saturated, which they

1. The Lower Devonian is the geological period spanning from 416 to 397 million years ago.
2. The Weichselien is the last glacial period spanning from approximately 116 until 11.5 thousand years ago.

Animation 2: Observed (black line) and simulated (grey line) temperature with hyporheic exchange (see Chapter 5).

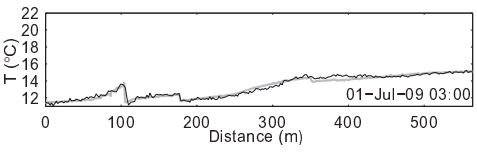

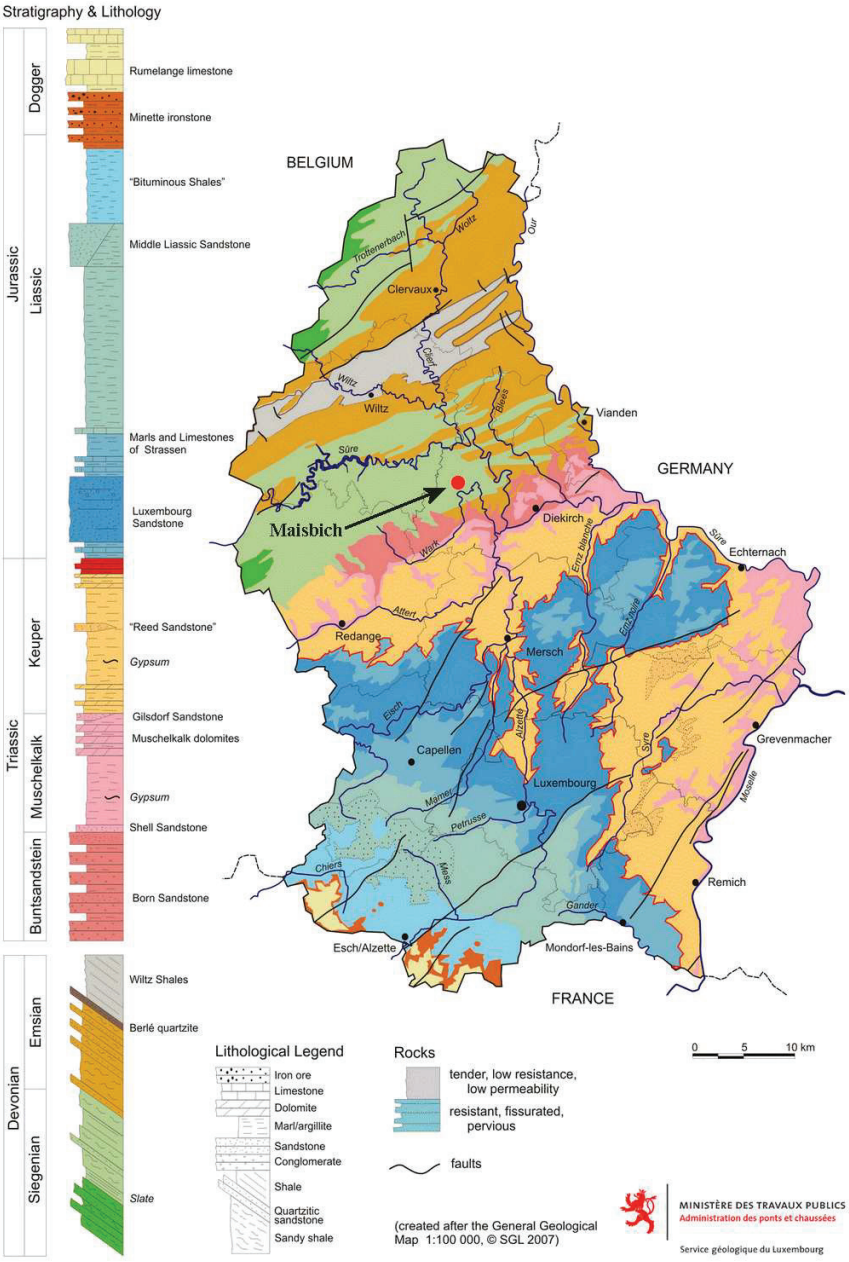

Figure 2.1: Geological Map of Luxembourg. Adapted from http://www.geologie.lu.

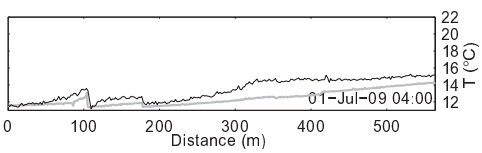

Animation 1: Observed (black line) and simulated (grey line) temperature without hyporheic exchange (see Chapter 5).

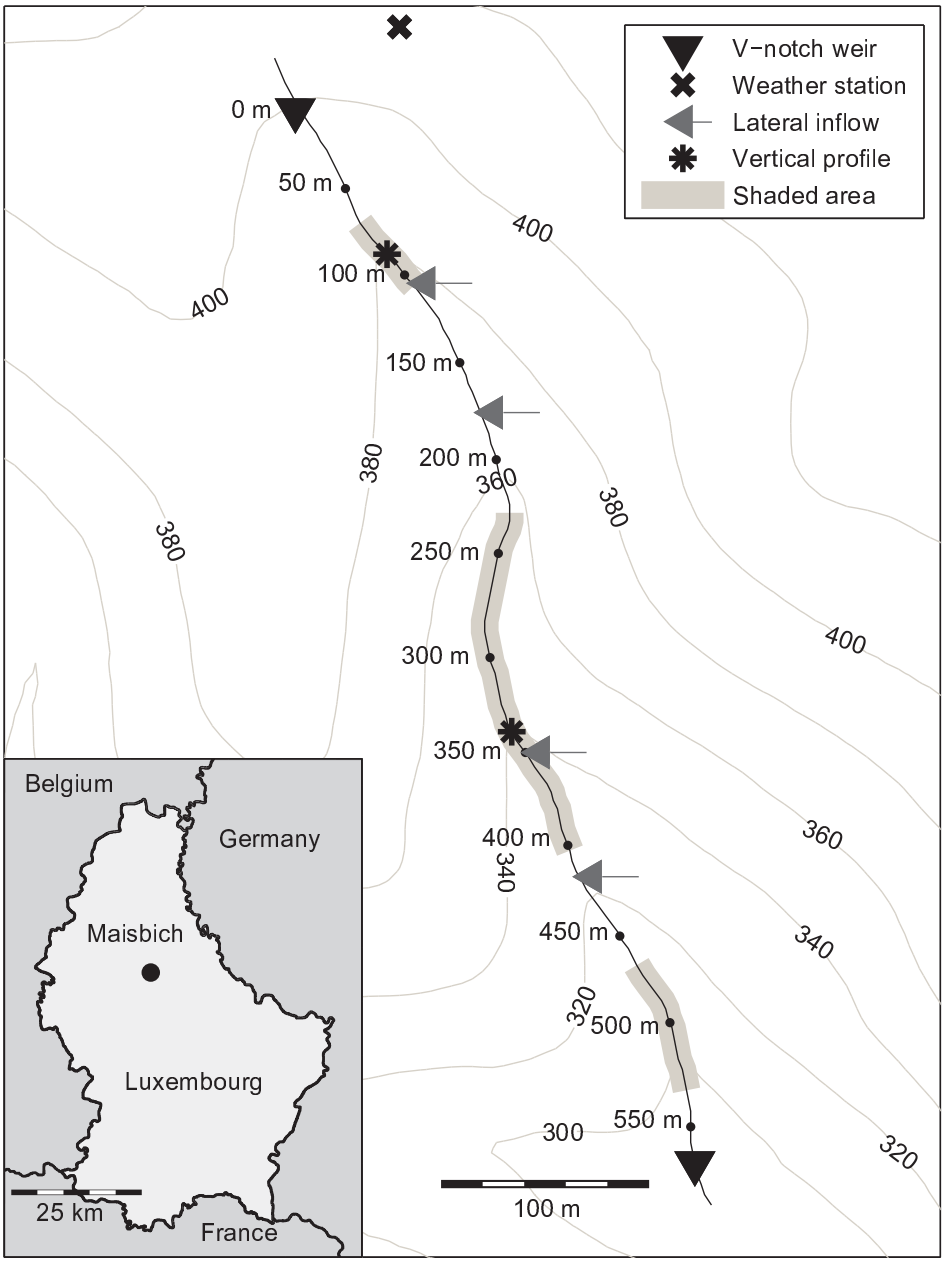

Figure 2.2: Map of the studied branch of the Maisbich. The shaded areas are areas which are never exposed to direct solar radiation. The vertical profile are temperature measurements at four depths below the streambed.

Animation 2: Observed (black line) and simulated (grey line) temperature with hyporheic exchange (see Chapter 5).

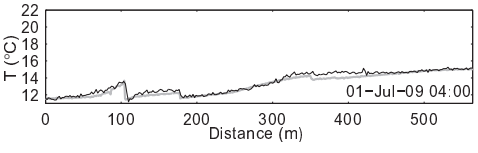

explain by the abundant macropores, created by roots and cracks in the bedrock, that surpass the interception capacity of the soil.

In the Maisbich, the schist bedrock is covered with a layer of loose rock clasts (partly in-situ weathered bedrock) with variable clay content of a few meters thick. This layer is overlain by a thin layer of fine sediments which is 0 to 1 m thick in the direct surroundings of the stream (alluvium) and on the hillslopes (colluviums). The stream scours the soil layer in the valley bottom, creating steep banks of 0.2 to 1 m high at many places. The investigated stream reach is 565 m long, with an average slope of 18% (Fig. 2.2).

During this study, we found four distinct sources of lateral inflow in the stream at 104, 177, 351 and 414 m measured from the upstream V-notch weir, among two small ones at 383 and 393 m which contribute less than 5% of the discharge just downstream of the inflow and are therefore not monitored. All inflows are groundwater sources: the first and last one flow over the land surface for ∼3 and ∼10 m, respectively, while the other sources are within 0.5 m from the stream. Summer baseflow can be less than 1 l s^{-1}, while the observed annual maximum discharge is in the order of 50-100 l s^{-1}, with some extreme values above 100 l s^{-1}. Just upstream of the first lateral inflow (104 m) and between 233 and 247 m a zone exists where a substantial portion of the stream water infiltrates into the bed. During low summer baseflow, as in Chapter (5) and (6), the stream loses 90% of its water between 60 and 77 m and ∼45% of its water between 233 and 247 m. During extremely dry conditions, the stream disappears completely downstream of these zones, while it reappears again at the next lateral inflow. Stream tracer tests (unpublished data) indicate that at least a part of the water that infiltrates between 60 and 77 m returns to the stream at 104 m, since some of the injected salt was found back in the source water.

Most of the banks are covered with vegetation. During summer and only during relatively short periods of time (often around two hours), when the sun's azimuth is close to the stream's aspect, parts of the stream are exposed to solar radiation. Between 66 and 106 m, 225 and 400 m, and 467 and 530 m the canopy prevents most of the solar radiation reaching the stream, even during summer.

2.2 Measurements[3]

2.2.1 Hydrometric measurements

At the upstream and downstream end of the studied reach, two V-notch weirs have been installed and equipped with Keller DCX22 pressure sensors recording water levels with a temporal resolution of 10 min and an accuracy of ∼0.05 l s^{-1} during summer base flow.

3. All observed data are on http://data.3tu.nl, doi:10.4121/uuid:57acdc8d-5c86-478a-9ada-8c075cc30b0a

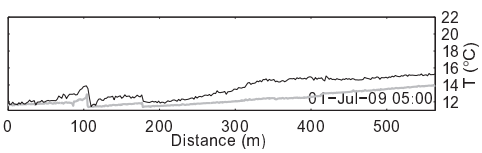

Animation 1: Observed (black line) and simulated (grey line) temperature without hyporheic exchange (see Chapter 5).

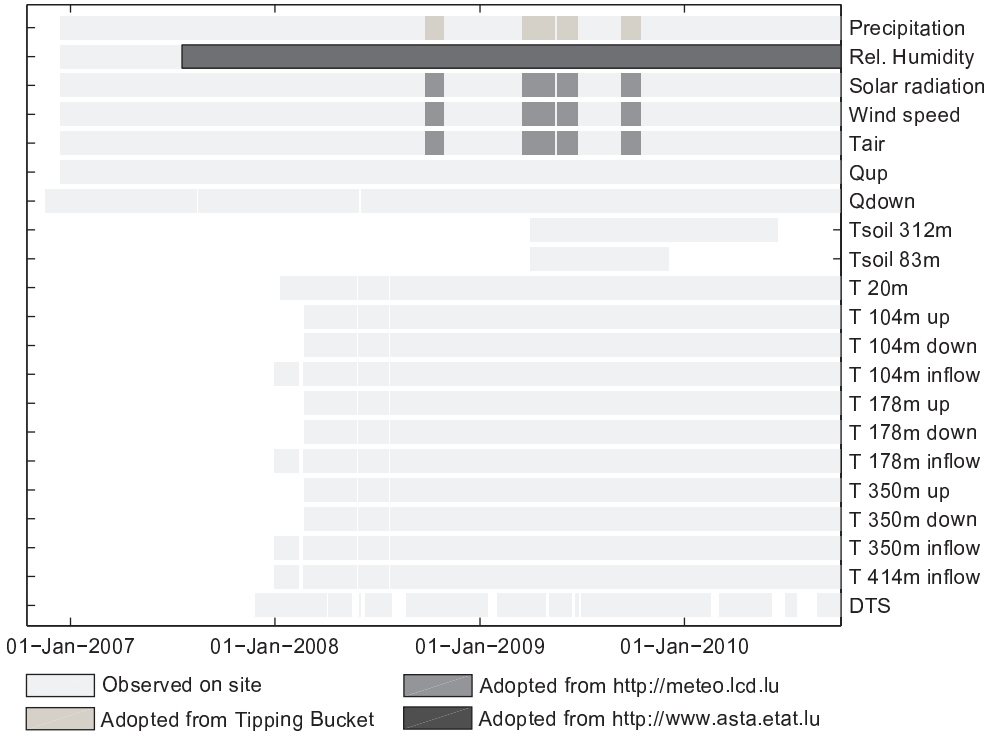

Figure 2.3: Overview of available data. T xxm are TidbiT temperature loggers located at distance xx. up, down and inflow means just upstream, downstream or of the lateral inflow itself. Gaps in meteorological data have been filled with data from nearby stations. The Tipping Bucket was located in the same catchment as the HOBO weather station.

On the plateau, just uphill of the upstream V-notch weir, a HOBO weather station monitors incoming solar radiation, air temperature, wind speed and direction, rainfall and relative humidity at a 10 min interval. Gaps in this data were filled with data from nearby stations: relative humidity data was taken from a nearby weather station in Ettelbruck (∼6 km from the site) from the Administration des Services Techniques de l'Agriculture[4], which had a temporal resolution of 10 min. Rainfall was taken from a tipping bucket located ∼300 Northwest from the weather station. Solar radiation, air temperature and wind speed were taken from meteoLCD in Diekirch[5] (∼ 8 km from the site). For an overview of all data availability see Fig. (2.3). As a first estimate, cross-sectional areas of the stream have been determined, assuming a trapezoidal shape (Chapter 4). In Chapter (5) and (6) the cross-sectional riverbed profiles were measured at 64 places along the stream using a pin-meter (Fig. 2.4). The pins were situated 2 cm from each

4. http://www.asta.etat.lu
5. Meteorological Station of the Lycee Classique Diekirch, L-9233 Diekirch, Luxembourg. Head: Francis Massen, francis.massen@education.lu http://meteo.lcd.lu

Animation 2: Observed (black line) and simulated (grey line) temperature with hyporheic exchange (see Chapter 5).

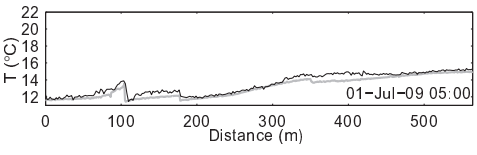

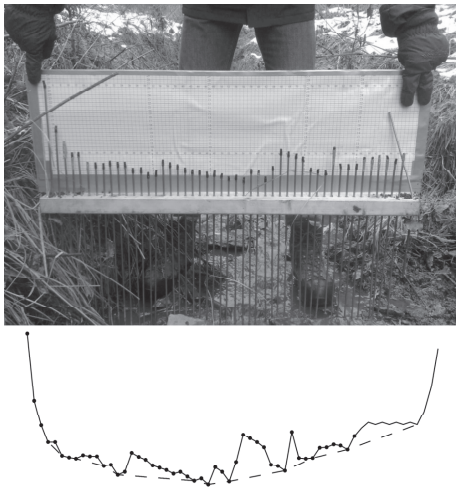

Figure 2.4: Photo of pin-meter (top) and the digitalized bed profile including the contour line (bottom). Note, that to avoid numerical problems, we sometimes added some points on the right or left sides of the observed points to identify the river banks. During the case studies, the water level always stayed within the observed range.

other. The vertical displacement of each pin could be determined with an accuracy of ∼2 mm. To distinguish between in-stream rock clasts and the riverbed (see Chapter 5), we drew a contour around the lower pins. For each water level it is now possible to determine the cross-sectional area of the stream water and the rock clasts, the wetted perimeter and the surface width of the stream.

2.2.2 Temperature measurements†

Along the entire stream, temperature has been measured using a fibre optic Distributed Temperature Sensing (DTS) system. A DTS system consists of a dedicated desktop computer with built-in data-acquisition and processing software, to which a fibre optic cable is attached. Short laser pulses (in the order of a few nanoseconds) are sent through the fibre optic cable. When light strikes matter a small portion of the light may be reflected. By measuring the time between the moment the laser pulse is sent through the cable and the moment a reflected photon comes back, the location of reflectance can be determined, since the speed of light in glass is known. Most of the reflected light is reflected at the original energy, while a portion of that light is adsorbed and reemitted at wavelengths just above and below the frequency of the incident light due to loss or gain from quanta of energy exchanged with electrons. This frequency shifted light

†. Based on: Selker, J. S., Thvenaz, L., Huwald, H., Mallet, A., Luxemburg, W., van de Giesen, N., Stejskal, M., Zeman, J., Westhoff, M., Parlange, M. B., 2006b. Distributed fiber-optic temperature sensing for hydrologic systems. Water Resour. Res. 42 (12), W12202

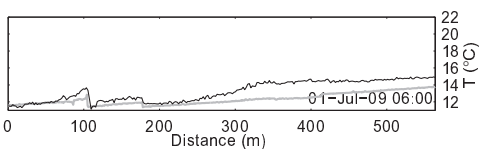

Animation 1: Observed (black line) and simulated (grey line) temperature without hyporheic exchange (see Chapter 5).

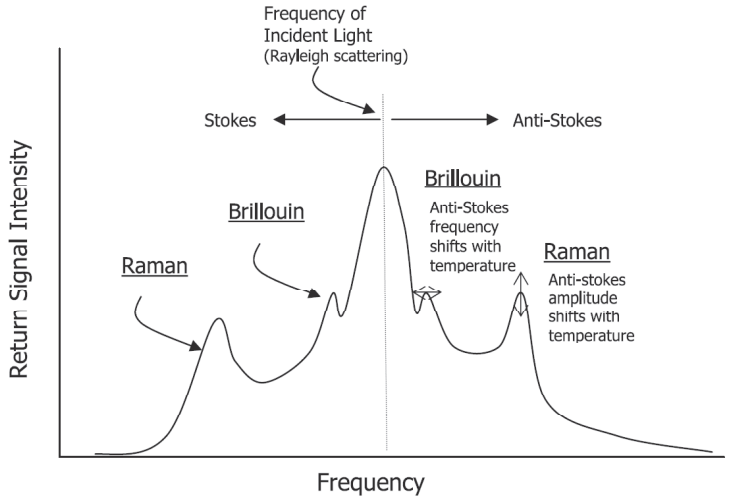

Figure 2.5: Diagram of Raman return scattering intensity below (Stokes) and above (anti-Stokes) the frequency of the injected light.

is referred to as Raman scattering, with the light of frequency below the incident light being referred to as Stokes backscatter, and that above the incident light the anti-Stokes backscatter (Fig. 2.5).

Below a critical light intensity the magnitude of Raman Stokes scattering is a linear function of the intensity of illumination, while at these intensities the anti-Stokes scattering is a function of the intensity of illumination and exponentially of the temperature of the fibre. Hence the ratio of the magnitudes of the anti-Stokes to Stokes scattered light eliminates the intensity dependency and provides a quantity that depends exponentially on the fibre temperature. The precision of this measurement is limited primarily by the accuracy of this ratio, that is a function of the total number of photons observed, which, by the law of large numbers, follows a normal distribution decreasing with the square root of the total number of photons observed. Hence the precision of temperature measurements increases with the square root of the integration interval, as long as instrument drift and other sources of error are insignificant. At the same time, the greater the spatial resolution, the fewer photons are observed per unit time per interval of measurement, resulting in a lower rate of temperature reading convergence.

The strength of the optical signal decays exponentially with distance from the source (Beer's law), so points further from the instrument have lower photon counts, and will therefore also require proportionally longer integration times to obtain a desired level of precision. In summary, the precision of a Raman measurement is, in first approximation, proportional to the square root of the product of the linear distance from the instrument and the number of resolved sections divided by the integration time.

Animation 2: Observed (black line) and simulated (grey line) temperature with hyporheic exchange (see Chapter 5).

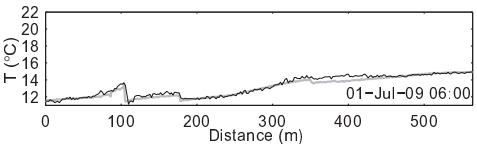

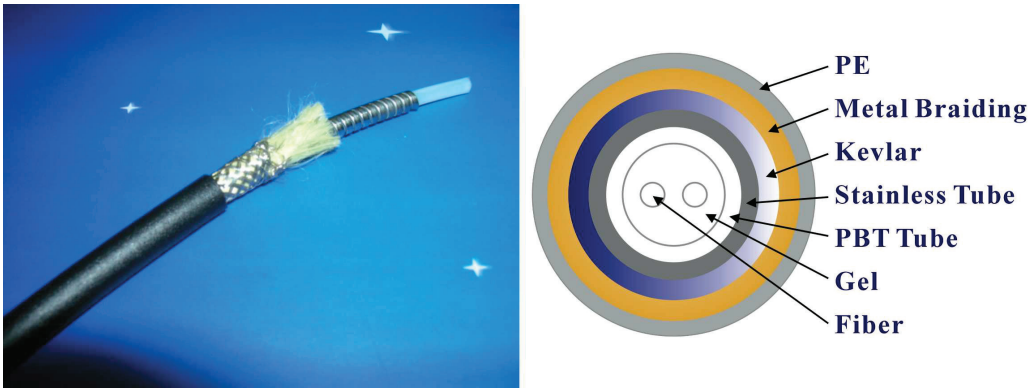

Figure 2.6: Photo and cross-section of Kaiphone fibre optic cable. On the photo, the gel and fibres are not visible. From: Kaiphone Technology Co., Ltd.

One might think that the precision could be improved to an arbitrary degree by using more intense lasers, but this approach is limited by the optical nonlinearity in the scattering that arises at high intensities: it is critical to keep the intensity below this threshold. To obtain the greatest photon count suggests the use of a larger diameter (50 μm diameter, or roughly 2000 μm^2) multimode fibre, which is no longer employed in long-haul communications due to the higher dispersion. On the contrary, a standard 9 μm diameter single-mode cable has almost negligible dispersion, but the allowable signal strength is reduced by a factor of 25 due to the smaller cross section. Because of the greater optical dispersion, the spatial resolution of Raman scattering systems is limited to about 1 m for cable lengths of up to 1000 m, and to about 2 m for lengths up to 10,000 m.

For this research we used a Halo DTS system (Halo, Sensornet, UK), which has a spatial resolution of 2 m and a temporal resolution of 3 min. This configuration resulted in a precision of ∼0.1°C. The DTS obtained temperatures were calibrated with five independent temperature loggers (TidbiT v2 Temp logger, HOBO, USA) located along the cable at 26, 395, 931, 1111 and 1270 m from the DTS desktop computer, respectively. Note that the investigated branch lies between 717 (downstream V-notch weir) and 1282 m (upstream V-notch weir) from the desktop computer. For each Tidbit temperature logger, which measured at a 6 min interval, a linear relation was determined between the DTS derived temperature and the difference between the TidbiT and DTS derived temperature for the period 4-Apr-2008 until 4-Dec-2008 ($\Delta T = aT_{DTS} + b$). For each Tidbit location we now have a slope (a) and an offset (b). We then derived a lineair relation between distance from the DTS desktop computer and slope, and between distance from desktop computer and offset, resulting in an offset as a function of distance and DTS derived temperatures. Subsequently, this offset was added to the initial DTS derived temperatures.

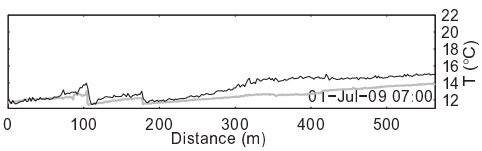

Animation 1: Observed (black line) and simulated (grey line) temperature without hyporheic exchange (see Chapter 5).

The cable used is an armored fibre optic cable (Kaiphone Technology Co., Ltd, Pan Chiao City, Taipei Hsien, Taiwan) with two multimode fibres. The fibres are first covered by very thin plastic, surrounded by gel after which several layers of different materials protect the fibres (Fig. 2.6). Many small stones were put on top of the fibre optic cable, to keep it submerged. However, after storm events, the water replaced many stones and sediments causing the cable to be partly buried or partly above the water, where it measures air temperature. For this reason, employment of a DTS system requires high maintenance in a stream as small as the Maisbich.

In the four major lateral inflow points the temperature was monitored with independent temperature loggers (TidbiT). The temperature upstream and downstream of the three most upstream lateral inflow points was monitored as well with TidbiT temperature loggers. They all had a temporal resolution of 6 min.

At 83 and 312 m from the upstream V-notch weir, temperature loggers (HOBO TMC6-HD sensors connected to an U12-008 logger) monitored the temperature below the stream at depths of 5, 10, 20 and 40 cm at a 30 min interval. These observations were only used for Chapter (5).

2.3 Sprinkling tests

To get an idea of the subsurface structure and its hydrological response, we performed two sprinkling tests at the same plot, which was located just uphill of the lateral inflow point at 350 m (Fig. 2.7). At this location eight piezometers were installed and all were equipped with pressure loggers (Diver, Schlumberger) measuring on a 30 min interval, while a salt tracer was added to the sprinkling water. The two tests were different in design.

Sprinkling test 1

The first experiment was performed between 8-May-2009 and 14-May-2009 and was the subject of the MSc thesis of Rothuizen [2010]. In this section, only a short summary is given. During five days we sprinkled each day 1400 l over an area of ca 150 m^2 during one hour, while on day 6, 1600 l was infiltrated in piezometer P3.3. The sprinkled water had an electrical conductivity of ca 4 mS cm^{-1}. 2D ERT profiles were measured along the steepest gradient, during and right after each sprinkling period. Between 9-May and 12-May a total of 37.8 mm of natural rainfall was observed, of which 20 mm fell on 11-May (day four).

Each day, while sprinkling, the salt tracer was encountered in the lateral inflow, with a delay of 15 to 30 min after the start of the sprinkling test, while the time to peak in the lateral inflow increased from 44 min during the first two days to 81 min at day 4, after which it decreased again to 69 min at day 5. All piezometers showed only minor response to the sprinkled water, except piezometer P1.2, where the water level increased ∼70 cm due to the sprinkling alone.

Animation 2: Observed (black line) and simulated (grey line) temperature with hyporheic exchange (see Chapter 5).

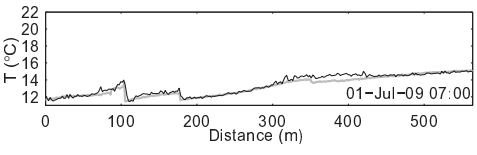

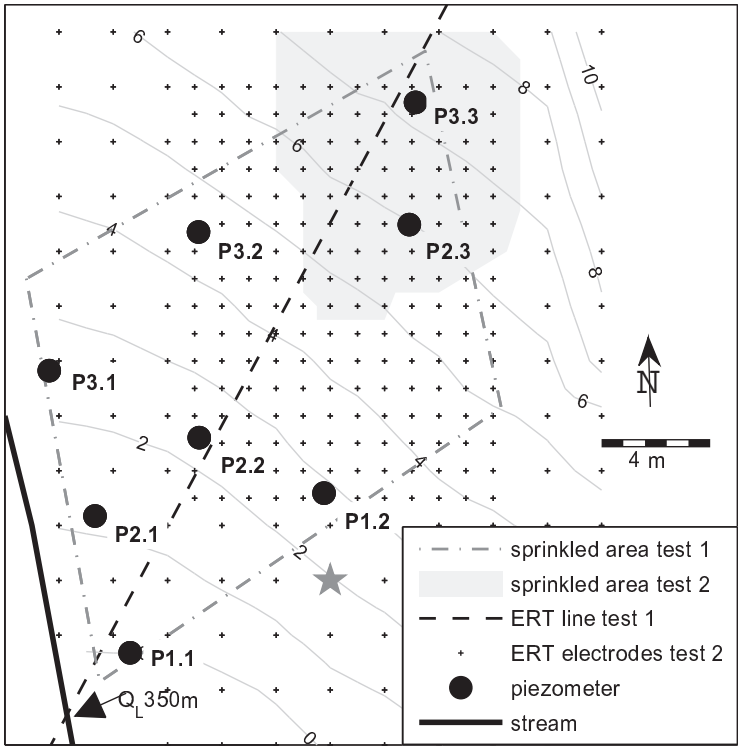

Figure 2.7: Map of sprinkling site, just uphill of the lateral inflow at 350 m. The isohypses are altitudes relative to the surface level of piezometer P1.1. The large star indicates the point where water exfiltrated from the hillslope during an injection test in piezometer P3.3.

This indicates that this piezometer is located in an area collecting water from an uphill area. The 27 mm of natural rain influenced only piezometers P1.2 and P2.3 significantly, where the water level increased with 95 and 80 cm respectively. Especially the increase in P2.3 is assumed to be water fallen on the hillslope uphill of this location. This also indicates that the hillslope was connected to this plot after ca 30 mm of rainfall.

The increase in tracer concentration of the lateral inflow was highest on day 4: an increase of 266 μS cm^{-1} versus $\sim$70 μS cm^{-1} during all other days. This can also be explained by the natural rain, which flushes the unsaturated zone where previous sprinkled salt was stored. Time lapse ERT results show that a decrease in electrical resistivity occurred only in the top 1.5 m of the subsurface. This confirms that most sprinkled water is stored in the unsaturated zone and on top of the saturated zone.

During the injection test in piezometer P3.3 on day 6, first high concentrated water (4.3 mS cm^{-1}) was injected followed by more diluted water $\sim$1 mS cm^{-1}. Reason for this was that injected water was found back at a location Southeast from piezometer P1.2 (large star in Fig.

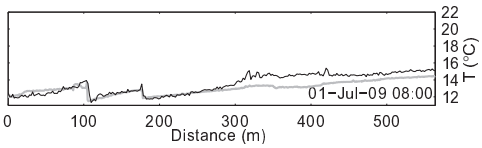

Animation 1: Observed (black line) and simulated (grey line) temperature without hyporheic exchange (see Chapter 5).

2.7), where it exfiltrated out of the hillslope. After injecting the diluted water, the EC of the exfiltrated water went down after ca 40 min, indicating a flow velocity of ∼25 m h^{-1}. During the injection, the water level in piezometer P1.2 increased until 0.30 m below surface level and remained this high until the injection stopped. This indicates that all excess water rapidly flows through the top 30 or 40 cm of the soil where lots of macropores are present.

Sprinkling test 2[†]

During the second sprinkling test, performed between 5 and 8-Oct-2010, we sprinkled 9.3 m^3 on an area of ca 80 m^2 during a period of 22.5 hours, resulting in an intensity of 5.2 mm/h. A salt tracer was added to the sprinkling water, increasing the electrical conductivity to ∼1300 μS cm^{-1}. 3D electrical resistivity tomography (ERT) was performed, using a grid with 291 electrodes. A dipole-dipole configuration running in x and y directions was used to obtain a 3D picture of soil resisivities. Each 1.5 h an acquisition was made containing about 1700 measurements. The inversion of the ERT measurements of the was done using the FE code Bert [Günther et al., 2006; Rücker et al., 2006] and was done in two different ways. On the one hand, the original data were directly inverted and on the other hand, the ratio of the new measurements and the measurements taken before the infiltration was inverted as ratio data. In particular these ratio data were found to have a small root mean square error (RMSE) which implies that the quality of the measurements is good in spite of the partly difficult, stony subsurface with poor electrode contact

During the whole experiment, the largest response was found in piezometers P2.3 and P1.2, with an maximum increase in water level of >146 cm (P2.3 was dry before start of sprinkling) and 124 cm, respectively. piezometers P2.2 and P3.2 only showed a maximum increase in water level of 33 and 12 cm, while P1.1, P2.1 and P3.1 did not show any response. Piezometer P3.3 remained dry during the entire experiment.

The 3D ERT ratios between acquisition at t=t_1 and the pre-event acquisition confirmed the preferential flow towards piezometer P1.2 (Fig. 2.8; a threshold of 0.83 was taken to better visualize the infiltration front, while a value of 1 means no change in electrical resistivity). From this figure it can also be seen that most of the water percolates in a vertical direction, while no lateral flow is visible along the steepest gradient (Northeast - Southwest).

From both experiments, we can conclude that the majority of subsurface flow is through preferential flowpaths, which, in the investigated plot does not follow the steepest gradient of the surface. We can also conclude that the 'observed' preferential flowpath is relative large, resulting in flow velocities in the order of meters per hour.

†. Based on: Noell, U., Wießner, C., Ganz, C., Westhoff, M., 2011. Direct observations of surface watergroundwater interaction using electrical resistivity tomography. IAHS Publ. 345, 42–47

Animation 2: Observed (black line) and simulated (grey line) temperature with hyporheic exchange (see Chapter 5).

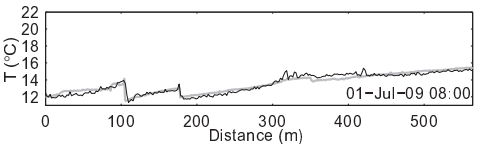

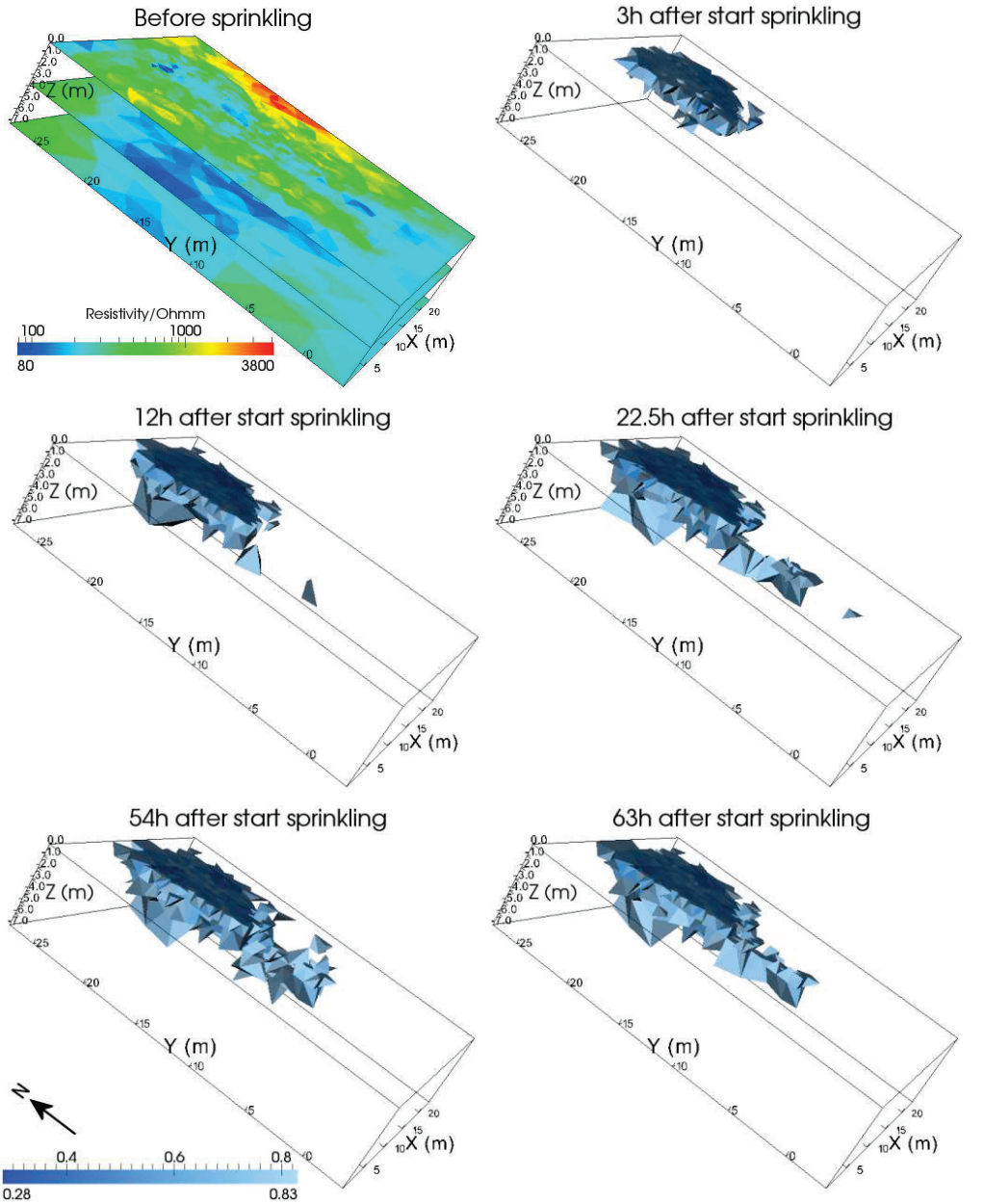

Figure 2.8: Top left: absolute resisivities of the subsoil just before the sprinkling experiment, obtained with 3D ERT. All other figures: time lapse ERT results. The ratio between the acquisition at t=t1 and the pre-event acquisition is shown, where a value of one means no change in resistivity. A threshold of 0.83 was taken to better visualize the wet infiltration front. The sprinkling lasted for 22.5 hours, with an intensity of ∼5.2 mm/h.

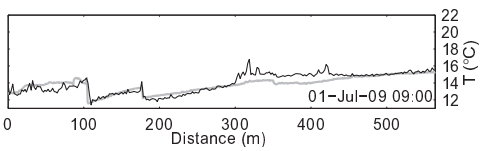

Animation 1: Observed (black line) and simulated (grey line) temperature without hyporheic exchange (see Chapter 5).

Chapter 3

Model setup†

3.1 Routing and transport model

With the DTS fibre optic cable, we measured in-stream temperature with a 2 m and 3 min resolution. To be able to fully analyze the obtained temperature profiles, an energy balance model is needed, describing the energy exchanges between the water-air interface and the water-streambed interface. Since the stream transports heat, the energy balance model should be coupled with a transport model for heat, where the enrgy balance can be treated as a sink/source term. To determine the (dynamic) hydraulic parameters in the transport model, the transport model should also be coupled with an hydraulic model. The coupled models should be able to account for the fast variations in discharge and in-stream temperature in both space and time. We therefore chose a spatial resolution of 1 m, while the used timestep was ≤ 5 s, depending on the how fast the discharge varied. The basic equations for these models are:

The mass balance for water:

$$\frac{\partial A_w}{\partial t} + \frac{\partial Q}{\partial x} = \sum q_L \tag{3.1}$$

the routing model, based on the Saint Venant equation [Stelling and Duinmeijer, 2003]:

$$\frac{\partial u}{\partial t} + g\frac{\partial \zeta}{\partial x} + u\frac{\partial u}{\partial x} + C_f\frac{u|u|}{R} = 0 \tag{3.2}$$

and the transport model:

$$\frac{\partial (A_w T_w)}{\partial t} + \frac{\partial (Q T_w)}{\partial x} + \frac{\partial}{\partial x}\left(-A_w D\frac{\partial T_w}{\partial x}\right) = \sum q_L T_L + \frac{W\Phi_{atm}}{\rho_w c_w} + \frac{P\Phi_{cond}}{\rho_w c_w} \tag{3.3}$$

where A, Q and T are the cross-sectional area (m^2), discharge ($m^3\ s^{-1}$) and temperature ($^\circ C$). q_L is the lateral inflow per unit stream length ($m^2\ s^{-1}$), u is the stream velocity ($m\ s^{-1}$), ζ

†. Based on: Westhoff, M. C., Savenije, H. H. G., Luxemburg, W. M. J., Stelling, G. S., van de Giesen, N. C., Selker, J. S., Pfister, L., Uhlenbrook, S., 2007. A distributed stream temperature model using high resolution temperature observations. Hydrol. Earth Syst. Sci. 11 (4), 1469–1480, `http://www.hydrol-earth-syst-sci.net/11/1469`

Animation 2: Observed (black line) and simulated (grey line) temperature with hyporheic exchange (see Chapter 5).

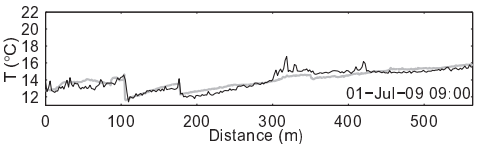

is the water level a.m.s.l. (m) and g is the acceleration of gravity (m s^{-2}). C_f and R are the hydraulic friction of streambed (-) and the hydraulic radius (m). D is the longitudinal dispersion coefficient (m^2 s^{-1}), W is the width of the stream (m) and P is the wetted perimeter (m). Φ_{atm} and Φ_{cond} are the net energy flux (W m^{-2}) between the water-air interface and between the water riverbed interface, respectively, and ρ and c are the density (kg m^{-3}) and heat capacity (J kg^{-1} °C^{-1}), while x and t are distance (m) and time (s). The subscripts $_w$ and $_L$ stand for water and lateral.

The first term of the lefthand side of Eq. (3.3) represents the dynamic energy storage, the second and third term the advective and dispersive transport of energy and the righthand members the sinksource terms, accounting for advective energy exchange of lateral inflows, heat exchange between the water-air interface and energy exchange between the water-riverbed interface.

The numerical solutions for Eq. (3.1 - 3.3) are given in Appendix (A). In Chapter (4) and (5), more processes will be added to Eq. (3.3) to improve the temperature model: In Chapter (4) heat exchange with in-stream rock clasts has been added, and in Chapter (5) hyporheic exchange has been added. All energy balance components are described in Section (3.3).

3.2 Determination of lateral inflows

The second objective is to quantify all flow processes. An important one are the lateral inflows. The four major ones have been equipped with temperature sensors, which makes it possible to determine their relative contribution a priori using a mass balance for temperature:

$$Q_d = Q_u + Q_L \tag{3.4a}$$

$$Q_d T_d = Q_u T_u + Q_L T_L \tag{3.4b}$$

where the subscripts $_d$ and $_u$ refer to the location just downstream and just upstream of the lateral inflow. When all temperatures are known and Q_d is assumed to be 100%, the relative contribution can be determined by solving Eqs. (3.4a and 3.4b):

$$\frac{Q_L}{Q_d} = \frac{T_d - T_u}{T_L - T_u} \tag{3.5}$$

Assuming normally distributed errors in the temperature observations, the absolute error $\sigma_{(Q_L/Q_d)}$ (°C) of the relative contribution of a lateral inflow, is determined as [Genereux, 1998]:

$$\sigma_{(Q_L/Q_d)} = \left\{ \frac{1}{(T_L - T_u)^2} \sigma_{T_d}^2 + \left[\frac{T_d - T_L}{(T_L - T_u)^2} \right]^2 \sigma_{T_u}^2 + \left[\frac{T_u - T_d}{(T_L - T_u)^2} \right]^2 \sigma_{T_L}^2 \right\}^{0.5} \tag{3.6}$$

where σ_T is the standard deviation of the temperature measurements (°C). The relative error (r) in Q_L/Q_d is then obtained by dividing Eq. (3.6) by Eq. (3.5).

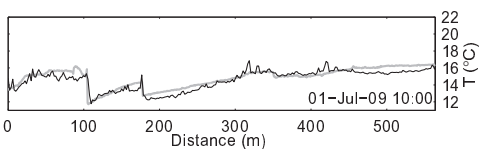

Animation 1: Observed (black line) and simulated (grey line) temperature without hyporheic exchange (see Chapter 5).

3.3 Energy balance model

The energy fluxes in Eq. (3.3) were split up in two components: The first one (Φ_{atm}) describes all energy fluxes through the water-air interface, the second one (Φ_{cond}) describes the energy flux through the water-streambed interface. A positive flux is defined as a flux towards the water, meaning that the water heats up. The energy flux through the water-air interface is given as the sum of net solar radiation, longwave radiation, latent heat and sensible heat:

$$\Phi_{atm} = \Phi_{solar} + \Phi_{LW} + \Phi_{latent} + \Phi_{sens} \tag{3.7}$$

where each component is determined separately.

3.3.1 Solar radiation

Solar radiation consists of direct radiation and diffuse radiation of which a part is reflected by the water surface and a part is absorbed by the water body. The remaining part reaches the streambed, of which also a part is reflected and a part is absorbed by the streambed. Shadowing influences the direct radiation, and thus must be estimated. Critical shadow angles were calculated for each grid cell. Partial shading due to vegetation was also taken into account. The diffuse radiation is assumed not to be influenced by shadow effects (i.e. diffuse radiation in shaded parts is assumed to be the same as in non-shaded parts) . The net solar radiation is computed as:

$$\Phi_{solar} = \beta(1 - D_f)(\Phi_{direct} + \Phi_{diffuse}) \tag{3.8}$$

$$\Phi_{direct} = (1 - D_{diff})C_{shadow}\Phi_{obs} \tag{3.9}$$

$$\Phi_{diffuse} = D_{diff}\Phi_{obs} \tag{3.10}$$

where Φ_{obs} is the observed solar radiation, Φ_{direct} and $\Phi_{diffuse}$ are the direct beam and diffuse solar radiation, D_f is the fraction of solar radiation that reaches the streambed, while β and D_{diff} are the albedo and fraction of diffuse solar radiation. The factor C_{shadow} is the shadow factor and is determined by looking at thresholds for shading. For each moment in time the aspect and solar angle was determined and compared with the topographic and vegetation angles. When the stream is completely in the shadow, $C_{shadow} = 0$, and when there is no shading $C_{shadow} = 1$.

3.3.2 Longwave radiation

Longwave radiation Φ_{LW} includes the atmospheric longwave radiation, back radiation (radiation flux emitted from the water column) and land cover longwave radiation. They are all determined using the Stefan-Boltzman law.

The total incoming longwave radiation is the sum of atmospheric and longwave radiation, where the 'view to sky' coeficient (θ_{vts}) determines their relative weight: if vegetation is denser more

Animation 2: Observed (black line) and simulated (grey line) temperature with hyporheic exchange (see Chapter 5).

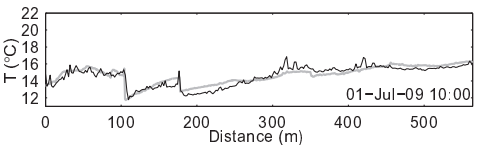

radiation is emitted from the vegetation to the stream, but less radiation is received from the atmosphere. Atmospheric longwave radiation is the longwave radiation the water receives from the atmosphere. It is computed as [Boderie and Dardengo, 2003]:

$$\Phi_{LWa} = 0.96\theta_{vts}\epsilon_{atm}\sigma_{SB}(T_{air} + 273.2)^4 \tag{3.11}$$

$$\epsilon_{atm} = 1.1B_c + a_1\sqrt{e_a} \tag{3.12}$$

$$e_s = 0.61275\exp\left(\frac{17.27T_{air}}{237.3 + T_{air}}\right) \tag{3.13}$$

$$e_a = \frac{H}{100\%}e_s \tag{3.14}$$

where Φ_{LWa} is the atmospheric longwave radiation, θ_{vts} is the 'view to sky' coefficient (-), ϵ_{atm} is the emissivity of the atmosphere (−), σ_{SB} is the Stefan Boltzman constant (W m^{-2} °C^{-4}) and T_{air} is the air temperature (°C). e_a is the actual vapour pressure (kPa), e_s is the saturation vapour pressure (kPa), H is the relative humidity (-), a_1 is an empirical constant (0.094 kPa$^{-1/2}$) and B_c is the 'Brunt' coefficient (-). B_c is an emperical function of air temperature and the ratio of observed solar radiation and clear sky radiation [Koberg, 1964]. It is approximated by:

$$\begin{aligned} B_c = &\left(-2.96e^{-4}C_L^2 + 1.39e^{-4}C_L - 0.12e^{-4}\right)T_{air}^2 \\ &+ \left(5.33e^{-2}C_L^2 - 5.3e^{-2}C_L + 1.43e^{-2}\right)T_{air} + \left(-1.51C_L^2 + 1.69C_L + 0.25\right) \end{aligned} \tag{3.15}$$

where C_L is ratio between Φ_{solar} and the maximum theoretical solar radiation during clear sky conditions (-).

Back radiation (Φ_{LWb}) is the energy flux emitted from the water column. It is computed as [Boderie and Dardengo, 2003]:

$$\Phi_{LWb} = -0.96\sigma_{SB}(T + 273.2)^4 \tag{3.16}$$

Land cover longwave radiation (Φ_{LWc}) is the longwave radiation emitted by the vegetation and received by the water. The land cover longwave radiation is computed as [Boyd and Kasper, 2003]:

$$\Phi_{LWc} = 0.96(1 - \theta_{vts})\epsilon_{veg}\sigma_{SB}(T_{air} + 273.2)^4 \tag{3.17}$$

where ϵ_{veg} is the emmisivity of the vegetation and is set to 0.96. Note that during cloudy conditions, when $\epsilon_{atm} \approx \epsilon_{veg}$, θ_{vts} is insensitive.

3.3.3 Latent heat

Latent heat is the energy used for evaporation. It is computed using the Penman equation for open water [Monteith, 1981]:

$$\Phi_{latent} = -\rho_w\lambda E \tag{3.18}$$

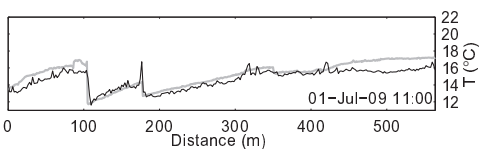

Animation 1: Observed (black line) and simulated (grey line) temperature without hyporheic exchange (see Chapter 5).

$$\lambda = 1000(2501.4 + T_w) \tag{3.19}$$

$$E = \frac{s(\Phi_{solar} + \Phi_{LW})}{\rho_w \lambda (s + \gamma)} + \frac{c_{air}\rho_{air}(e_s - e_a)}{\rho_w \lambda r_a (s + \gamma)} \tag{3.20}$$

$$r_a = \frac{245}{0.54U_{wind} + 0.5} \tag{3.21}$$

$$\begin{aligned} s &= \frac{\partial e_s}{\partial T} \\ &= \frac{e_{s(T=T_{air})} - e_{s(T=T_w)}}{T_{air} - T_w} \end{aligned} \tag{3.22a}$$

for $T_w \approx T_{air}$this becomes:

$$s = e_s\left(\frac{17.27}{237.3T_w} - \frac{17.27T_w}{(237.3 + T_w)}\right) \tag{3.22b}$$

where Φ_{latent} is the latent heat (W m^{-2}), λ and E are the latent heat of vaporization (J kg^{-1}) and open water evaporation (m s^{-1}), s is the derivative of the saturation vapour pressure over temperature (kPa °C^{-1}), γ is the psychometric constant (kPa °C^{-1}), r_a is the aerodynamic resistance (s m^{-1}) and U_{wind} is the wind speed (m s^{-1}) at 2 m high.

3.3.4 Sensible heat flux

The sensible heat flux is the heat exchange between the water and the air, which is driven by temperature differences. It is computed as [Boyd and Kasper, 2003]:

$$\Phi_{sens} = B_r \Phi_{latent} \tag{3.23}$$

$$B_r = 6.1e^{-4} P_a \frac{T_w - T_{air}}{e_{s(T=T_w)} - e_{s(T=T_w)}} \tag{3.24}$$

where Φ_{sens} is the sensible heat flux (W m^{-2}), B_r is the Bowen ratio (-) and P_a is the atmospheric pressure (kPa)

However, when the relative humidity is 100%, the Bowen ratio (B_r) is going to infinity, which is physically not possible. For this reason we used the following equation in Chapter (5) and (6) [Monteith, 1981]:

$$\Phi_{sens} = \frac{\gamma(\Phi_{solar} + \Phi_{LW})}{s + \gamma} + \rho_{air} c_{air} \frac{T_{air} - T_w}{r_a} \tag{3.25}$$

3.3.5 Riverbed conduction

Heat transfer between the water and the riverbed is called streambed conduction. It is driven by temperature gradient between water and subsurface. It is computed as [Boyd and Kasper, 2003], assuming that the river bed is saturated:

$$\Phi_{cond} = -K_{soil} \frac{T_w - T_{soil}}{\mathrm{d}z} \tag{3.26}$$

Animation 2: Observed (black line) and simulated (grey line) temperature with hyporheic exchange (see Chapter 5).

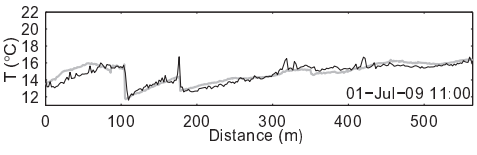

where K_{soil} is the thermal conductivity of the subsurface (W m^{-}1°C^{-}1), T_{soil} is the temperature of the subsurface (°C) and z is the depth (m). The change in temperature of the subsurface is given as

$$\frac{\partial T_{soil}}{\partial t} = -K_{soil}\frac{\partial^2 T_{soil}}{\partial z^2} + \frac{\beta \Phi_{bed}}{c_{soil}\rho_{soil}\mathrm{d}z} \tag{3.27}$$

where Φ_{bed} is the solar radiation reaching the streambed (W m^{-2}) and the subscript $_{soil}$ stands for subsurface. In the schematization of the subsurface, $\Phi_{bed} = 0$ for all layers, except for the top layer.

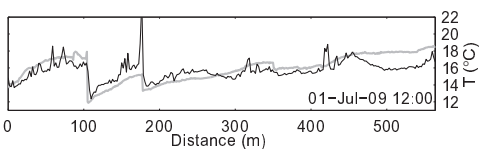

Animation 1: Observed (black line) and simulated (grey line) temperature without hyporheic exchange (see Chapter 5).

Chapter 4

Quantifying the effect of in-stream rock clasts on the retardation of heat along a stream†

Abstract. *The objective of this Chapter is to explore and quantify the retardation of heat along the stream. We carried out two tracer experiments. A small water storage basin was emptied into the stream over time periods of 50 and 18 min increasing stream discharge roughly by a factor of two. Salt was added as a tracer in both experiments. In the second experiment the temperature of the added water was additionally cooled to about 0° C by adding snow into the storage basin. The electrical conductivity was measured at three points along the 565 m long stream, while the temperature was measured with a resolution of 2 m and 3 min using the DTS system. During the second experiment, we observed a significant time lag between the salt breakthrough curves (BTC) and the heat BTCs. We routed the water with a hydraulic model, which we coupled with a 1D advection-dispersion model, and in case of heat we also coupled it with an energy balance. We used the salt BTCs to calibrate the transient storage zones, after which we applied the energy balance to simulate the heat BTCs. Although heat exchange with the streambed delays the advection of heat, it could not fully explain the retarded BTC we observed. We hypothesize that the retardation of heat is caused by its storage in the many rock clasts present in the stream and positioned on top of the streambed. To allow for water-rock clast interaction, we included the fraction of rock clasts in the storage term of the advection-dispersion equation. In this approach we only have to add one additional parameter to account for the fraction of rock clasts in the cross-sectional area of the stream. By applying a fraction of 35% we were able to simulate the retarded heat BTC correctly. Although the fraction of rock clasts in the stream will change with different water levels, it is a straightforward approach, which enables us to couple the hydraulic model directly with the advection-dispersion model, while ensuring that the retardation of heat is simulated correctly.*

†. *Based on: Westhoff, M. C., Bogaard, T. A., Savenije, H. H. G., 2010. Quantifying the effect of in-stream rock clasts on the retardation of heat along a stream. Adv. Water Resour. 33 (11), 1417–1425*

Animation 2: Observed (black line) and simulated (grey line) temperature with hyporheic exchange (see Chapter 5).

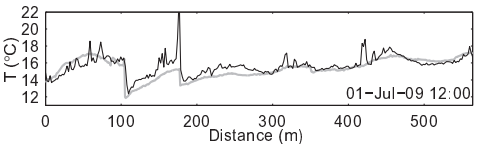

4.1 Introduction

Recently, Distributed Temperature Sensing (DTS) was introduced as a new monitoring device in hydrology [Selker et al., 2006a]. The number of applications of DTS in hydrological studies is now growing rapidly [e.g. Lowry et al., 2007; Moffett et al., 2008; Selker et al., 2006b; Steele-Dunne et al., 2010; Tyler et al., 2009; Westhoff et al., 2007, and numerous contributions at conferences]. However, it is difficult to use the observed temperature signal to quantify hydrological processes due to its non-conservative behaviour, especially when the temperature of the medium is exposed to solar radiation. In such cases, the energy balance needs to be considered, which in our study implied the integration of the energy balance model with the hydraulic model of the stream discharge.

Heat transport models have been developed for numerous different applications, across all hydrological domains. For example, in the saturated and unsaturated soil VS2DI [Healy, 2008] was used to simulate solute and heat transport, while SUTRA [Voss and Provost, 2002] has also been used to simulate density flows in these environments. Transport of heat has also been coupled with distributed hydrological models. Morin et al. [1983] developed CEQUEAU, a 3D hydrological model able to model temperature in the whole model domain. St-Hilaire et al. [2000] adapted this model to more accurately simulate the subsurface temperature yielding a better estimate of the temperature of the groundwater inflows into a stream. Bicknell et al. [1997] developed the software package HSPF to simulate heat and solute transport in surface water and subsurface water. HSPF was extended by Chen et al. [1998a,b] to include a shading module to more accurately simulate the influence of the incoming solar radiation on the surface water. Maxwell et al. [2007] coupled a 3D atmospheric model (ARPS) with the 3D variably saturated groundwater model Parflow. Brookfield et al. [2009] adapted HydroGeoSphere to simulate heat transport in the whole model domain. For a case study in the Pine river in Ontario, Canada they were able to simulate distributed atmospheric input and heat and solute transport over the land surface, and in the subsurface.

In cases where the focus is mainly on the surface water, or when there is (as in our case) no clear connection between the surface water and an extensive groundwater body, in-stream temperature models are sufficient. When longitudinal temperature differences in a stream are negligible, only the energy balance has to be considered [e.g. Bogan et al., 2003, 2004; Brown, 1969; Caissie et al., 2007; Evans et al., 1998; Webb and Zhang, 1997, 1999]. However, in many small streams the advection of heat is not negligible and the advection-dispersion equation must be applied [e.g. Bartholow, 2000; Boyd and Kasper, 2003; Foreman et al., 1997, 2001; Sinokrot and Stefan, 1993; Kim and Chapra, 1997; Westhoff et al., 2007; Younus et al., 2000].

Consequently, to simulate retarded heat transport, transient storage zones have to be taken into account due to surface-subsurface water interactions. In solute transport models [e.g. Bencala and Walters, 1983; Briggs et al., 2009; Choi et al., 2000; Gooseff et al., 2003, 2005, 2007; Runkel, 1998] this is common practice. These models use one or multiple transient storage boxes and

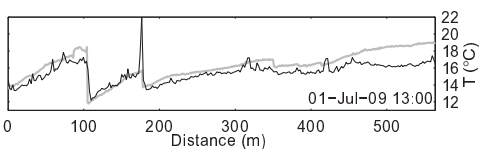

Animation 1: Observed (black line) and simulated (grey line) temperature without hyporheic exchange (see Chapter 5).

different residence time distributions to simulate observed breakthrough curves of certain solutes. However, only a few temperature models included this in either a steady state [Cozzetto et al., 2006; Story et al., 2003], or dynamic model [Meier et al., 2003; Neilson et al., 2009].

In these models, two processes are responsible for retarded transport of heat: (1) transient storage zones, in which the stream water is retarded and (2) energy exchange with the streambed, in which only heat is retarded. The first can be quantified by simulating observed tracer breakthrough curves (BTC) of a conservative tracer. The second is often described with a diffusion model, taking into account the thermal properties of the sediment and the wetted perimeter of the stream.

Heat exchange between water and the streambed is very sensitive to the contact area, which is often taken to be the same as the wetted perimeter determined with a hydraulic model. Also, the hydraulic models are based on energy losses due to friction (momentum exchange) between water and streambed. This is generally described by a roughness coefficient, which is a different concept to heat exchange. However, it would be desirable if both momentum and heat exchange through the water-streambed interface could be modelled in a coupled fashion.

The objective of this research is to explore and quantify the retardation of heat along a small stream, with the long-term objective of identifying different runoff mechanisms by using heat as a tracer. We developed a transient storage model for non-uniform flow and combined it with an energy balance model. To quantify the different behaviour of water and heat transport, we performed a combined heat-solute tracer test in a first order stream. We used both heat and salt as tracers and observed a significant time lag between the BTC of the two tracers, which could not be explained by heat exchange between the water and the streambed alone. We hypothesize that the delayed arrival time of the heat BTC is partly caused by storage of heat in the streambed and partly by heat exchange with in-stream rock clasts present in the stream.

4.2 Methods

4.2.1 Setup of experiment

Two tracer experiments were performed on 2-Dec-2008 and 3-Dec-2008 (referred to as experiment 1 and 2, respectively), in which water from a 3 m^3 flexible plastic basin was released at the upstream end of the stream. The basin was filled during the hours preceding the experiment by redirecting a portion of the stream flow. During both experiments salt was added to the basin increasing the electrical conductivity (EC) from 520 to 2830 μS cm^{-1} and from 421 to 2220 μS cm^{-1}, respectively. For the second experiment snow was also added, which cooled the water from 7.3 to 0°C (Table 4.1).

During the first experiment the discharge from the basin was approximately 0.5 l s^{-1} for the first 31 min, then 0.7 l s^{-1} for 9 min and 1.7 l s^{-1} during the last 10 min. The release of the

Animation 2: Observed (black line) and simulated (grey line) temperature with hyporheic exchange (see Chapter 5).

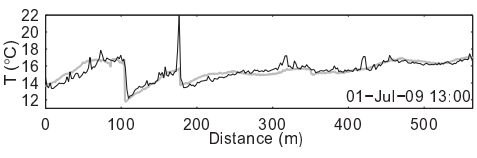

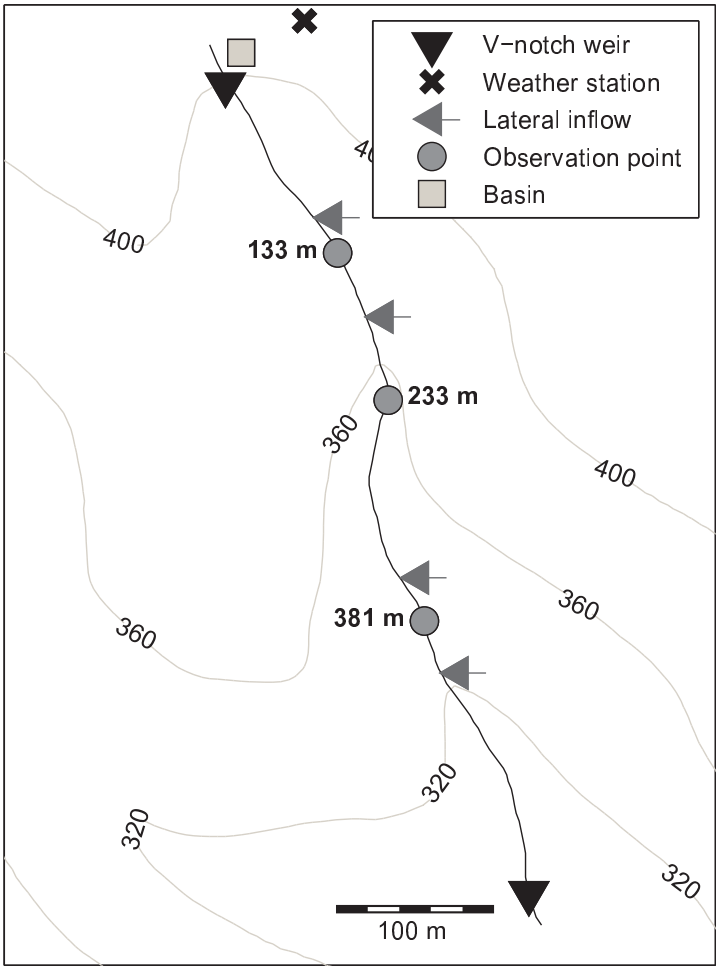

Figure 4.1: Overview of experimental setup

second experiment was constant at $2.0\,\mathrm{l\,s^{-1}}$ for 18 min. During the second experiment, the basin partly blocked the stream, causing an accumulation of water behind the reservoir. This volume then became available during the release of the reservoir.

At three points along the stream (133 m, 233 m and 381 m downstream of the upper V-notch weir. See Fig. 4.1) the breakthrough curves of both the EC and the temperature were measured (handheld conductivity meter 340i, WTW) with an interval of 1 to 5 min, depending on how quickly the EC changed, until the EC was close to its background concentration again. Temperature observations were made for the whole stream, using the DTS.

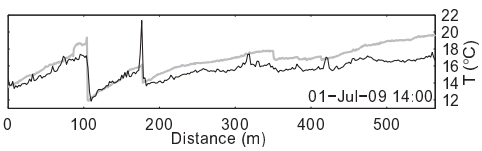

Animation 1: Observed (black line) and simulated (grey line) temperature without hyporheic exchange (see Chapter 5).

4.2.2 Modelling approach

To filter out the effect of the streambed on the advection of heat, we first simulated the breakthrough curves of EC in the first experiment. This experiment also served to calibrate the stream roughness, the dispersion coefficient and the transient storage along the stream. Subsequently, we applied the energy balance model to the first experiment. We calibrated the energy balance model with the DTS observations to determine the temperature of the alluvium. This influences the heat exchange with the riverbed via conduction. Both models were applied to the second experiment for validation.

We simulate the breakthrough curves of EC with a transient storage model [e.g. Runkel, 1998].

$$\frac{\partial(A_w C_w)}{\partial t} + \frac{\partial(Q C_w)}{\partial x} + \frac{\partial}{\partial x}\left(-A_w D \frac{\partial C_w}{\partial x}\right) = \sum q_L C_L + A_w \alpha \left(C_S - C_w\right) \tag{4.1}$$

$$A_S \frac{\partial C_S}{\partial t} = A_w \alpha \left(C_w - C_S\right) \tag{4.2}$$

where C is the salt concentration (kg m^{-3}), α is the exchange coefficient between the stream and transient storage (s^{-1}), while subscript $_S$ stands for transient storage. In Eq. (4.2) the cross-sectional area of the transient storage is assumed to be constant over time ($\partial A_S/\partial t = 0$). To include transient storage in the heat transport model, we adapted Eq.(3.3) to:

$$\begin{aligned} &\frac{\partial(A_w T_w)}{\partial t} + \frac{\partial(Q T_w)}{\partial x} + \frac{\partial}{\partial x}\left(-A_w D \frac{\partial T_w}{\partial x}\right) \\ &= \sum q_L T_L + A_w \alpha \left(T_S - T_w\right) + \frac{W \Phi_{atm}}{\rho_w c_w} + \frac{P \Phi_{cond}}{\rho_w c_w} \end{aligned} \tag{4.3}$$

while writing Eq. (4.2) as:

$$A_S \frac{\partial T_S}{\partial t} = A_w \alpha \left(C_w - T_S\right) \tag{4.4}$$

Table 4.1: Details of the tracer experiments.

	T_{BF} (°C)	T_{basin} (°C)	$EC_{initial}$ (μS cm^{-1})	EC_{basin} (μS cm^{-1})	$Q_{baseflow}$ [a] (l s^{-1})	Q_{basin} l s^{-1}
Exp 1	8.4	8.3	520 ± 3	2830 ± 14	2.4 ± 0.1	0.5 ± 0.3 for 31 min
						0.7 ± 0.04 for 9 min
						1.7 ± 0.06 for 18 min
Exp 2	7.3	0	421 ± 3	2220 ± 11	3.2-4.1 [b] ± 0.1	2.0 ± 0.07 for 18 min

[a] Baseflow observed at the upper V-notch weir.

[b] Just before the start of the experiment, the discharge was 3.2 l s^{-1}, while just after the basin was emptied a discharge of 4.1 l s^{-1} was observed.

Animation 2: Observed (black line) and simulated (grey line) temperature with hyporheic exchange (see Chapter 5).

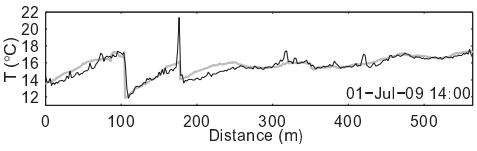

During the experiment, we observed a delayed arrival time of heat, compared to the solute, which could not be explained by heat exchange between the water and the streambed alone (see Section 4.3.3). To simulate this retarded transport of heat along the stream, we added an extra term to Eq. (4.4) to account for storage of heat in in-stream rock clasts:

$$\rho_w c_w \frac{\partial A_w T_w}{\partial t} + \rho_r c_r \frac{\partial A_r T_r}{\partial t} + \rho_w c_w \frac{\partial Q T_w}{\partial x} + \rho_w c_w \frac{\partial}{\partial x}\left(-A_w D \frac{\partial T_w}{\partial x}\right) = \rho_w c_w \sum q_L T_L + \rho_w c_w \alpha A_w (T_S - T_w) + W_b \Phi_{atm} + P_b \Phi_{cond} \tag{4.5}$$

where subscript $_r$ stands for in-stream rock clasts. If we now assume that the heat exchange between the water and the rock clasts is instantaneous; meaning the temperature of rock clasts is always the same as the stream water temperature, the first two terms in Eq. (4.5) can be combined, simplifying the equation to:

$$\rho_b c_b \frac{\partial (A_b T_w)}{\partial t} + \rho_w c_w \frac{\partial (Q T_w)}{\partial x} + \rho_w c_w \frac{\partial}{\partial x}\left(-A_w D \frac{\partial T_w}{\partial x}\right) = \rho_w c_w \sum q_L T_L + \rho_w c_w A_w \alpha \left(T_S - T_w\right) + W \Phi_{atm} + P \Phi_{cond} \tag{4.6}$$

were ρ_b and c_b are the density (kg m^{-3}) and the specific heat capacity (J kg^{-1} °C^{-1}) of the weighted average of water and rock clasts present in the stream. They are given by $\rho_b = (1-\eta)\rho_w + \eta\rho_r$ and $c_b = (1-\eta)c_w + \eta c_r$. η is the fraction of rock clasts in the total cross-sectional area of the stream, and $(1-\eta)$ is the fraction of water present in the total cross-sectional area of the stream. A_b is bulk cross-sectional area, meaning the cross-sectional area of both water and rock clasts, and is given by $A_w/(1-\eta)$.

Calibration was performed on the resistance term, the dispersion term (D), and the transient storage terms (A_S and α). The EC of the lateral inflows (C_L) was determined by matching the initial observed EC at the observation points. The resistance term consists of two components, namely the Manning coefficient and a term accounting for Carnot losses [Chanson, 2004]. The latter is included because the rock clasts in the stream function as numerous small rapids, causing flow expansions and thus energy dissipation. The rock clasts are partly submerged during the peak flow. This reduces the number of rapids, thereby reducing the total resistance of the streambed. Both terms account for energy losses in the hydraulic model and are optimized by mimicking peak arrival times of the observed BTCs of EC.

4.2.3 Determination of initial discharge profile

In a stream where several inflows and outflows are present, it is important to know the initial longitudinal discharge profile. To obtain an estimate of the initial discharge at the three observation points, we determined the volume of the flood wave as:

$$V_{new} = \int_{t=0}^{\infty} Q_{BF} \frac{C_{tot}(t) - C_{BF}}{C_{new} - C_{BF}} \mathrm{d}t \tag{4.7}$$

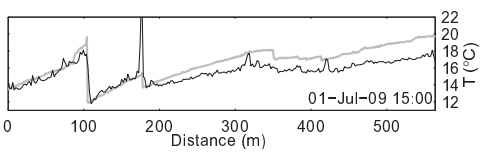

Animation 1: Observed (black line) and simulated (grey line) temperature without hyporheic exchange (see Chapter 5).

where V_{new} is the volume of the new water at the observation point (m^3), Q_{BF} is baseflow or initial discharge at the same point ($m^3\ s^{-1}$), and C_{new}, C_{BF} and C_{tot} are the EC of the water in the basin, the background EC at the observation point and the EC of the mixed water ($\mu S\ cm^{-1}$), respectively.

V_{new} should correspond with the total volume of water released from the basin minus the losses between the observation points and the basin. Other constraints that should be met are:

- The upstream discharge plus all positive and negative exchange flows should equal the downstream discharge:

$$Q_{down} = Q_{up} + \sum Q_L \tag{4.8}$$

  where the subscripts $_{down}$, $_{up}$ and $_L$ are the downstream V-notch weir, the upstream V-notch weir and the lateral inflows and outflows, respectively. The relative contributions of the four biggest inflows were estimated with Eq (3.5). The outflows of water were estimated using Eq. (4.8) and their locations are based on detailed field surveys of discharge distributions along the stream throughout the year. For example, during very dry conditions, the stream disappears completely just upstream of observation point 1. During such a dry spell, $0.3\ l\ s^{-1}$ infiltrated. This can be seen as a lower boundary to constrain the number of solutions determining the initial discharge profile.
- The upstream EC plus all sink and source terms should equal the observed EC at observation point i during baseflow:

$$Q_{BFi} = \frac{Q_{up}C_{up} + \sum Q_L C_L}{C_{BFi}} \tag{4.9}$$

  where $\sum Q_L C_L$ are all lateral inflows between the upstream V-notch weir and observation point i.

To meet all constraints, the initial discharge profile is obtained iteratively.

The initial discharge profiles for the two experiments are different due to significant snowfall between the two experiments. We assumed that the total snowmelt along the stream is the amount needed to close the water balance between the upstream and downstream V-notch weir. The EC of snow is taken to be 20 $\mu S\ cm^{-1}$.

4.3 Results

4.3.1 Initial discharge profile

Just before the start of the first experiment, the upstream and downstream discharge values were $2.4\ l\ s^{-1}$ and $4.4\ l\ s^{-1}$ (Fig. 4.2). The volume of the basin was $2.48\ m^3 \pm 10\%$ (this was estimated by measuring the outflow over time, which has an error of ~10%). The initial discharge values

Animation 2: Observed (black line) and simulated (grey line) temperature with hyporheic exchange (see Chapter 5).

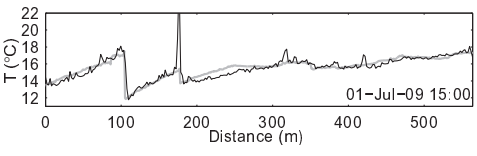

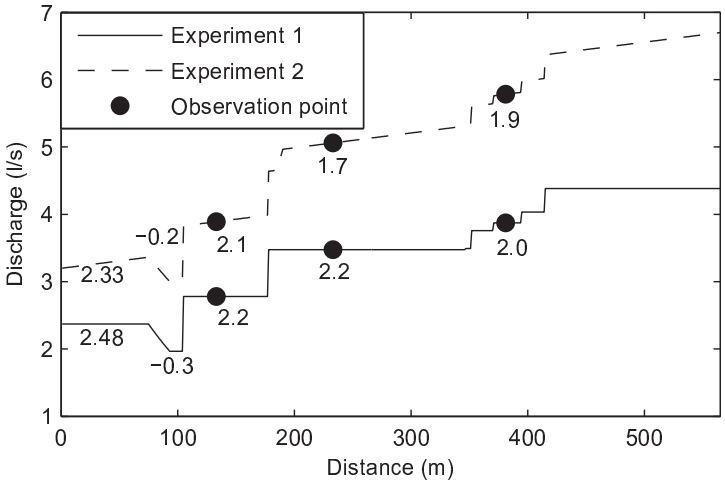

Figure 4.2: Initial discharge profiles for both experiments. The numbers show the estimated volumes, V_{new}, of the basin at the observations points. The numbers -0.2 and -0.3 indicate the volumes of new water which are lost.

at the three observation points were 2.8, 3.5 and 3.9 l s^{-1}, resulting in new water volumes, V_{new}, of 2.2, 2.2 and 2.0 m^3. We estimated the loss of water upstream of observation point 1 to be 0.4 l s^{-1}, resulting in a loss of 0.3 m^3 of new water. The small inflows at 370 and 395 m have been observed in the field, but they were too small to quantify using a mass balance. Therefore they are quantified by closing the water balance, with the constraint that they are smaller than 5% of the discharge in the stream. Due to significant snowfall between the two experiments, the initial discharge profile of the second experiment was more uncertain. For this profile we added two extra sources of lateral inflow, in addition to the lateral inflows determined for the first experiment. Between 185 and 190 m overland flow was observed and estimated to be 0.3 l s^{-1}. To close the water balance we have set the snowmelt to be 1.25 l s^{-1} uniformly distributed along the stream (Fig. 4.2). Due to the unknown distribution of snowmelt, we were unable to obtain realistic volume estimates at observation points 2 and 3.

4.3.2 Breakthrough curves of EC

For experiment 1, the simulated BTCs of EC match the observed BTC reasonably well (Fig. 4.3A), with a RMSE of 71 μS cm^{-1} (Nash-Sutcliffe=0.89). The values of the calibrated parameters are given in Table (4.2). The upstream EC was determined as a weighted average of the EC of the baseflow and the 'new' water. The simulated BTCs all arrive 1 or 2 min too early. The timing of the peaks are good, while the tail is too short in the simulations. Without further calibration we applied the transport model to the second experiment, which gave a RMSE of 108 μS cm^{-1} (Nash-Sutcliffe=0.76) (Fig. 4.3B). The poorer performance is mainly caused by

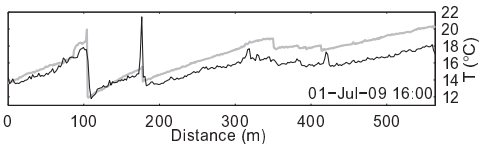

Animation 1: Observed (black line) and simulated (grey line) temperature without hyporheic exchange (see Chapter 5).

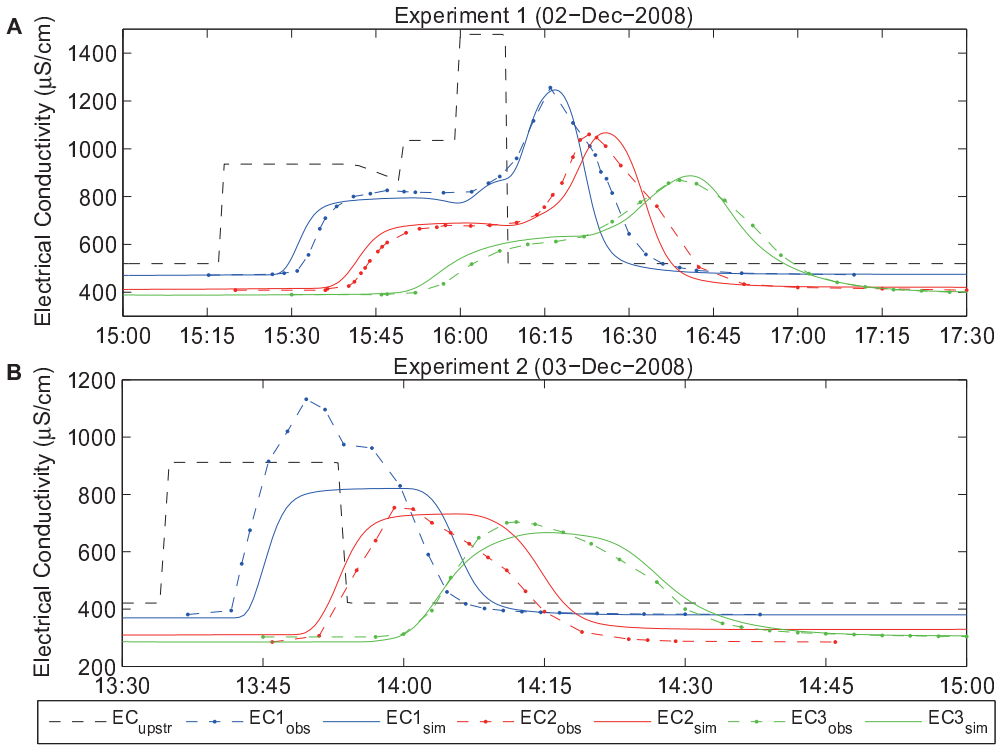

Figure 4.3: Observed and simulated BTC of EC for (A) experiment 1 and (B) experiment 2.

the poor fit of the BTC at observation point 1. The timing of the first arrival time of the BTC at observation points 2 and 3 is better than during the first experiment, and the shape of the tail also looks better, although, the timing is too late.

4.3.3 Breakthrough curves of heat

Looking at the observed BTC of heat (only during the second experiment) a time lag can be observed between the peak arrival time of EC and heat (Fig. 4.4). Going downstream (from observation point 1 to 3) the time lag increases. To be able to simulate this time lag, we optimized the fraction of rock clasts in the stream using experiment 2. The optimal value is found to be 0.35 (Fig. 4.5: for comparison we added the black line indicating the points of the lowest simulated temperatures during experiment 2). Except for the fraction of rock clasts, no further calibration was done: the same parameters were used as during the first experiment. The RMSE of experiment 1 is 0.22 °C (Nash-Sutcliffe=0.89) and 0.23 °C (Nash-Sutcliffe=0.90) for the second experiment.

Animation 2: Observed (black line) and simulated (grey line) temperature with hyporheic exchange (see Chapter 5).

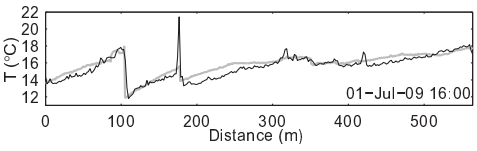

4.4 Discussion

4.4.1 Breakthrough curves of EC and heat

As stated in Section (4.2.2), a reliable routing model (including transient storage zones) is needed to see the net effects of the streambed on the advection of heat. The routing model for the first experiment appears reliable, resulting in good simulations of the BTC of EC. However, in the second experiment the model performance is worse.

First of all, the initial discharge profile during the second experiment is not as clear as during the first experiment due to snowfall the night before, and snowmelt just before and during the experiment. In other words: the stream conditions were changing during the experiment. This results in unreliable estimates of Q_{BF}, using Eq. (4.7).

Secondly, the maximum observed EC at observation point 1 is higher than the maximum EC determined at the upstream boundary. This is physically not possible unless there is an inflow with a high EC (which we did not observe in the field). The EC of the new water was not measured directly, but determined as a weighted average of the EC of the baseflow and the new water. Therefore it is sensitive to both the baseflow and the new water discharge. Due to the uncontrolled release of the accumulated water behind the basin, the baseflow was uncertain during the experiment.

Initially we assumed that there was a constant release of the accumulated water behind the basin during the 18 min it took to empty it. However, it is likely that the accumulated water behind the basin only became available when part of the water from the basin had been released (as the obstruction was removed). If it is assumed that the obstruction was still functioning during the first 6 min, and that the accumulated water was released in the following 12 min at a constant rate, the shape of the simulated EC at the observation points corresponds much better with the observations (Fig. 4.6), resulting in a RMSE of 100 μS cm^{-1} (Nash-Sutcliffe=0.79). However, the peak of the simulated EC at point 1 is still much lower than the observed, implying further uncertainty in the flow regime, probably due to a variable inflow distribution from snowmelt along the stream. The homogeneous distribution of the snowmelt in our simulations is likely responsible for the fact that although the BTC at point 1 is simulated too low, BTCs at the two downstream observation points are simulated correctly. If the snowmelt upstream of point

Table 4.2: Calibrated values of D, C_L, A_S and α.

D (m^2/s)	0.2	
C_L (μS cm^{-1})	190	
	75-100 m	234-345 m
A_S (m^2)	0.006	0.010
α (s^{-1})	0.0010	0.0014

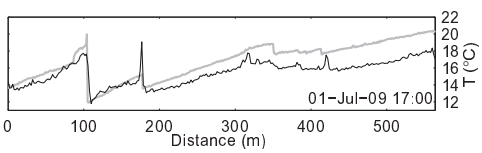

Animation 1: Observed (black line) and simulated (grey line) temperature without hyporheic exchange (see Chapter 5).

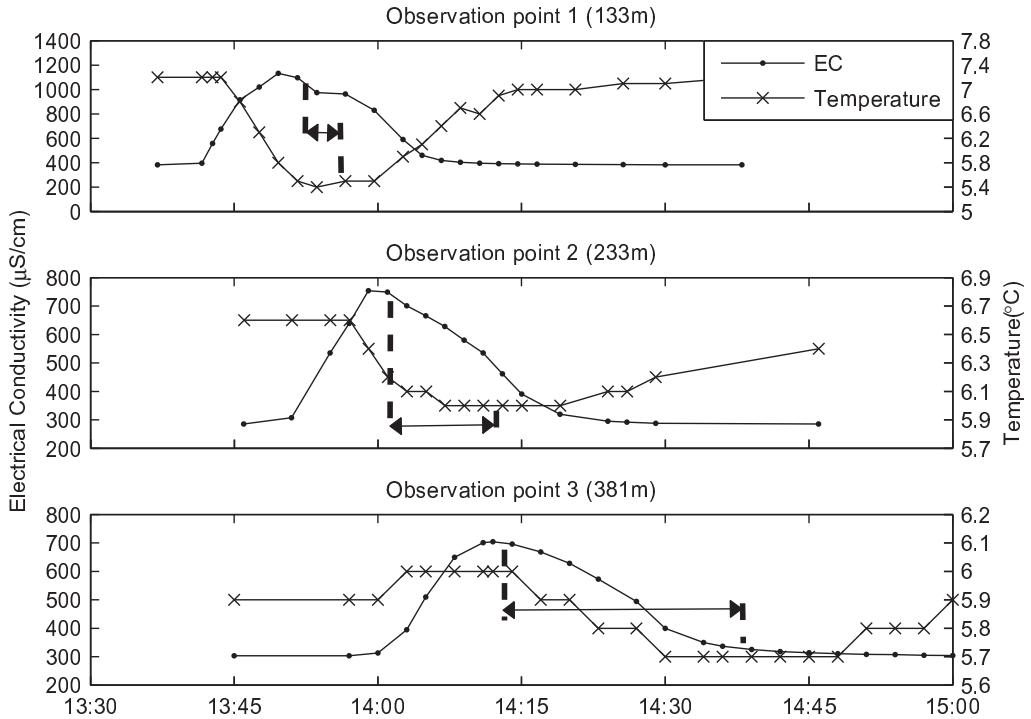

Figure 4.4: Observed BTCs of EC and temperature (measured with the handheld conductivity meter) at the three observation points for experiment 2. The red lines indicate the time lag between the peak arrival times of EC and heat.

1 is less, and is corrected with extra snowmelt between point 1 and 2, the first BTC will be simulated better, while the BTCs at point 2 and 3 remain the same.

Because the spatial distribution of preferential snowmelt pathways is unknown, we assumed a constant snowmelt of 1.25 l s^{-1} uniformly distributed over the length of the stream. By redistribution of the snowmelt contribution and the related base flows, a better fit could be obtained, but we cannot confirm this with observations.

A peculiar phenomenon can be observed in Fig. (4.5). Downstream of the inflow point at 175 m the lowest temperature occurs earlier than just upstream of this point. This phenomenon is visible in both the observed and the simulated temperature. This is caused by the fact that the flood wave travels faster than the thermal wave (Fig: 4.7). At 175 m a relatively warm inflow enters the stream and mixes with the stream water. If the stream discharge is high, the inflow

Animation 2: Observed (black line) and simulated (grey line) temperature with hyporheic exchange (see Chapter 5).

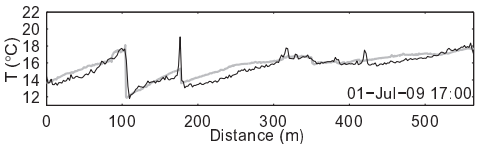

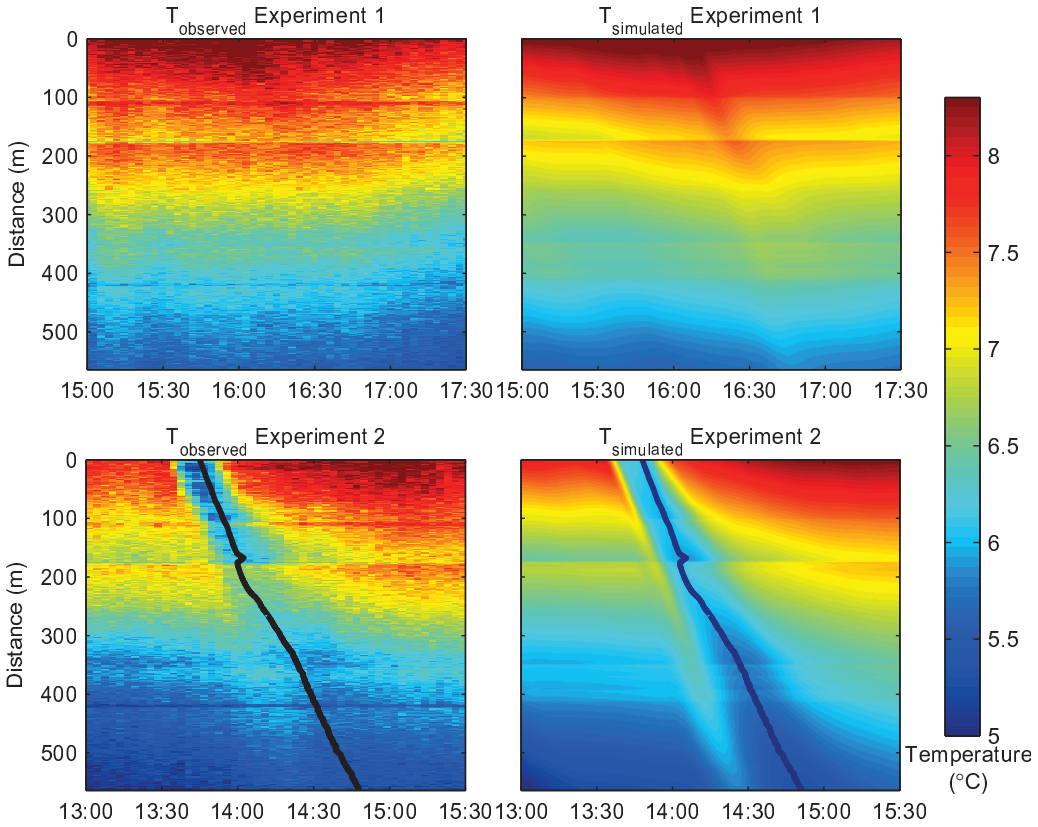

Figure 4.5: Observed and simulated temperature for both experiments. The black lines indicate the lowest simulated temperature and are shown to compare the advection of the thermal wave of the observed and the simulated temperature.

does not heat up the stream as much as when the stream discharge is low. In Fig. (4.7) it can be seen that downstream of the inflow, the coldest water passes when the discharge is still high.

4.4.2 Storage of heat in the rock clasts

Our objective was to explore and quantify the retardation of heat along a small stream. We found a significant time lag between the arrival times of EC and heat, which we could not explain with heat exchange with the streambed alone. We hypothesize that the in-stream rock clasts store heat as well. If the heat exchange between the rock clasts and the water is fast enough, the rock

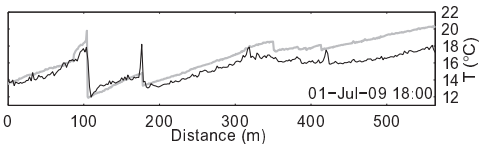

Animation 1: Observed (black line) and simulated (grey line) temperature without hyporheic exchange (see Chapter 5).

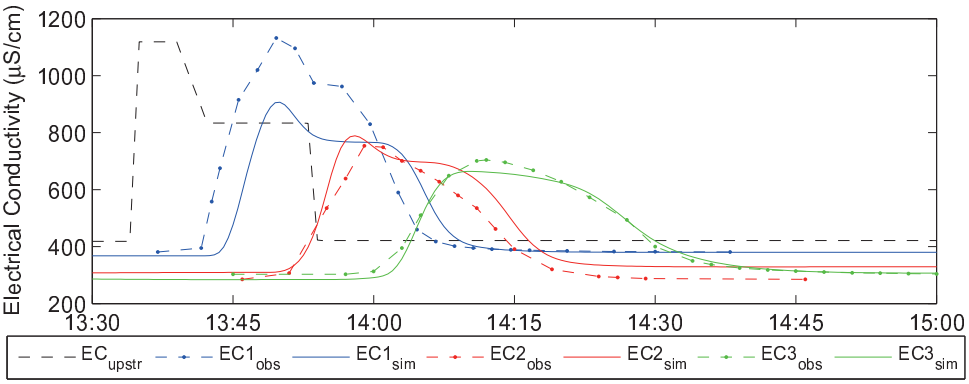

Figure 4.6: Simulated EC of experiment 1, if the accumulated water behind the basin is released 6 min after the start of the experiment. This changes the flow regime in the stream and the simulated upstream boundary condition of EC.

clasts in the stream have the same temperature as the stream water. Using this assumption, we only have to increase the cross-sectional area of the stream with the fraction of rock clasts, which slows down the advection of heat. This phenomenon was earlier described for vertical groundwater flow [e.g. Blasch et al., 2007; Constantz and Thomas, 1996; Silliman et al., 1995; Stallman, 1965; Taniguchi and Sharma, 1990]. However, in these studies the objective was to determine percolation rates, given the porosity (which is the similar to 1 minus the fraction of rock clasts) of the medium. Here, we use the fraction of rock clasts in the cross-sectional area of the stream to determine transit times of heat. In larger streams, and in streams with a sandy or gravel streambed, the fraction of rock clasts in the cross-sectional area is close to zero. However, if we apply a fraction of rock clasts of 0 in our simulations (which is the same as applying Eq. 4.4), the thermal wave travels too fast. The black line in Fig. (4.8A) and (4.8B) is the line of the lowest temperature using a fraction of 0.35, the red line in Fig. (4.8B) indicates the line of the lowest temperature if a fraction of 0 is used (no storage of heat in rock clasts).

A simplification in our modelling approach is that we assume that the rock clasts have the same temperature as the surrounding water. To test this assumption, we considered a flat rock clast with a thickness of 2 cm, subject to a temperature change at both sides of the rock clast of 4°C per hour (this was the maximum observed temperature change of the water during a studied period in July 2009; see Chapter 5). Numerical simulations showed that the temperature at the middle of the stone is always within 0.06°C from the outside temperature. Because most of the rock clasts are smaller than this, while the contact area between water and rock clasts is larger than considered in this calculation, the assumption that $T_w = T_r$ seems valid. Only a few larger rock clasts violate this assumption, but their relative contribution is minor. A disadvantage of

Animation 2: Observed (black line) and simulated (grey line) temperature with hyporheic exchange (see Chapter 5).

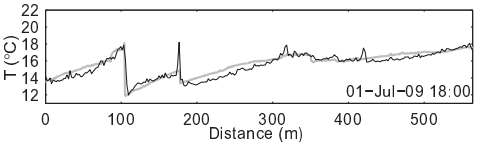

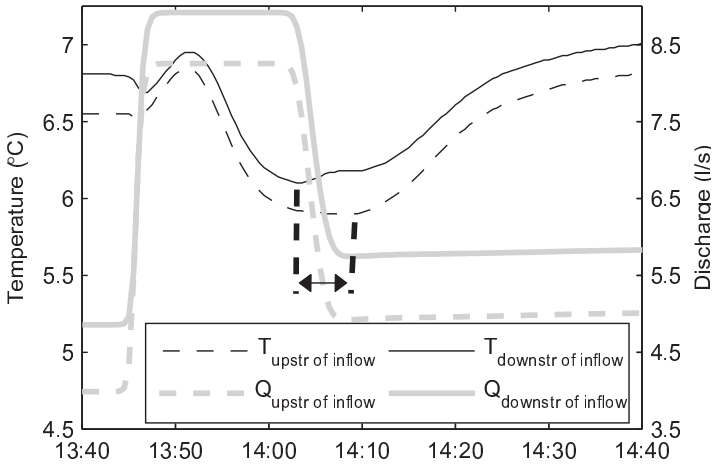

Figure 4.7: Simulated temperature and discharge just upstream and downstream of the inflow point at 175 m. The lowest temperature downstream of the inflow, occurs earlier in time than the lowest temperature upstream of the inflow.

applying this method in an open stream, compared to vertical groundwater flow, is that the cross-sectional area of the stream varies with varying discharge, making the fraction of rock clasts dynamic as well. Therefore we suggest using the fraction of rock clasts as a calibration parameter.

The big advantage of this method is that a hydraulic model can easily be coupled with an energy balance model. All flow parameters, such as the flow velocity, cross-sectional area and wetted perimeter, can be directly used in the energy balance model, while only one extra parameter (fraction of rock clasts in the stream) is needed to account for the retarded advection of heat, caused by the rock clasts in the stream.

4.5 Conclusion

Temperature contains information for a wide variety of hydrological processes. With the introduction of DTS into the field of hydrology, temperature observations have become available in both space and time. The long-term objective of our study is to identify different runoff mechanisms focusing on the detection of groundwater discharge zones using heat as a tracer. However, the interpretation of the observed temperature signal is often not straightforward, due to its non-conservative behaviour. Therefore, coupled hydraulic-energy balance models are needed. One might ask why we should use a non-conservative tracer in stream hydrology instead of working with a conservative tracer like salt. In our opinion, the answer is found in the very

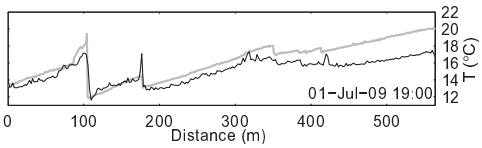

Animation 1: Observed (black line) and simulated (grey line) temperature without hyporheic exchange (see Chapter 5).

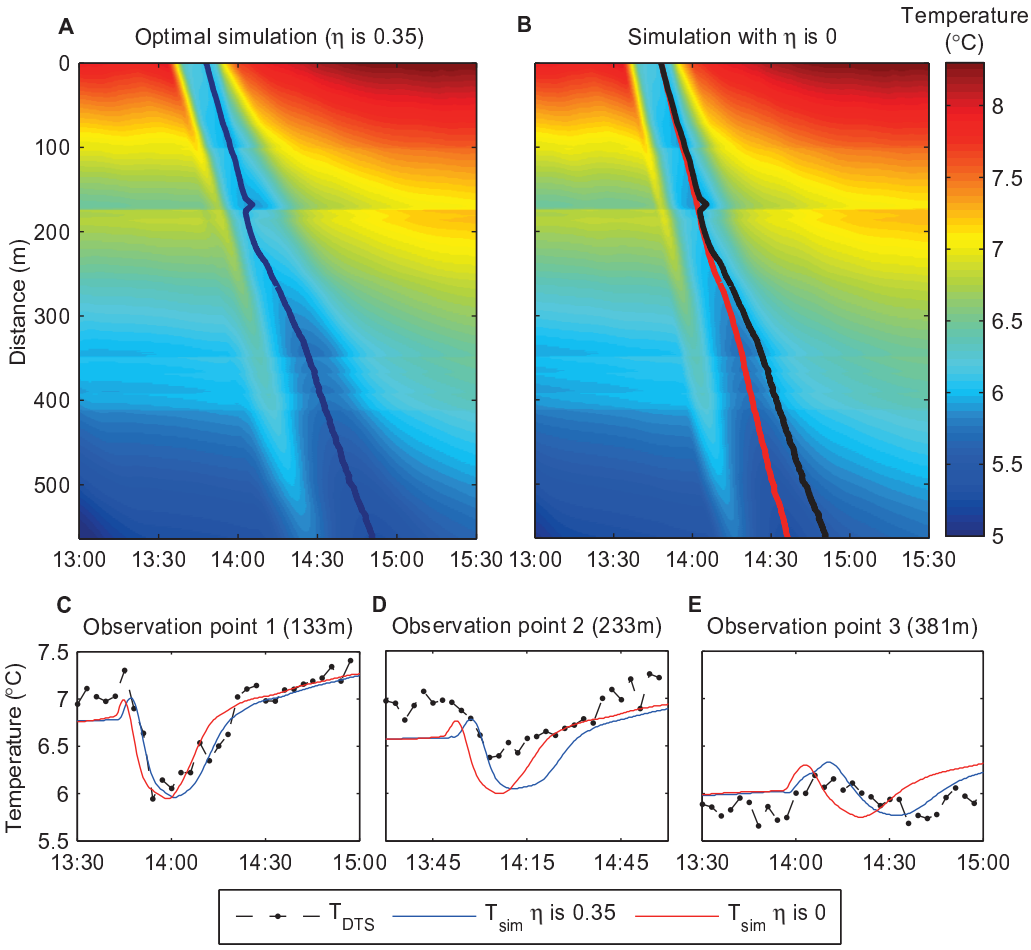

Figure 4.8: Simulated temperature during experiment 2 for (A) the optimized fraction of rock clasts, (B) for the case when no heat is stored in rock clasts, present in the stream and (C-E) the observed (with DTS) and the simulated thermal waves at the three observation points. The black lines in (A) and (B) indicate the line of lowest temperature of the optimized simulation and the red line indicates the line of lowest temperature without storage of heat in rock clasts.

high spatial and temporal resolution of the measurements and the high accuracy/precision of the temperature observations. We believe this outweighs the extra effort put into energy balance modelling to reduce the uncertainty associated with its nonconservative behaviour.

In this study we carried out a tracer experiment using salt and heat as a tracer. We observed a significant time lag between the breakthrough curves of both tracers, with salt travelling faster

Animation 2: Observed (black line) and simulated (grey line) temperature with hyporheic exchange (see Chapter 5).

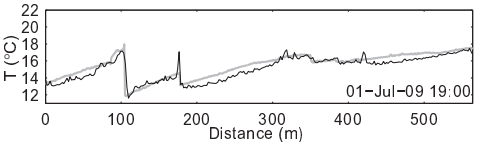

than heat. We hypothesize that, besides transient storage zones (in our case the hyporheic zone is most important), heat BTCs can be retarded by heat exchange with the streambed as well as with the in-stream rock clasts. To simulate the delayed arrival time of heat, we propose accounting for the fraction of rock clasts present in the total cross-sectional area of the stream, in which heat is stored as well. This is simply done by increasing the cross-sectional area in the advection-dispersion equation, with the assumption that the rock clasts have the same temperature as the surrounding water. Applying this method makes it possible to use the hydraulic parameters, such as cross-sectional area and wetted perimeter (determined with the hydraulic model) in the energy balance model. The fraction of in-stream rock clasts then accounts for a larger cross-sectional area in the storage term of the advection-dispersion equation, thus slowing down the advection of heat. This is a pragmatic solution, which makes it easy to couple a hydraulic model with an energy balance model, while still accounting for the slower advection of heat.

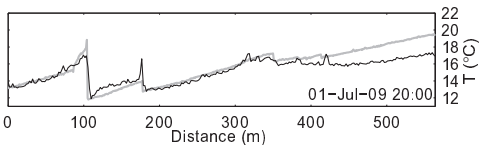

Animation 1: Observed (black line) and simulated (grey line) temperature without hyporheic exchange (see Chapter 5).

Chapter 5

Quantifying hyporheic exchange at high spatial resolution using natural temperature variations along a first order stream†

Abstract. *Hyporheic exchange is an important process that underpins stream ecosystem function, and there have been numerous ways to characterize/quantify exchange flow rates and hyporheic zone size. The most common approach, using conservative stream tracer experiments and 1D solute transport modeling, results in over-simplified representations of the system. Here we present a new approach to quantify hyporheic exchange and the size of the hyporheic zone (HZ) using high-resolution temperature measurements and a coupled 1D transient storage and energy balance model to simulate in-stream water temperatures. Distributed Temperature Sensing was used to observe in-stream water temperatures with a spatial and temporal resolution of 2 m and 3 min, respectively. The hyporheic exchange coefficient (which describes the rate of exchange) and volume of the HZ were determined to range between 0 to 2.7e-3 s^{-1} and 0 to 0.032 m^3m^{-1}, respectively, at a spatial resolution of 1-10 m by simulating a time series of in-stream water temperatures along a 565 m stretch of a small first-order stream in central Luxembourg. As opposed to conventional stream tracer tests, two advantages of this approach are that exchange parameters can be determined for any stream segment over which data has been collected and that the depth of the HZ can be estimated as well. Although the presented method was tested on a small stream, it has potential for any stream where rapid temperature change (with regard to time) of a few degrees can be obtained.*

†. *Based on: Westhoff, M. C., Gooseff, M. N., Bogaard, T. A., Savenije, H. H. G., 2011 (accepted). Quantifying hyporheic exchange at high spatial resolution using natural temperature variations along a first order stream. Water Resour. Res*

Animation 2: Observed (black line) and simulated (grey line) temperature with hyporheic exchange (see Chapter 5).

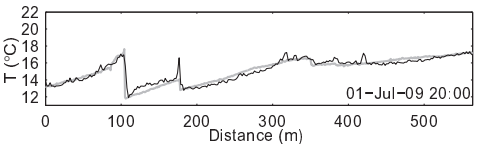

5.1 Introduction

Stream water-groundwater interactions (hyporheic exchange) may influence stream water quality significantly [Findlay, 1995]. In this study we defined the hyporheic zone as the subsurface volume of alluvial aquifer through which stream water exchanges, although we recognize that different disciplines may define the hyporheic zone differently [Krause et al., 2010]. However, it is often difficult to either quantify hyporheic exchange or to locate the extent of the hyporheic zone.

Different approaches have been applied to quantify the hyporheic exchange or to identify the hyporheic zone. Vertical hydraulic gradients have been measured to identify zones of upwelling and downwelling stream water [Anderson et al., 2005]. Ward et al. [2010] successfully used Electrical Resistivity Tomography (ERT) to visualize the hyporheic zone during a stream tracer test using dissolved salt as a conservative tracer. Groundwater models have also been developed to investigate hyporheic exchange. Gooseff et al. [2006] used a 2D groundwater model and showed the effect different bed forms and stream sizes have on hyporheic exchange. Residence time distributions of exchange over different spatial scales of exchange have been investigated by using groundwater flow models [Cardenas, 2008]. Such approaches have also elucidated the influence of stream sinuosity and larger groundwater flow boundary conditions on hyporheic zone extent and exchange [Cardenas, 2009]. However, Wondzell et al. [2009] showed that due to equifinality (i.e. different model parameterizations give similarly good model outcomes [e.g. Beven and Freer, 2001]) in groundwater models the simulated hyporheic exchange can differ significantly with different hydraulic conductivities, while observed groundwater heads were simulated well.

Another approach to characterize hyporheic exchange is to analyze in-stream tracer breakthrough curves with 1D transient storage models [e.g. Bencala and Walters, 1983; Runkel, 1998]. However, Harvey and Wagner [2000] showed that this approach is sensitive to experimental setup (i.e., the "window of detection"), such as the length of the experimental reach, and Wörman and Wachniew [2007] showed that the chosen 'goodness of fit' parameter to quantify the model performance, also influences the analysis of the observed breakthrough curves. Nevertheless, this approach has been widely used to infer size of hyporheic zones and their influence on solute transport in streams [e.g. Haggerty et al., 2000, 2002; Gooseff et al., 2003, 2005; Zarnetske et al., 2007].

A general complication of the 1D transient storage model is that the transient storage zone represents both in-stream transient storage zones (e.g. eddies) and hyporheic zones (or even more processes), without distinguishing between the two. Choi et al. [2000] compared a one-zone transient storage model with a two-zone transient storage model. They showed that only if the two transient storage zones have completely different characteristics in terms of exchange rate and volume, the two-zone model outperforms the one-zone model. Briggs et al. [2009] estimated the exchange rate and storage volume of one of the two zones by field observations: in their case they measured the volumes of in-stream transient storage zones as well as the breakthrough

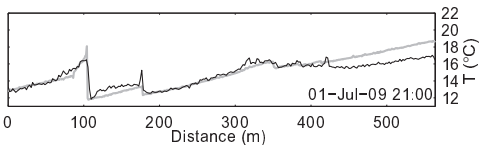

Animation 1: Observed (black line) and simulated (grey line) temperature without hyporheic exchange (see Chapter 5).

curves in these in-stream transient storage zones. However, a major disadvantage of most tracer studies that are designed to quantify hyporheic exchange is that the locations of the observation points should be chosen a priori, and no knowledge about the location of the hyporheic zone beneath the streambed is gained.

The in-stream tracer studies mentioned above all relied upon the application of chemical tracers in the stream or streambed. In this study, we use temperature as a tracer. Temperature has been used as a tracer to identify upwelling or downwelling stream water by analyzing temperature variations at different depths in the streambed [e.g. Stallman, 1965; Lapham, 1989; Silliman et al., 1995; Constantz, 1998; Constantz et al., 2003; Becker et al., 2004; Anderson et al., 2005; Niswonger et al., 2005; Hatch et al., 2006; Keery et al., 2007], though it is a useful stream tracer as well. Hyporheic exchange dampens the stream water temperature oscillations at both the daily and annual timescales [e.g. Poole and Berman, 2001; Burkholder et al., 2008] thus potentially allowing for the quantification of hyporheic dynamics from analysis of temperature dynamics. However, temperature is not a conservative tracer. Heat exchanges occur throughout coupled stream-hyporheic systems. Yet analysis of the energy balance of stream and hyporheic waters is needed [e.g. Brown, 1969; Sinokrot and Stefan, 1993; Kim and Chapra, 1997; Boyd and Kasper, 2003; Becker et al., 2004; Westhoff et al., 2007; Roth et al., 2010]. Such an approach requires extensive information on spatial and or temporal temperature patterns. For example, in cases where hyporheic exchange is an important flux, the temperature of the return flux should be known as well as the stream temperature. Cozzetto et al. [2006] used observed subsurface temperature as an estimate for the temperature of the hyporheic zone. Loheide II and Gorelick [2006] and Westhoff et al. [2010] used simulated subsurface temperatures as a proxy for the temperature of the hyporheic return flux. However, they ignored the fact that the hyporheic exchange can influence subsurface temperature as well. Story et al. [2003] and Neilson et al. [2009] included this effect, assuming that the hyporheic zone only covered the top layer of the streambed. Meier et al. [2003] also included energy exchange with transient storage zones (such as the hyporheic zone), but they only considered the influence of in-stream transient storage zones. All of these studies were constrained by the fact that the locations of the observation points had to be chosen a priori.

The aim of this study is to identify hyporheic exchange at a spatial resolution on the order of 1 to 10 m and to estimate the depth of the hyporheic zone beneath the streambed. This study is unique in that we make use of high-frequency (3 minute interval), high spatial (2 m) resolution temperature observations, which allows us to choose the segments of constant hyporheic exchange parameters after the observations are made (section 5.2.2). We develop and demonstrate results of a heat transport model that accounts for exchange with transient storage zones, and allows us to identify the size of the hyporheic zone and hyporheic exchange fluxes along the study reach. There is significant potential to advance our general understanding of hyporheic exchange, its dynamics through space, and influence on stream ecosystems using this

Animation 2: Observed (black line) and simulated (grey line) temperature with hyporheic exchange (see Chapter 5).

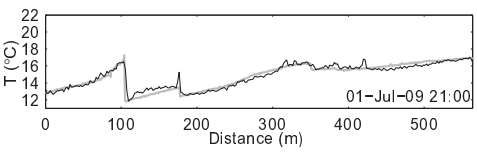

new modelling approach.

5.2 Methods

5.2.1 Improvements to model

In this Chapter, a couple of improvements were made compared to Chapter (4): First of all, we obtained a better representation of the cross-sectional profiles by measuring them with a pin-meter (Fig. 2.4). To differentiate between hyporheic exchange and heat exchange between water and in-stream rock clasts, the cross-sectional areas of the rock clasts were estimated by drawing a contour line around the observed profile. Secondly, at 83 and 312 m from the upstream V-notch weir, temperature loggers (HOBO TMC6-HD sensors connected to an U12-008 logger) monitored the temperature below the stream at depths of 5, 10, 20 and 40 cm at a 30 min interval. These observations were used to better validate our model results.

In the temperature model, improvements were made to be able to simulate the temperature of the hyporheic zone and thus the subsurface. The previous model was unable to simulate the temperature of the hyporheic zone. Therefore, model improvements for this Chapter involved a better description of the vertical subsurface heat conduction and simulation of the temperature of the hyporheic zone. In Chapter (4) we used only two layers of ∼7 cm to simulate heat conduction at subsurface-stream water interface. In this Chapter, however, because we simulate the temperature of the hyporheic zone, we needed to simulate the subsurface temperature to greater depth. Hence, we extended the subsurface model domain to a depth of 1 m below the stream and combined Eq. (3.27) and (4.4):

$$\frac{\partial T_{soil}}{\partial t} = -K_{soil}\frac{\partial^2 T_{soil}}{\partial z^2} + \alpha\frac{A_w}{A_{hz}}(T_w - T_{hz}) + \frac{\beta\Phi_{bed}}{c_b\rho_b \mathrm{dz}} \tag{5.1}$$

where subscript $_{hz}$ replaces $_S$, since we now assume that hyporheic exchange is the only transient storage. The first term on the right hand side of Eq. (5.1) represents the vertical heat conduction in the subsurface; the second term represents the temperature change by hyporheic exchange and the third term the heat conduction between the stream and the first subsurface layer. Note that the second term is only applied at the locations where hyporheic exchange is defined and the third term is only applied at the top layer of the subsurface. In the numerical solution we defined 25 horizontal subsurface layers with a vertical thickness of 4 cm each. At the lower boundary (at 1 m depth) we assumed a constant temperature of 14°C. This temperature was estimated by analyzing the subsurface temperature observations at 83 and 313 m. The hyporheic zone is assumed to be somewhere within this 1 m thick profile (Fig. 5.1), which is reasonable for such a small stream. The thickness of the hyporheic zone is determined as $d_{hz} = A_{hz}/P$. The temperature of the hyporheic return flow is taken as the average temperature of all vertical grid cells where hyporheic exchange was determined. Equation (4.6) was solved explicit, while Eq.

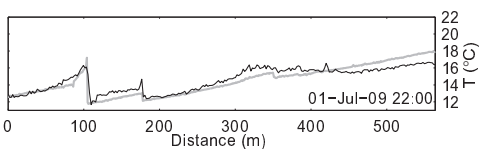

Animation 1: Observed (black line) and simulated (grey line) temperature without hyporheic exchange (see Chapter 5).

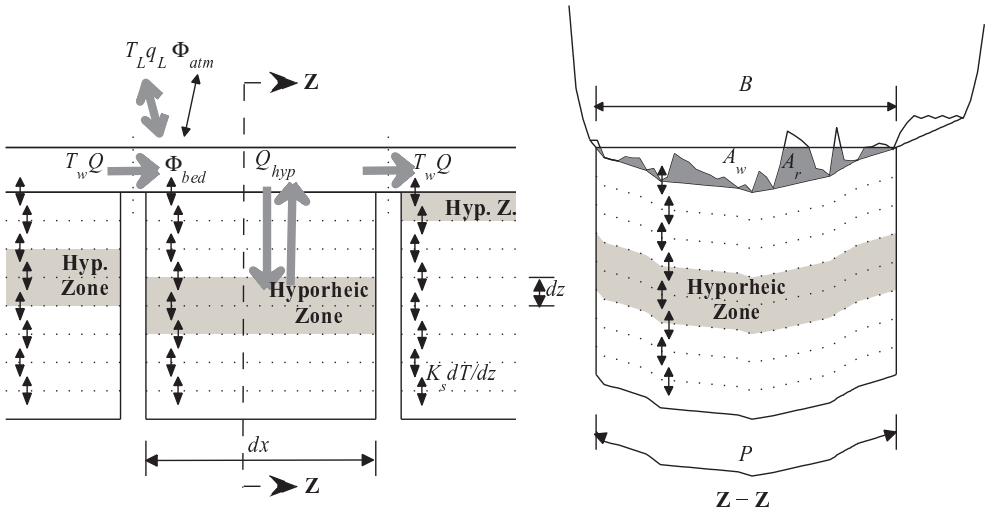

Figure 5.1: Schematic of the 1D advection-dispersion model with transient storage. The grey arrows are water fluxes, the black arrows are energy fluxes. q_{hyp} is the hyporheic flux, given by αA_wdx.

(5.1) was solved with an implicit scheme, all with time steps of 5 s and longitudinal grid cells of 1 m. For the sensible heat flux Eq. (3.25) was used.

5.2.2 Calibration strategy

For this study we focus on two consecutive warm days on July 1 and 2, 2009. In our approach we first determined the discharge profile, after which we calibrated the parameters describing hyporheic exchange.

Stream discharge was observed at the weirs located upstream and downstream of the investigated reach. No direct discharge measurements have been done in-between. Instead we determined the longitudinal discharge profile in an indirect way. The relative contributions of the two major inflows at 351 and 414 m have been determined with a mass balance equation knowing the temperature of the inflow and the temperature just upstream and downstream of the inflow (Eq. 3.5).

This was not possible for the first lateral inflow at 104 m, because upstream of this point the stream was almost dry, leading to very high uncertainty using Eq. (3.5), nor for the lateral inflow at 177 m because its measurement of T_L was influenced by mixed stream water. To determine the discharge of these two lateral inflows, we calibrated the discharge of the stream segment just downstream of the inflow. These two sections (at 108-180 m and 182-234 m), were exposed to solar radiation during two to three hours leading to a rapid increase in temperature (max 8.9

Animation 2: Observed (black line) and simulated (grey line) temperature with hyporheic exchange (see Chapter 5).

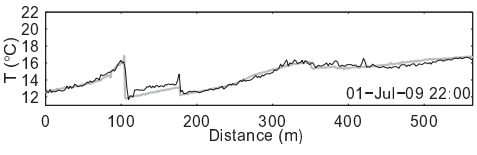

and 4.7°C/100 m for both sections, respectively). Because the temperature increase is linearly dependent on the depth of the stream, a smaller stream depth results in a faster increase in temperature. The stream depth is, in turn, a function of discharge, with lower discharge resulting in shallower depths. The inflows at 383 and 393 m were not monitored, since they were too small to affect in-stream temperature. We estimated both at $Q_L = 0.05Q_d$.

We directly observed the influence of streamflow losses at several locations. The loss of water upstream 93 m has been estimated as 98% of the discharge because the stream was almost dry between 93 and 104 m. For numerical stability, we assumed there was a small fraction of water left in the stream. The location where stream water infiltrated is, as a best guess (based on detailed field surveys), set between 60 and 93 m from the upstream V-notch weir where we assumed for each grid cell the same relative amount of water to infiltrate. The loss between 234 and 248 m was estimated in such a way that the observed upstream discharge plus all gains minus all losses equals the observed downstream discharge. For this loss of water also counts that the location is a best estimate. The sensitivity of the energy budget to these latter three assumptions is minor, but important to maintain the water balance in the model. Fig. 5.2 shows the discharge profile that resulted from the discharge calibration.

We used in-stream temperature observations to calibrate the exchange coefficient (α), the cross-sectional area of the hyporheic zone (A_{hz}) and the average depth of the hyporheic zone. We calibrated these parameters in predefined short segments of the stream (between 40 and 170 m long) to prevent error propagation from upstream to downstream. For each segment, the observed upstream water temperature was taken as boundary condition. The segment boundaries were chosen 2 to 4 m downstream of a lateral inflow or at the upstream end of a completely shaded section. These were the areas where we could constrain the calibration parameters well (see section 5.4.2). The selected segments were 0-106 m (until the first inflow), 108-180 m (between the first and second inflow), 182-350 m (between the second and third inflow), 354-421 m (between the third inflow and the end of a shaded area), 421-465 m (beginning of open area until the start of a shaded area) and 466-565 m (start of a shaded area until the downstream V-notch weir). The small gaps between segments are points where there is a lateral inflow which has to mix completely before we observe a representative water temperature. Within each segment subsections of constant α, A_{hz} and depth of the hyporheic zone were considered, to best fit the observed in-stream temperature. The predefined segments were determined a priori while the selection of subsections was done by trial and error, trying to minimize the number of subsections.

At 83 and 312 m from the upstream V-notch weir we observed subsurface temperature at 5, 10, 20 and 40 cm below the stream using independent temperature sensors. From this we determined the hyporheic exchange parameters α, A_{hz} and depth of the hyporheic zone by simulating subsurface temperature with the vertical temperature diffusion equation (Eq. 5.1). As boundary condition, we used observed stream water temperature. We then varied α, A_{hz} and depth of the

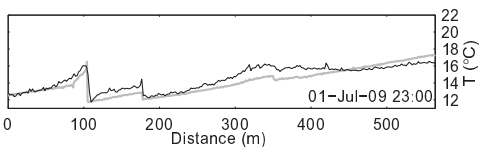

Animation 1: Observed (black line) and simulated (grey line) temperature without hyporheic exchange (see Chapter 5).

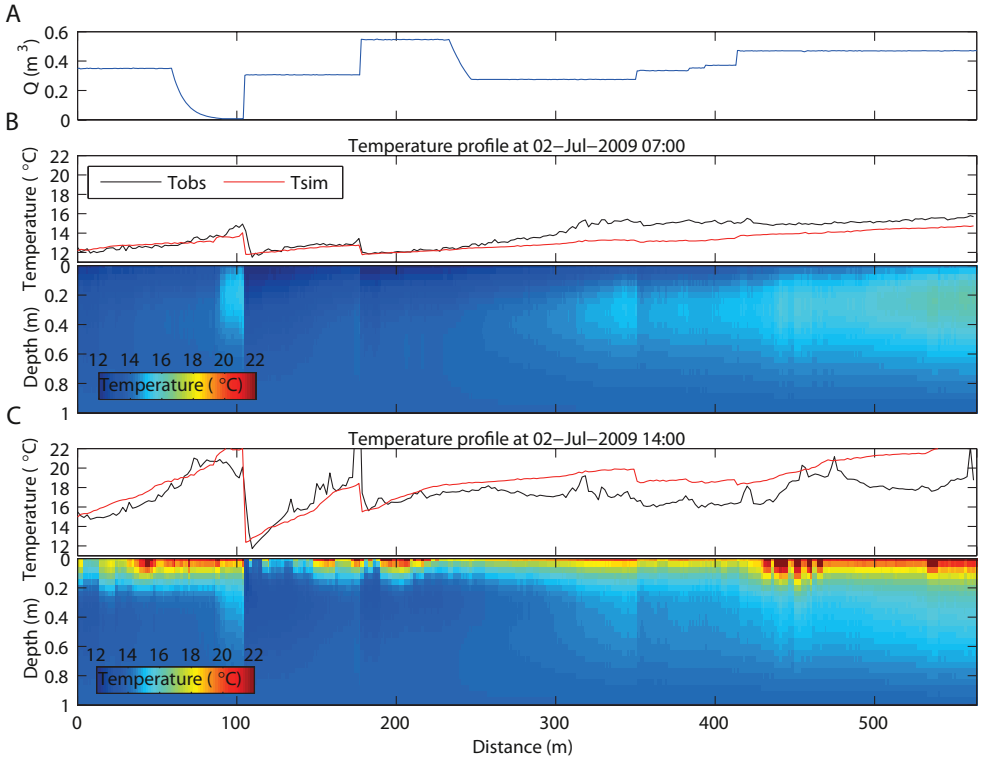

Figure 5.2: Base case simulation without hyporheic exchange, with (A) stream discharge; and observed and simulated stream water temperature with simulated subsurface temperatures at (B) 2-Jul-2009 7:00 and (C) 2-Jul-2009 14:00.

hyporheic zone to minimize the RMSE of observed and simulated temperature at 5, 10, 20 and 40 cm depth. The resulting parameter values for α, A_{hz} and depth of the hyporheic zone were then compared with the parameter values obtained by calibrating on in-stream temperature, as a way of validation. We also compared the observed subsurface temperatures with simulated subsurface temperatures calibrated with in-stream temperatures (as described above).

5.3 Results

As a base case we first simulated the stream water and subsurface temperature without hyporheic exchange, taking only heat exchange with the in-stream rock clasts into account (Fig. 5.2B and C Animation 1[1]). Figure (5.2B) shows the observed and simulated stream water temperature

1. Animation 1 is plotted at the lower left of all even pages between page 1 and 91.

Animation 2: Observed (black line) and simulated (grey line) temperature with hyporheic exchange (see Chapter 5).

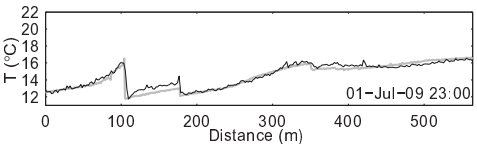

at 2-Jul-2009 07:00 and the simulated subsurface temperature over depth and along the stream. Figure (5.2C) shows the same but for 2-Jul-2009 14:00. Up to 250 m, the temperatures were very well simulated with a RMSE of 0.85°C. Further downstream, the simulated temperatures deviate more strongly from the observed with a RMSE for the whole stream of 1.27°C. During the day, the simulated stream water temperatures are too high and during nighttime too low. This indicates a storage effect of heat where energy is stored during the day and released during the night. Hyporheic exchange is a likely candidate for this phenomenon.

Subsequently we introduced hyporheic exchange into the model. After calibration we ended up with 13 stream segments of constant A_{hz}, α and depth of the hyporheic zone (Fig. 5.3A). The hyporheic exchange buffered the temperature, resulting in a much better fit with a RMSE of 0.65°C (Fig. 5.3B and C, Animation 2[2]). One particular behaviour in the observed stream water temperatures was the occurrence of negative longitudinal temperature gradients visible at 2-Jul-2010 14:00 at 80-100 m, 250-300 m and 470-520 m. Indeed, these stream reaches were never exposed to direct short wave radiation due to the thick canopy cover. But the net energy flux, although small, was still positive due to longwave radiation and sensible heat, indicating that the stream should have been warming-up. Exchange with the relative cooler water in the hyporheic zone made it possible to simulate the observed negative longitudinal temperature gradients.

The observed subsurface temperatures at 83 and 312 m were used for validation. Comparing the simulated subsurface temperatures with the observed, gave a RMSE at 83 and 312 m (averaged for all observed depths) of 0.30 and 0.26°C, respectively (Fig. 5.4, Table 5.1). At 83 m simulated peak temperatures were underestimated, especially during 2-Jul (by 1.3, 0.57, 0.47 and 0.35°C at 5, 10, 20 and 40 cm depth). Also the peak temperature in in-stream water temperature was underestimated at this position by 1.7°C. At 312 m simulated in-stream water temperature was underestimated during peak temperatures by 0.4°C, while at 5, 10 and 20 cm this was only 0.2, 0.1 and 0.25°C. The difference at 40 cm depth was larger with 0.55°C. At 83 and 312 m, we solved for the values of α, A_{hz} and depth of the hyporheic zone independently using the observed subsurface temperature profiles. The values of these parameters are in the same range as the values obtained when calibrating on stream water temperature (Table 5.1).

The influence of the hyporheic zone on the subsurface temperature is best seen in Fig. (5.3C). Hyporheic exchange circulation acts as a heat sink during the day, conducting heat from the stream into the subsurface. This resulted in higher simulated subsurface temperatures than at areas without hyporheic exchange during the day.

The relative influence of the hyporheic exchange, compared with Φ_{atm} and Φ_{cond}, is illustrated in Fig. (5.5). The hyporheic exchange is presented here as $q_{hyp} = \rho_w c_w \alpha (T_{hz} - T_w)$ [W m^{-3}]. Here, Φ_{atm} and Φ_{cond} are also expressed as an energy flux per unit volume [W m^{-3}]. During the night q_{hyp} is positive, while Φ_{atm} and Φ_{cond} are close to zero. During the day, q_{hyp} is a cooling flux which can be, in absolute terms, larger than Φ_{atm}.

2. Animation 2 is plotted at the lower right of all odd pages between page 1 and 91.

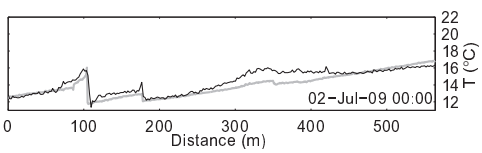

Animation 1: Observed (black line) and simulated (grey line) temperature without hyporheic exchange (see Chapter 5).

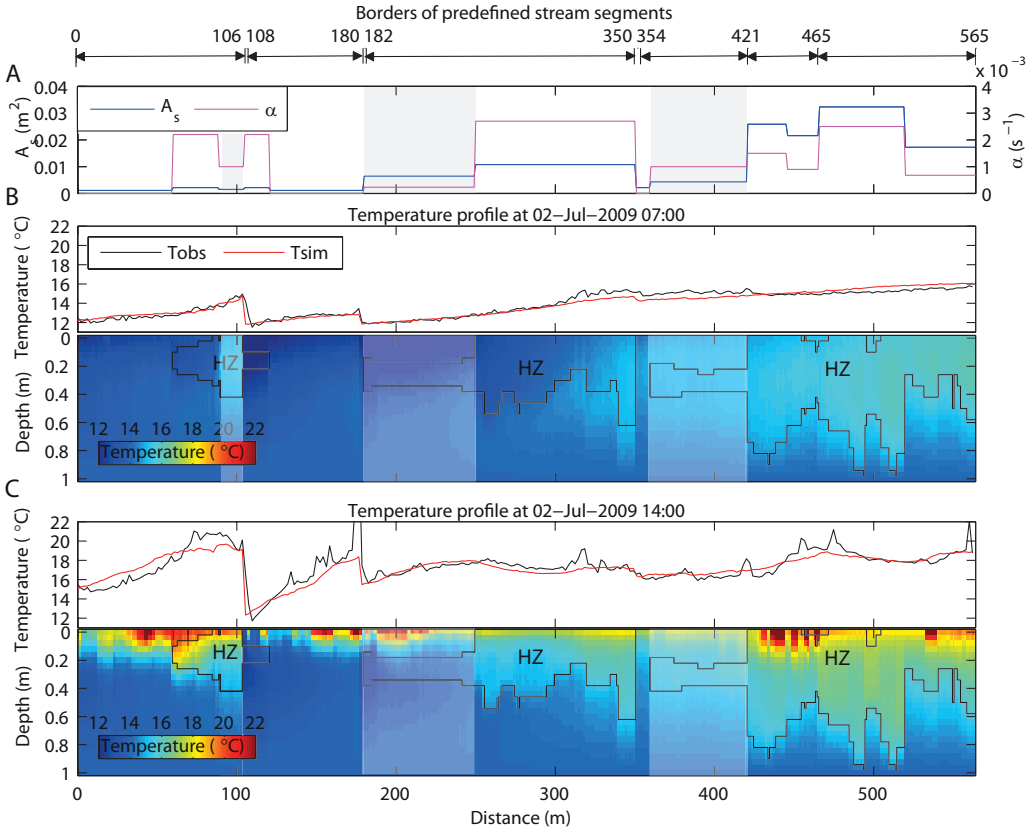

Figure 5.3: Optimal solution with (A) values of A_{hz} and α along the stream; and observed and simulated stream water temperature with simulated subsurface temperatures at (B) 2-Jul-2009 7:00 and (C) 2-Jul-2009 14:00. The black lines in the subsurface temperature panels visualize the thickness and depth of the hyporheic zone for each Δx. The transparent boxes indicate areas where hyporheic exchange parameters were poorly identifiable. On top the a priori determined stream segments are indicated. Note that in the results shown here, simulated temperatures were not corrected at segment boundaries.

5.4 Discussion

5.4.1 Limitations

Since each model is a simplification of the real world, several assumptions had to be made. In our case, we showed excellent model performance for simulated stream water temperatures. Here we discuss the validity of our assumptions.

No lateral hyporheic exchange was taken into account. This means that downwelling hyporheic water returns to the stream within the same grid cell. Since we assume instantaneous mixing

Animation 2: Observed (black line) and simulated (grey line) temperature with hyporheic exchange (see Chapter 5).

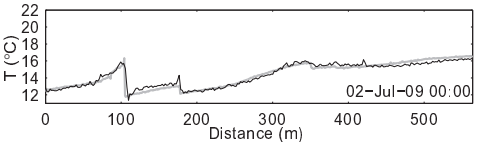

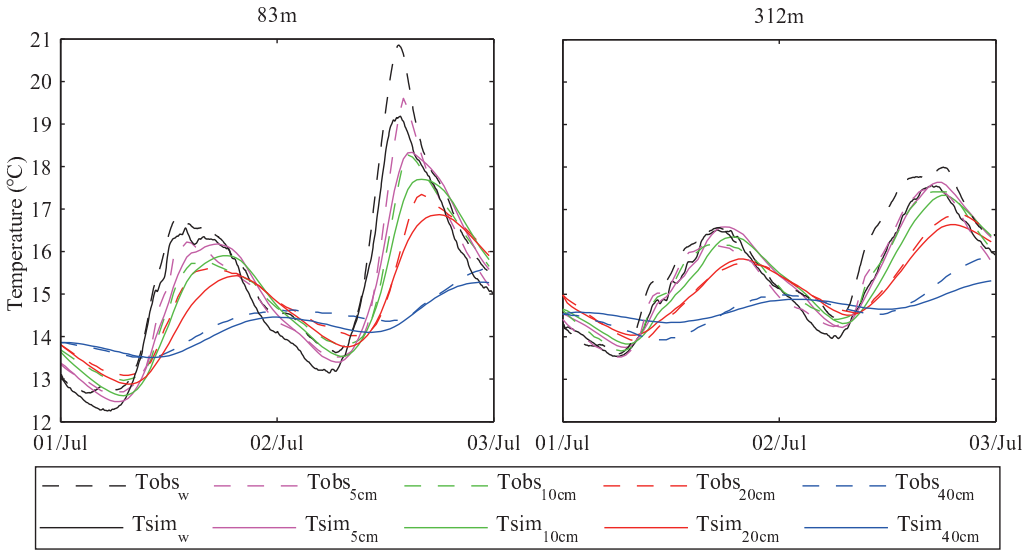

Figure 5.4: Observed and simulated subsurface temperatures. The simulated temperatures were calibrated on observed stream water temperatures only.

Table 5.1: Comparison of calibration parameters using two different strategies: 1) Calibration was done by mimicking the observed stream water temperatures (Tw), and 2) calibration was done by mimicking the observed subsurface temperatures at four different depths while the observed stream water temperature was used as boundary condition (T_{soil}).

	83 m		312 m	
	Calibration on T_w	Calibration on T_{soil}	Calibration on T_w	Calibration on T_{soil}
RMSE[a] ($°C$)	0.30	0.29	0.26	0.26
α (s^{-1})	$2.2e^{-3}$	$2.1e^{-3}$	$2.7e^{-3}$	$3.3e^{-3}$
A_{hz} (m^2)	$2.2e^{-3}$	$2.1e^{-3}$	$10.8e^{-3}$	$6.5e^{-3}$
Depth (m)	0.16	0.16	0.10	0.14
P (m)	0.08[b]	0.08	0.50[b]	0.54

[a] The RMSE was determined as the average RMSE between the simulated and observed subsurface temperatures at 5, 10, 20 and 40 cm depth for the whole simulation period.

[b] These values of the wetted perimeter are taken directly from the routing model.

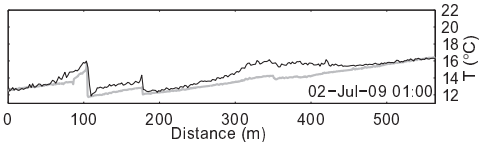

Animation 1: Observed (black line) and simulated (grey line) temperature without hyporheic exchange (see Chapter 5).

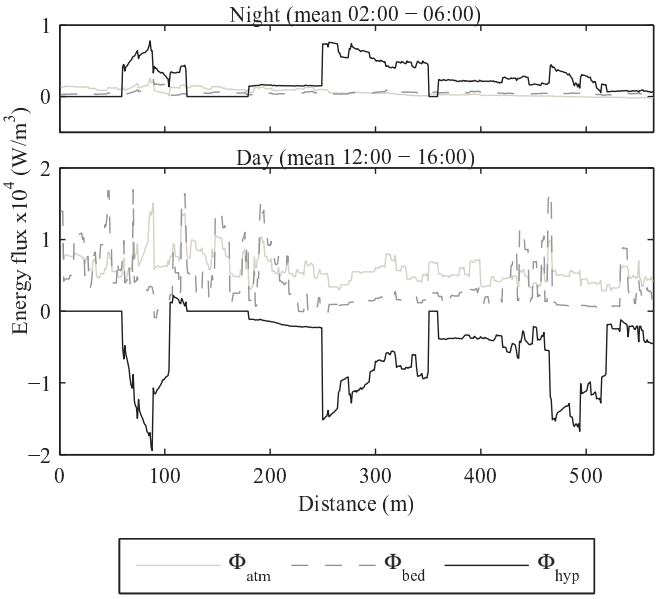

Figure 5.5: Mean simulated energy fluxes during night (02:00-06:00) and day (12:00-16:00). The energy fluxes have been averaged over 4 hours during 1 and 2-Jul-2009.

within each grid cell (both in the stream as in the subsurface), lateral hyporheic exchange cannot be tested within this model framework. However, some of the longer lateral hyporheic flow paths were taken into account implicitly. For example, salt that was injected in the stream around 60 m was found back in the inflow at 104 m (data not shown), indicating that this inflow (partly) consist of stream water infiltrated into the subsurface between 60 and 93 m. Because we observed the temperature of the inflow at 104 m, the temperature of this hyporheic return flux was known, and therefore it was not needed to simulate this temperature.

We also ignored the effect of vertical (upwelling) groundwater flow on subsurface temperature. In this catchment, groundwater flows through preferential flowpaths and enters the stream at concentrated inflow points. These inflows are then visible as temperature anomalies in the stream. During this study we only found six lateral inflows, meaning that only at these six locations this assumption is violated. With longitudinal grid cells of 1 m, this is only 1% of the whole stream.

In our model setup, we allowed the hyporheic zone to be somewhere in the subsurface (up to 1 m depth), without forcing it to be in the top layers. The rationale for this is that the rocky subsurface allows for many preferential flow paths, making it possible for stream water to be connected with a somewhat deeper hyporheic zone. However, after calibrating the model, most hyporheic zones seem to be directly beneath the stream. Only two sections (182-250 m and 360-420 m) appear to be really deeper in the subsurface. Yet, these are two sections where the

Animation 2: Observed (black line) and simulated (grey line) temperature with hyporheic exchange (see Chapter 5).

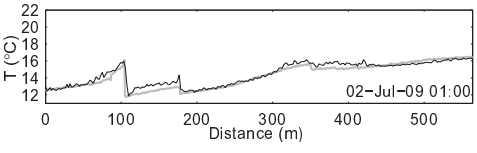

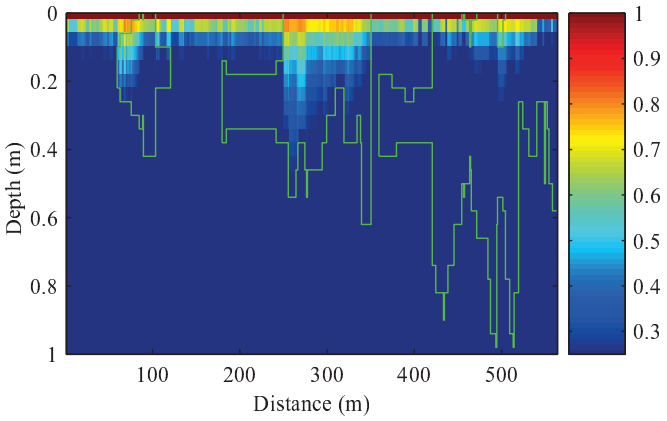

Figure 5.6: Diurnal temperature amplitudes in the subsurface divided by the amplitude at the top of each column. The green lines visualize the thickness and depth of the hyporheic zones.

parameters representing hyporheic exchange were poorly identified (see Section 5.4.2).

An assumption that has a much larger impact is that the width of the hyporheic zone is assumed to be the same as the wetted perimeter of the stream (which is responsible for the high variability of the thickness of the hyporheic zone, since the wetted perimeter is different for each grid cell). We recognize that this is an arbitrary way to determine the shape of the hyporheic zone, but since we do not have any observation, any shape would be arbitrary. At the two locations where we observed subsurface temperatures (at 83 and 312 m), we inferred the thickness of the hyporheic zone with two different sets of observations (i.e. calibrating on in-stream temperature, and calibrating on observed subsurface temperature, as described in section 5.2.2). Both methods gave similar results (Table 5.1), indicating that the assumed shape of the hyporheic zone is correct for these two locations. Yet, between 420 and 520 m, the calibrated thickness of the hyporheic zone seems rather large. Since a large volume was needed to buffer the temperature in the model, a wider and thinner hyporheic zone would have given similar model results while the shape of the hyporheic zone could have been more realistic.

Finally, we must consider the simulated depth of the subsurface. In our simulations we defined a constant temperature at 1 m depth below the stream. To test the validity of this assumption, we determined for each vertical section in the subsurface the diurnal temperature amplitude at 2-Jul-2009 and divided that by the amplitude at the top of each vertical subsurface column. For most areas, the temperature amplitude below a depth of 0.2 m was less than 25% of the amplitude at the top of the column. Only between 250 and 300 m this was slightly deeper at maximum 0.5 m depth (Fig. 5.6). This indicates that simulating subsurface temperatures up to a depth of 1 m was sufficient. We also found no change in RMSE when the subsurface temperatures where simulated up to 2 m depth (results not presented).

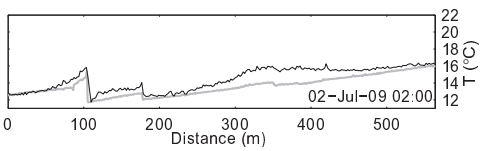

Animation 1: Observed (black line) and simulated (grey line) temperature without hyporheic exchange (see Chapter 5).

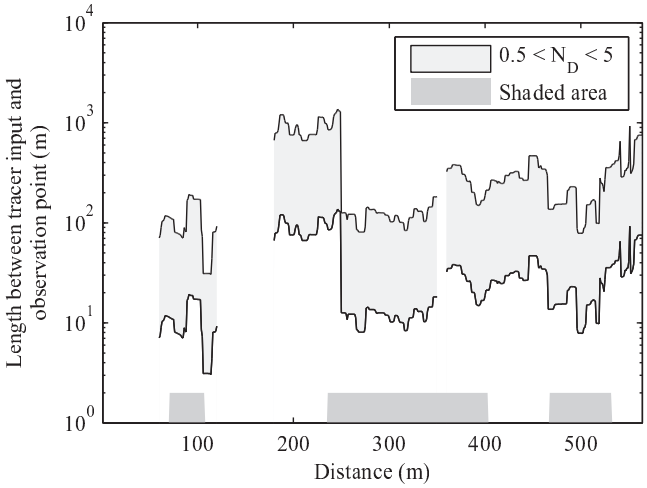

Figure 5.7: Length between tracer input and observation point, for a Damkohler number between 0.5 and 5. The shaded areas are parts which are shaded all day. The non-shaded areas are exposed to solar radiation for at least some period during the day.

5.4.2 How well is the hyporheic zone constrained?

Harvey and Wagner [2000] stated that for a good identifiability of α and A_{hz} the Damkohler number should be between 0.5 and 5. The Damkohler number is a dimensionless number describing the ratio between hyporheic exchange rate and advection and is given by $N_{DaI} = \alpha(1 + A_w/A_{hz})L/u$ [Harvey and Wagner, 2000], where L is the distance between tracer input and observation point and u is stream velocity. Since the Damkohler number is a function of α and A_{hz}, which are both calibration parameters, it is only possible to determine the Damkohler number a posteriori.

In this study the main tracer input is solar radiation. Close to an area exposed to solar radiation $N_{DaI} < 0.5$, while far away $N_{DaI} > 5$. This means that although we have temperature observation every 2 m along the stream, we cannot determine α and A_{hz} everywhere along the stream with the same confidence level. To investigate the indentifiability of α and A_{hz}, we determined the required distance L needed to obtain $0.5 < N_{DaI} < 5$ (Fig. 5.7). For example: between 182 and 250 m the stream is exposed to solar radiation. This means that in this reach L is very small since the tracer injection point (solar radiation) is at the same place as the temperature observations. An N_{DaI} of 0.5 indicates that a length of ∼150 m is needed for a good identifiability of α and A_{hz} (Fig. 5.7). We therefore conclude that the identified hyporheic exchange at this (non-shaded) stream reach is unreliable. On the other hand, between 250 and 350 m the stream is not exposed to solar radiation. The mentioned range of $0.5 < N_{DaI} < 5$ indicates that good identifiability is obtained when the distance L between the tracer input and point of observation

Animation 2: Observed (black line) and simulated (grey line) temperature with hyporheic exchange (see Chapter 5).

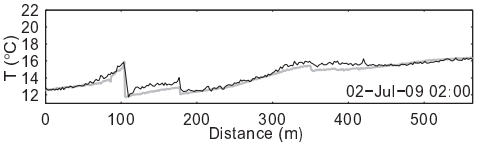

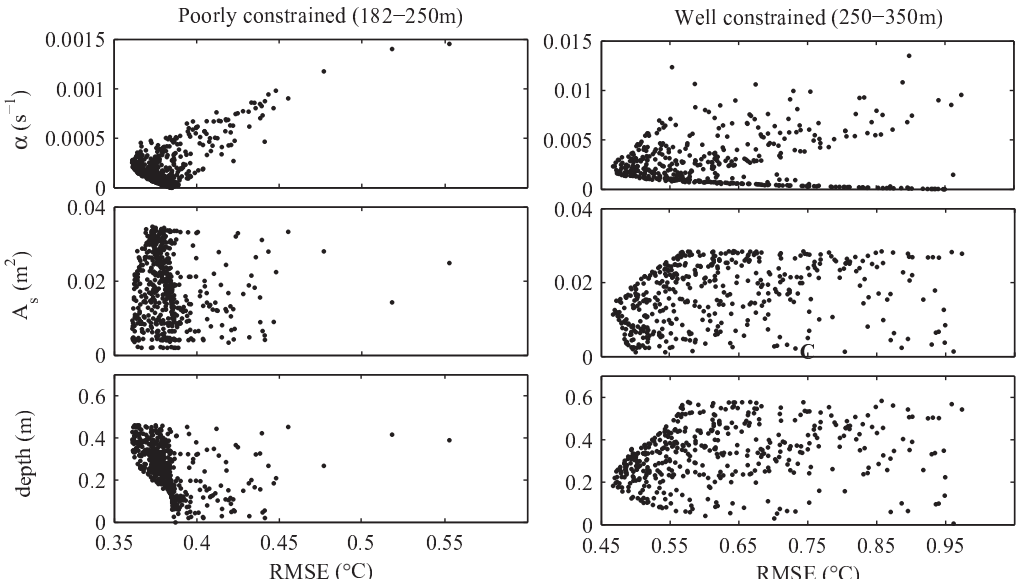

Figure 5.8: Scatter plots for three different parameters describing the hyporheic exchange for a poorly constrained section (left) and a well constrained section (right). 694 (segment 182-250 m) and 454 (segment 250-350 m) Monte Carlo simulations were used, during which the values of α, A_{hz} and average depth of the hyporheic zone varied randomly around their optimal value.

is between ∼12 and ∼120 m from the tracer input, which is the case for this stream reach. This identifiability is also seen in the scatter plots for both stream sections (Fig. 5.8). These plots were obtained from 694 (segment 182-250 m) and 454 (segment 250-350 m) Monte Carlo runs during which the values of α and A_{hz} and average depth of the hyporheic zone varied randomly around their optimal value. Good identifiability is obtained when the lowest RMSE converges to a unique value of the considered parameter. This was the case for the stream segment between 250 and 350 m, while for the segment 182-250 m, the parameter values did not converge to a unique value with a lower RMSE. This means that with this method, in a natural setup hyporheic exchange can only be identified in shaded areas downstream of an open area, which is exposed to direct solar radiation. During less favorable conditions, such as cloudy days or for completely shaded stream segments, a possible solution would be to heat up the stream water artificially, although we recognize that a large amount of energy will be needed to heat up the water a few degrees. Another reason for poor identifiability of the hyporheic exchange is when the temperature variations are too low. This is the case between 360 and 420 m. At this stream segment the standard deviation of the 2 day temperature time series is ∼0.9°C, while this is between 1.1 and 1.5°C between 250 and 350 m.

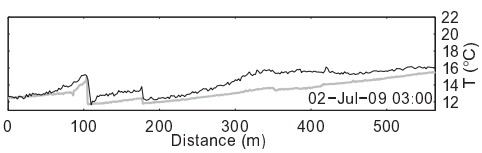

Animation 1: Observed (black line) and simulated (grey line) temperature without hyporheic exchange (see Chapter 5).

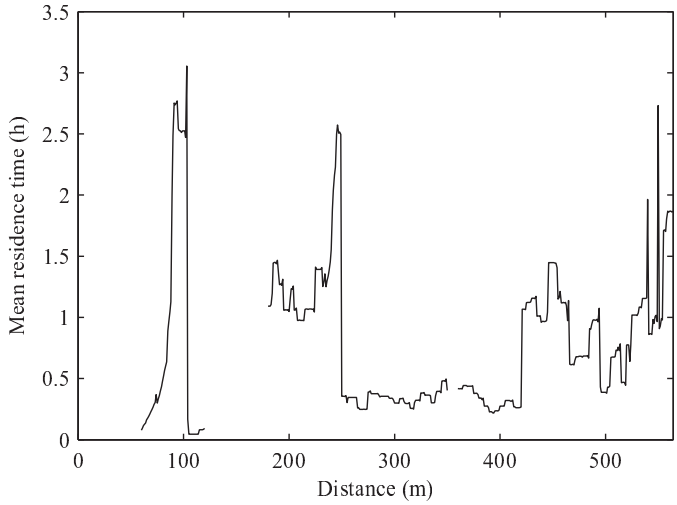

Figure 5.9: Spatial variation of mean residence times in the hyporheic zone, determined with $A_{hz}/(\alpha A_w)$.

Our results show that at places where hyporheic exchange is identifiable the hyporheic flow is 4% of the stream flow per unit stream length (determined as $\alpha A_{hz}/Q$), which is an order of magnitude higher than found by Gooseff et al. [2003] and Wondzell [2006] in similar sized streams with a 'poorly sorted mix of boulders, cobbles, gravels and finer textured sediments' [Wondzell, 2006], while in a 4$^{\text{th}}$ order stream Gooseff et al. [2003] found values between 0.1 and 3%. Zarnetske et al. [2007] found for five low gradient tundra streams with 10 to 1000 times higher flows, hyporheic exchange fluxes between 0.1 and 3% of the stream flow per unit stream length.

In this model framework we used the assumption of a well mixed hyporheic zone. The mean residence time (MRT) of water in the hyporheic zone can then be easily determined with $A_{hz}/(\alpha A_w)$. However, we could not test whether the assumption of a well-mixed hyporheic zone is the best one, or if, for example a different residence time distribution (i.e., power-law, gamma), were more appropriate. Although we cannot be certain about the best residence time distribution, the assumption of a well mixed hyporheic zone gives a first estimate of the MRT, which is variable along the stream reach (Fig. 5.9), from more than 2.5 h between 90 and 104 m to less than 0.5 h between 250 and 420 m. The MRTs downstream of 420 m are relatively large, although a large exchange coefficient was found here. As stated in Section 5.4.1, a large hyporheic zone volume was needed in the simulations to buffer enough energy to decrease the diurnal in-stream temperature oscillations. Besides having a different shape of the hyporheic zone, it is also possible that the assumption of a well-mixed hyporheic zone is not valid here, and that in reality, lateral hyporheic flow paths are present at this area.

Animation 2: Observed (black line) and simulated (grey line) temperature with hyporheic exchange (see Chapter 5).

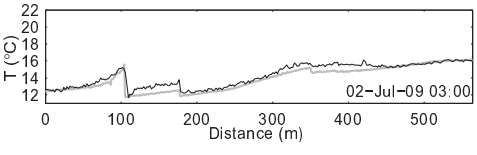

5.5 Summary and conclusions

Hyporheic exchange is a process that moves stream water into the subsurface and back to the stream. However, it is often difficult to determine the flux and the volume and location of the hyporheic zone. A widely used method to estimate the hyporheic flux and volume is by analyzing observed in-stream tracer breakthrough curves. However, in that approach the observation points must be determined a priori, while no knowledge is obtained on the specific location or variance of the size of the hyporheic zone between observation locations.

In this work, we present a novel approach to estimate the parameters that describe the hyporheic exchange. We use high spatial and temporal resolution in-stream temperature observations to inform our model of heat transport in the stream and exchange with the hyporheic zone. Because of the high spatial resolution (2 m) of the observations, we were able to choose the stream segments of constant hyporheic exchange parameters after the experiment (instead of a priori), which gave us more spatial flexibility.

To interpret the high-resolution temperature observations, a coupled energy balance model with an advection-dispersion model is needed. An advantage of this coupled model is that energy exchange (conductive and advective) between the stream and the subsurface can be modeled and compared to the observed. Because the hyporheic zone is located somewhere in the subsurface, the depth of the hyporheic zone below the stream influences the temperature of this zone and thus of the hyporheic return flux. This makes it possible to estimate the depth of the hyporheic zone over small spatial scales (<10m), which is another important feature of this work.

However, the method also has some limitations. Temperature variations of several degrees are needed to identify the hyporheic exchange parameters. As a result, this method can only be applied in streams where the diurnal temperature fluctuations are sufficiently large. The low flow situation and relative warm meteorological conditions during this study were therefore suitable for testing this method.

The second limitation, which accounts for all in-stream tracer studies, is that a certain distance is needed between the point of tracer input and the observation point. In most cases, solar radiation is the main heat (i.e., tracer) input. This means that it is only possible to identify hyporheic exchange in shaded areas downstream of areas subject to solar radiation. A possible solution to overcome this problem is artificial heating (or cooling) of stream water or artificial shading of streams that are fully exposed to solar radiation.

This study contributes to the long-term objective of using heat as a tracer to quantify runoff mechanisms during stormflow and baseflow conditions. This work enabled us to more fully quantify the processes that influence the temperature distribution along the stream during steady discharge conditions. The following Chapter will concentrate on the dynamic changes of discharge and temperature during stormflow.

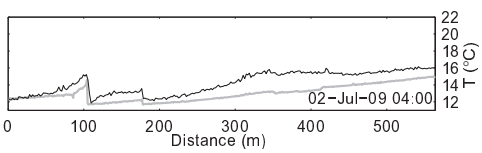

Animation 1: Observed (black line) and simulated (grey line) temperature without hyporheic exchange (see Chapter 5).

Chapter 6

Quantifying spatial and temporal discharge dynamics of an event in a first order stream, using Distributed Temperature Sensing†

Abstract. *Understanding the spatial distribution of discharge can be important for water quality and quantity modeling. Non-steady flood waves can, particularly as a result of short high intensity summer rainstorms, influence small headwater streams significantly. The aim of this paper is to quantify the spatial and temporal dynamics of stream flow in a headwater stream during a summer rainstorm. These dynamics include gains and losses of stream water, the effect of bypasses that become active and hyporheic exchange fluxes that may vary over time as a function of discharge. We use an advection-dispersion model coupled with an energy balance model to simulate in-stream water temperature, which we compare with high resolution temperature observations obtained with Distributed Temperature Sensing. This model was used as a learning tool to stepwise unravel the complex puzzle of in-stream processes subject to varying discharge. Hypotheses were tested and rejected, which led to more insight in the spatial and temporal dynamics in discharge and hyporheic exchange processes. We showed that, for the studied stream infiltration losses increase during a small rain event, while gains of water remained constant over time. We conclude that, eventually, part of the stream water bypassed the main channel during peak discharge. It also seems that hyporheic exchange varies with varying discharge in the first 250 m of the stream; while further downstream it remains constant. Because we relied on solar radiation as the main energy input, we were only able to apply this method during a small summer storm and low flow conditions. However, when additional (artificial) energy is available, the presented method is also applicable in larger streams, during higher flow conditions or longer storms.*

†. *Based on: Westhoff, M. C., Bogaard, T. A., Savenije, H. H. G., 2011. Quantifying spatial and temporal discharge dynamics of an event in a first order stream, using distributed temperature sensing. Hydrol. Earth Syst. Sci. 15 (6), 1945–1957,* `http://www.hydrol-earth-syst-sci.net/15/1945`

Animation 2: Observed (black line) and simulated (grey line) temperature with hyporheic exchange (see Chapter 5).

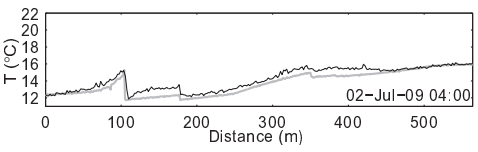

6.1 Introduction

Understanding discharge generation processes in headwater catchments is crucial for water quality and quantity modeling [Bonell, 1998]. However, it is often difficult to differentiate between different runoff generation processes. A classical way to do this is by hydrograph separation using end-member mixing analysis approach [Sklash and Farvolden, 1979]. This technique can be useful in differentiating between different source areas or between event and pre-event water [Uhlenbrook and Hoeg, 2003]. However, the spatial resolution is often low, fluxes are lumped and uncertainties can be high.

Understanding the spatial distribution of discharge can be important since non-steady flood waves can influence small headwater streams significantly, particularly as a result of short high intensity summer rainstorms. During such events, discharge can more than double, and side channels can become active. Also subsurface stormflow may occur, although a certain storage threshold in the hillslope has to be passed before this mechanism becomes active [e.g. Tromp-van Meerveld and McDonnell, 2006a].

To observe the spatial and temporal distribution of lateral inflows, several researchers excavated trenches [Woods and Rowe, 1996; Weiler et al., 1998; Uchida et al., 2005; Retter et al., 2006; Gomi et al., 2008; Tromp-van Meerveld et al., 2008]. Although these were able to give spatial and temporal flow information, installation of trenches is destructive and limited in size (2–60 m).

Another approach was presented by Ragan [1968]. He monitored all incoming water fluxes in a 190 m long stretch, including the change of in-stream storage. He added one term to close the water balance, which he concluded to be subsurface stormflow. Although he is one among some others [e.g. Anderson and Burt, 1978; Hjelmfelt Jr. and Burwell, 1984] who gained insights in temporal and spatial dynamics of lateral inflow without the use of trenches or 3D groundwater-surface water models , he did not include infiltration losses of stream water or hyporheic exchange in his analysis while also the location of the calibrated subsurface stormflow was unknown.

Stream water losses (or downwelling fluxes) are difficult to quantify, since they do not influence stream water quality directly. To determine these fluxes, some researchers observed vertical subsurface temperature profiles, which, when coupled with a vertical advection-dispersion model gave flow rates and directions [Stallman, 1965; Lapham, 1989; Taniguchi and Sharma, 1990; Silliman et al., 1995; Constantz and Thomas, 1996; Constantz, 1998; Constantz et al., 2003; Becker et al., 2004; Niswonger et al., 2005; Blasch et al., 2007]. However, these profiles were point measurements along the stream and obtained during steady state discharge conditions.

Moreover, hyporheic exchange fluxes may change with varying discharge. This triggered research on seasonal changes in hyporheic exchange, determined from head differences in a vertical profile using piezometer nests [Harvey and Bencala, 1993; Wroblicky et al., 1998; Bartolino, 2003]. In addition, on the timescale of one flood wave, coupled 3D groundwater-surface water models were

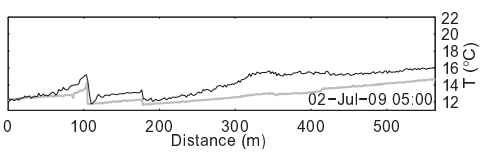

Animation 1: Observed (black line) and simulated (grey line) temperature without hyporheic exchange (see Chapter 5).

developed [Lal, 2001; Habel and Bagtzoglou, 2005; Boano et al., 2007; Ha et al., 2008]. However, these deterministic models require an accurate description of hydraulic conductivities and bedforms while such data are often not available. To overcome this problem, hyporheic exchange has been quantified using in-stream tracer tests. Most studies linking hyporheic exchange with discharge did their tracer tests during different discharge regimes [Legrand-Marcq and Laudelout, 1985; Harvey et al., 1996; Morrice et al., 1997; Wörman and Wachniew, 2007; Zarnetske et al., 2007; Schmid, 2008; Schmid et al., 2010], different morphological states [Hart et al., 1999; Harvey et al., 2003] or between different streams [D'angelo et al., 1993; Morrice et al., 1997; Schmid et al., 2010], but always during steady state flow conditions and not during a complete rainstorm.

The aim of this paper is to quantify the spatial and temporal dynamics of stream flow in a headwater catchment during a summer rainstorm. These dynamics include gains and losses of stream water, the effect of bypasses (in our case a side channel of ca 20 m long) that become active and hyporheic exchange fluxes that may vary over time as a function of discharge. In a previous study we showed the relation between hydraulics, in-stream temperature and hyporheic exchange in a first order stream during steady state discharge conditions [Westhoff et al., 2011 (*accepted*]. In this paper we focus on the dynamic effects that occur during and after a small intensive summer rainstorm of 6.4 mm, with a maximum intensity of 4.8 mm in 10 min. We use an advection-dispersion model coupled with an energy balance model to simulate in-stream water temperature, which we compare with high resolution temperature observations obtained with Distributed Temperature Sensing (DTS). Together with upstream and downstream discharge observations, we were able to locate and estimate the dynamics of hyporheic exchange, lateral inflows and bypasses. We used the method as a learning tool in which we stepwise unravel the complex interactions and dynamics in discharge.

6.2 Methods

6.2.1 Model description

In this Chapter we use the same model as in Chapter (5), except that we add rainfall as an additional source. Equation (3.1) and (4.6) are now written as:

$$\frac{\partial A_w}{\partial t} + \frac{\partial Q}{\partial x} = q_L + RW_R \tag{6.1}$$

$$\begin{aligned} \rho_b c_b \frac{\partial A_b T_w}{\partial t} + \rho_w c_w \frac{\partial Q T_w}{\partial x} + \rho_w c_w \frac{\partial}{\partial x}\left(-A_w D \frac{\partial T_w}{\partial x}\right) \\ = \rho_w c_w (q_L T_L + R W_R T_R) + \rho_w c_w \alpha A_w (T_{hz} - T_w) + W_b \Phi_{atm} + P_b \Phi_{cond} \end{aligned} \tag{6.2}$$

where R is rainfall (m/s), W_R is the width where rainfall turns into runoff immediately (m) and T_R is the temperature of the rain (°C). In this Chapter, we use the model as a learning tool

Animation 2: Observed (black line) and simulated (grey line) temperature with hyporheic exchange (see Chapter 5).

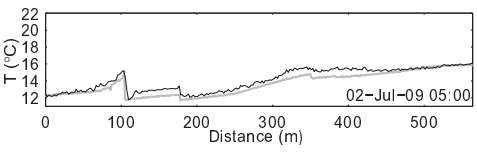

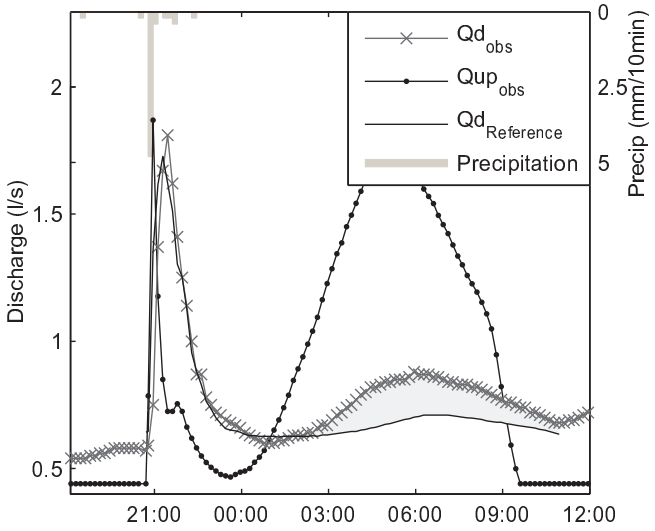

Figure 6.1: Observed and simulated (Reference) discharge of second peak on 22 and 23 June 2008. The reference discharge is simulated discharge using parameters obtained from calibration of the first discharge peak. The subscripts d and up refer to downstream and upstream. The shaded area is the difference between observed and simulated discharge.

to identify the spatial and temporal dynamics during a summer rainstorm. The studied period is 22 and 23-Jun-2008, during which a short but intensive rain event caused a double peak in discharge (Fig. 6.1), which is typical for this stream during low flows. During such conditions, the first discharge peak is mainly caused by 'rain on water' and rain on saturated riparian land (saturation overland flow), while the second discharge peak is assumed to be subsurface stormflow. Prior to the rain event, the discharge was 0.44 and 0.65 l s^{-1} for the upstream and downstream V-notch weir, respectively, while peak discharge was 1.9 and 1.8 l s^{-1}. All hyporheic exchange parameters were taken the same as in Chapter (5). For this study, we first validated the model for a two day period prior to the rainfall event at 22-Jun-2008 20:40, during which the discharge was steady.

6.2.2 Stepwise improvement of dynamic discharge simulations

In this study, we follow a downward approach in which we stepwise improve the model [Klemeš, 1983; Jothityangkoon et al., 2001; Sivapalan et al., 2003]. This means that we first model a simple case, and based on the results, we stepwise increase model complexity and develop and test new hypotheses to improve the model results. We combine this with a multi-objective model evaluation [Fenicia et al., 2008]. The objective functions are (1) the Root Mean Square Error of the downstream discharge ($RMSE_Q$), (2) the Root Mean Square Error of the in-stream

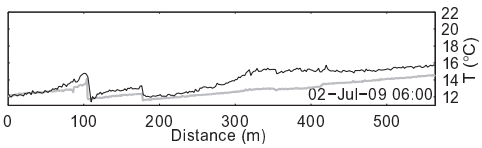

Animation 1: Observed (black line) and simulated (grey line) temperature without hyporheic exchange (see Chapter 5).

temperature ($RMSE_T$) and (3) the Root Mean Square Error of the relative contribution of the second lateral inflow at 178 m ($RMSE_L$).

For calibration, we split the observed hydrograph in two parts because different processes are responsible for the discharge peaks: the first peak is mainly caused by rain on water, while the second peak is assumed to be caused by subsurface stormflow. By first calibrating on the first discharge peak, we could test that parameter set on the second discharge peak, which allowed us to formulate different hypotheses to improve our understanding of the discharge dynamics (section 6.2.2.2).

6.2.2.1 First discharge peak

In a first step we only focus on the first discharge peak (between 22-Jun-2008 20:40 and 23-Jun-2008 01:00). Here we calibrated three parameters. These parameters are: 1) the losses of water which we describe as a function of discharge, 2) the area where saturation overland flow takes place (W_R): this is the stream itself and its near surroundings and 3) the temperature of the rain water (T_R). The first two influences both downstream discharge and in-stream temperature, while the third parameter only influences in-stream temperature.

6.2.2.2 Second discharge peak

During the second step of the calibration we focus on different processes that occur during the second discharge peak, which we assume is subsurface stormflow originating from the area upstream of the upstream V-notch weir. We first extend the simulation period of the first step with nine hour until 23-Jun-2008 10:00 to cover the second discharge peak, without changing any parameter. In this run we found a couple of mismatches between observed and simulated discharge and temperature. For reasons of clarity we treat these temperature and discharge mismatches separately, although we recognize that discharge influences temperature as well.

In-stream temperature

To improve the simulated temperature, we investigated the effect of constant and variable hyporheic exchange parameters (i.e. the flux between the stream and hyporheic zone, and volume of the hyporheic zone). This resulted in four different alternatives:

1. $q_{hyp} = \alpha A_w$ and $A_{hz} = P_b d_{hz}$, where d_{hz} is the thickness of the hyporheic zone, and is assumed to be constant in time. For the exchange flux we used the widely used expression from Runkel [1998]. For the volume of the hyporheic zone we assumed that the thickness would remain the same, and A_{hz} depends linearly on the wetted perimeter of the stream.
2. Both the q_{hyp} and A_{hz} are constant over time and keep the pre-event values.
3. $q_{hyp} = \alpha A_w$ and A_{hz} is constant over time.
4. q_{hyp} is constant over time and $A_{hz} = P_b d_{hz}$.

Animation 2: Observed (black line) and simulated (grey line) temperature with hyporheic exchange (see Chapter 5).

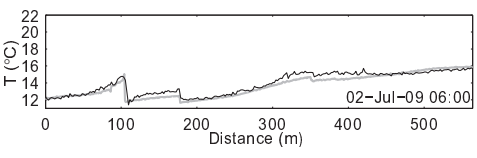

Discharge

The calibrated run of the first discharge peak was used for the second peak. This simulation resulted in a difference between simulated and observed downstream discharge for the second peak. In this step we took the difference between observed and simulated downstream discharge, and added this as a lateral inflow at distance x_i. By changing the position of this new lateral inflow, we tested three different hypotheses on where this water came from.

1. As a diffuse source between 250 and 350 m. The reason for this is that when this new water is cooler than the stream water (as a first estimate we took the temperature of the third lateral inflow for the temperature of this new inflow), it would cool down the stream water, which would result in a better fit.
2. As extra water from the second lateral inflow point at 178 m. Reason for this is that when the stream discharge is higher, the water would not heat up as rapidly. The reason for adding this new water at an already existing source is that preferential flowpaths already direct water to this point. Extra subsurface stormflow would easily directed to the same place.
3. As a new source at 117 m. This source is actually a bypass or side channel, bypassing the stream between ∼80 and 117 m. It has a similar bedform as the stream, and is completely shaded by vegetation. During high (winter) flows, we have observed that part of the stream water flowed through this bypass. Here we test if this also happens during this summer rainstorm.

6.3 Results

Validation of the model as being calibrated in Chapter (5) was done for the period 21 June 2008 00:00 until 22 June 2008 20:40, which was just before the start of the storm event. During this validation, the four major lateral inflows (at 104, 178, 350 and 414 m from the upstream V-notch weir, respectively) were determined to be 0.32 ± 0.013, 0.27 ± 0.016, 0.11 ± 0.008 and 0.16 ± 0.064 l s^{-1}, the two smaller inflows at 383 and 393 m were estimated to be 0 and 0.01 l s^{-1}, and the two losses between 60 and 77 m and between 233 and 247 m were determined to be 0.41 and 0.27 l s^{-1} to match the observed downstream discharge (Fig. 6.3a: blue line in bottom panel).

The validation run had a RMSE$_T$ of 0.51°C (for comparison: the RMSE$_T$ of the calibrated model was 0.66°C for the same time span at 1 and 2-Jul-2009. Note that this is slightly different than reported in Chapter (5), since the simulation period is 3:20 hour shorter). The difference in the RMSE$_T$ was mainly caused by the fact that during the calibration period the fibre optic cable was not submerged at a few distinct places. During the validation the simulated temperature downstream of 420 m was about 1°C too high during the night.

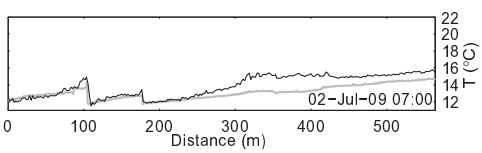

Animation 1: Observed (black line) and simulated (grey line) temperature without hyporheic exchange (see Chapter 5).

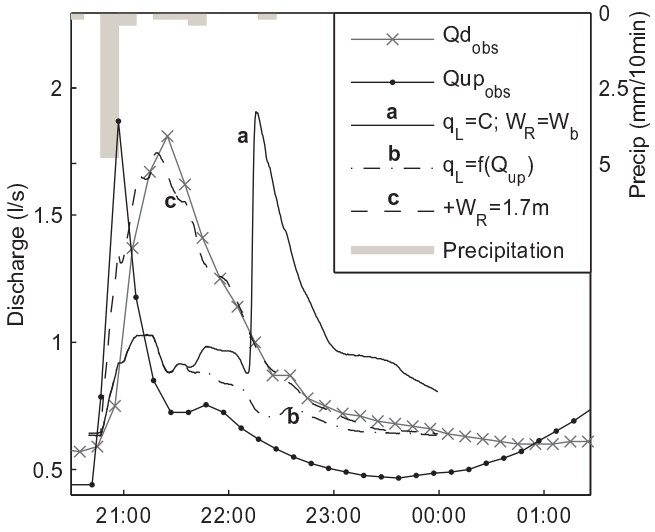

Figure 6.2: Observed and simulated first discharge peak on 22-Jun-2008. The subscripts d and up refer to downstream and upstream.

6.3.1 First discharge peak

The first discharge peak was calibrated by varying the infiltration losses ($q_L < 0$), the width accounting for 'rain on water' (W_R) and the temperature of the rain (T_R). Keeping the losses constant over time and W_R the same as the stream width W_b, resulted in a simulated downstream peak discharge arriving 50 min too late (line a in Fig. 6.2). Therefore we made the losses dependent on discharge (line b in Fig. 6.2): between 233 and 247 m the loss was set to be 45% of the discharge at 232 m. Between 60 and 80 m, the loss was set to 95% during pre-event discharge (0.4 l s^{-1}) and 88% during peak discharge (1.9 l s^{-1}). To be able to simulate the observed downstream discharge peak properly, we had to change W_R to 1.7 m for the entire stream to account for the additional saturated overland flow. After this refinement we obtained a $RMSE_Q$ of 0.11 l s^{-1} (line c in Fig. 6.2,Table 6.1). Good temperature simulations were obtained when T_R was taken 2.4°C lower than T_{air}, which can be seen as a correction for the wet bulb temperature. This resulted in a $RMSE_T$ of 0.34°C (Fig. 6.3A). For an overview of all steps in the calibration process and the corresponding objection functions, see Table 6.1.

6.3.2 Second discharge peak

Extending the simulation period until the second discharge peak, while keeping the same parameters as during the first discharge peak, resulted in a too low downstream discharge between 3:00 and 10:00h (Fig. 6.1). During the same period, the temperature between 250 and 350 m and downstream of 420 m was also too high (Fig. 6.3B). Here, we treat both discrepancies separately.

Animation 2: Observed (black line) and simulated (grey line) temperature with hyporheic exchange (see Chapter 5).

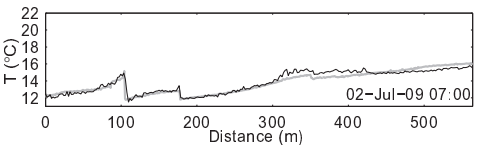

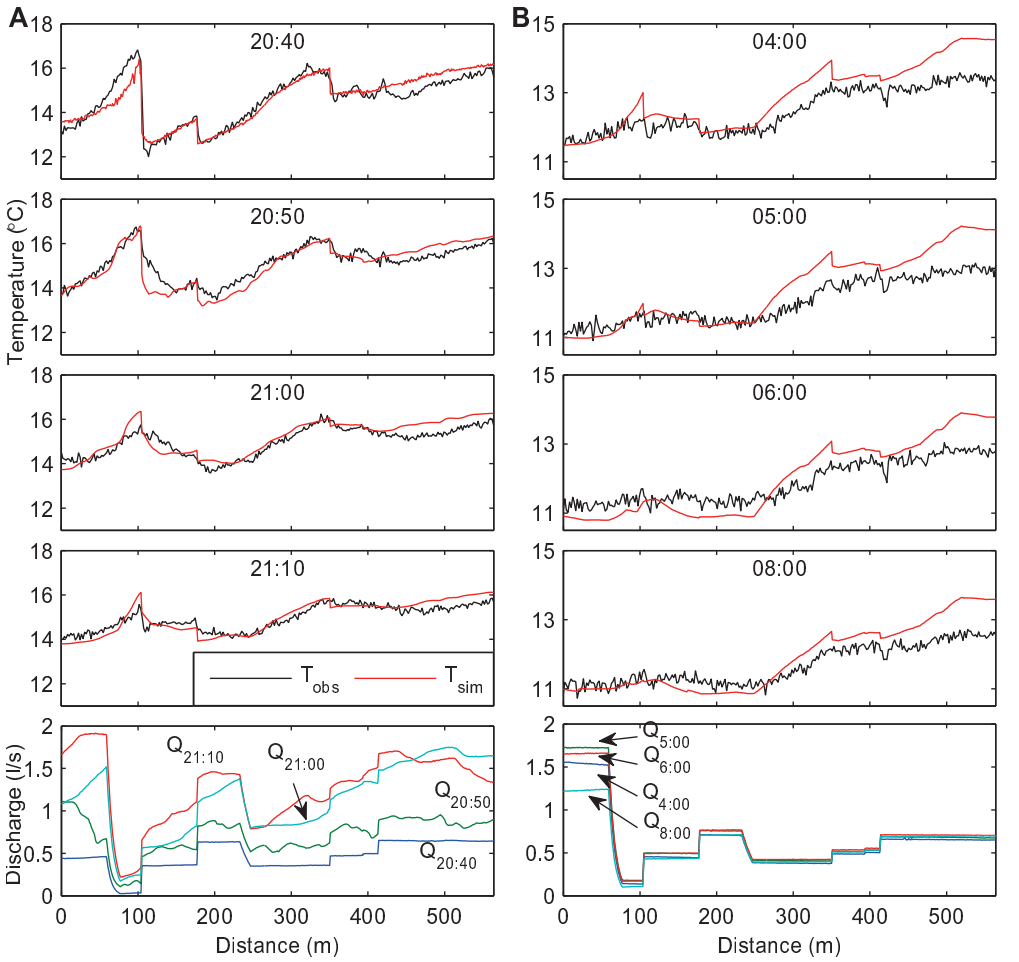

Figure 6.3: Observed and simulated temperature and simulated discharge during (A) first discharge peak (after calibration) and (B) second discharge peak using the same parameters as during the first discharge peak. q_{hyp} and A_{hz} are variable over time.

In-stream temperature

Although we recognize that discharge influences in-stream temperature as well, we focus first on the influence of different hyporheic exchange scenarios. The four different scenarios tested ($q_{hyp} = \alpha A_w$ and $A_{hz} = P_b d_{hz}$; q_{hyp} and A_{hz} are constant over time; $q_{hyp} = \alpha A_w$ and A_{hz} is constant over time; and q_{hyp} is constant over time and $A_{hz} = P_b d_{hz}$), gave different results for different sections in the stream. In Fig. (6.4A) the RMSE_T is shown for the time series between 1:00 and 10:00h for each observation point (a moving average over three points was plotted to get slightly smoother lines). Until 250 m the temperature was best simulated when both

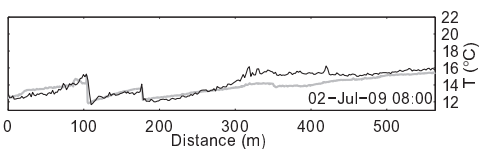

Animation 1: Observed (black line) and simulated (grey line) temperature without hyporheic exchange (see Chapter 5).

the hyporheic flux and the volume of the hyporheic zone were taken variable over time, while downstream of 250 m best results were obtained when both were constant over time. From Fig. (6.4A), it is also seen that when only A_{hz} is variable while q_{hyp} is constant, results hardly differ from the case where both are constant over time. The difference between a constant and variable A_{hz} is slightly larger when q_{hyp} is variable.

Discharge

During the second peak, the simulated downstream discharge is too low between 3:00 and 10:00h: apparently there is some lateral inflow, which we did not encounter for (Fig. 6.1). The difference between the two hydrographs (shaded area in Fig. 6.1) has been added to the stream at different locations x_i, while we used the RMSE_T and RMSE_L to test the effect of the different locations (the RMSE_Q are equal for each scenario, because the same amount of water was added for each

Table 6.1: Overview of calibration parameters for each step, with corresponding RMSE values.

First discharge peak (simulations between 20:40 and 00:00h)						
	$q_L < 0$	W_R	T_R	RMSE_T [° C]	RMSE_L [%]	RMSE_Q [l s^{-1}]
1	constant	W_b	T_{air}	0.38	8.6	0.45
2	$f(Q_{up})$	W_b	T_{air}	0.38	10.7	0.35
3	$f(Q_{up})$	1.7 m	T_{air}	0.38	6.8	0.11
4	$f(Q_{up})$	1.7 m	$T_{air} - 2.4°$ C	0.34	6.8	0.11
Second discharge peak (simulations between 01:00 and 10:00h)						
Calibration on in-stream temperature						
		q_{hyp}	A_{hz}	RMSE_T [° C]	RMSE_L [%]	RMSE_Q [l s^{-1}]
1		αA_w	$P_b z_{hz}$	0.50	5.8	0.12
2		constant	constant	0.48	5.8	0.12
3		αA_w	constant	0.49	5.8	0.12
4		constant	$P_b z_{hz}$	0.49	5.8	0.12
Calibration on discharge						
				RMSE_T [° C]	RMSE_L [%]	RMSE_Q [l s^{-1}]
Reference[a]				0.46	5.8	0.12
Scenario 1: inflow added between 250-350 m				0.40	5.8	0.01
Scenario 2: inflow added at 178 m				0.41	18.2	0.01
Scenario 3: inflow added at 117 m				0.41	4.3	0.01

[a] Reference refers to the simulation where q_{hyp} and A_{hz} are variable between 0 and 250 m and constant between 250 and 564 m, but without the new source.

Animation 2: Observed (black line) and simulated (grey line) temperature with hyporheic exchange (see Chapter 5).

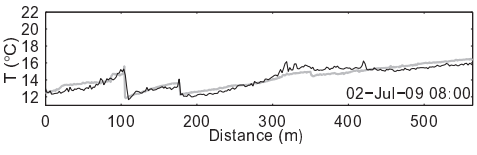

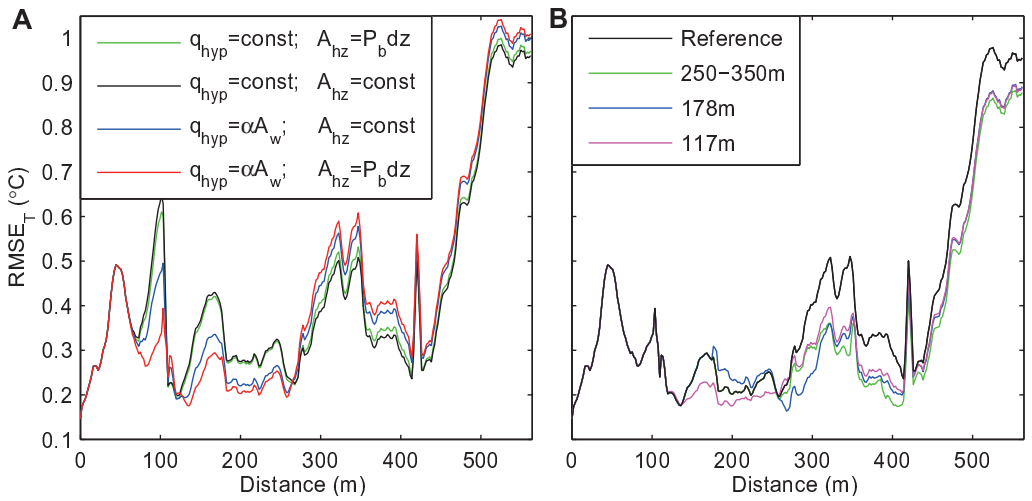

Figure 6.4: $RMSE_T$ for (A) different hyporheic exchange scenarios, and (B) different locations of the new source. Reference refers to the simulation where q_{hyp} and A_{hz} are variable between 0 and 250 m and constant between 250 and 564 m, but without the new source. The numbers of the other solutions are the location of the new source. A moving average of three observation point in space was taken for all time series between 23-Jun-2008 1:00 and 10:00h.

scenario). As a reference case, we used a hyporheic exchange scenario during which q_{hyp} and A_{hz} are variable between 0 and 250 m while downstream of 250 m they are constant over time. Because the temperature downstream of 420 m was also too high during the validation, we only focus on the area upstream of 420 m. Between 117 and 260 m, the $RMSE_T$ is the lowest when the new source is added at 117 m. Between 260 and 320 m best results were obtained when the new source was added at 178 m, while downstream of 320 m the diffuse source added between 250 and 350 m gave best results (Fig. 6.4B). Comparing the different scenarios with the observed relative contribution of the second source shows the best results when water is added at 117 m, with a $RMSE_L$ of 4.3% for the time series between 01:00 and 10:00h (Fig. 6.5, Table 6.1), with slightly poorer performance for the diffuse source ($RMSE_L$ is 5.8%). Note that the latter does not affect the second source compared to the reference simulation, since the new source was added downstream of this point. The scenario where the source was added as extra water at the second source totally mismatches the observations ($RMSE_L$ is 18.2%), indicating that this hypothesis should be rejected.

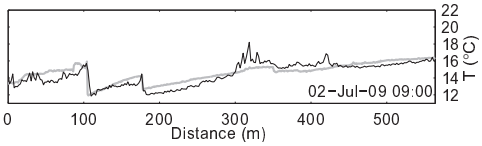

Animation 1: Observed (black line) and simulated (grey line) temperature without hyporheic exchange (see Chapter 5).

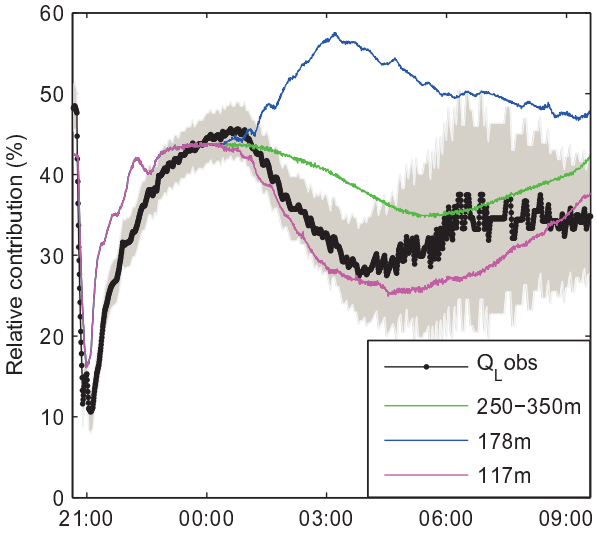

Figure 6.5: Observed and simulated (three scenarios) relative contribution of the second source. The different scenarios are the locations where the new source was added. Shaded area is observed contribution $\pm 1\sigma$

6.4 Discussion

6.4.1 Reality check

The presented method combines two sources of measured information: discharge observations and temperature observations. By combining these with a transport model for heat, we were able to investigate the spatial and temporal distribution of discharge along the whole length of the stream. In our approach we used the method as a learning tool to test, and more important, to reject hypotheses. In such a top-down approach, stepwise improvement of the model should be coupled with expert knowledge. Since a large number of different observations are needed to constrain the calibration parameters, all parameters and scenarios should be discussed for their physical meaning and realism [Seibert and McDonnell, 2002].

During the first discharge peak we calibrated three parameters: W_R, T_R and stream losses. In our case study W_R has limited physical meaning, since it corrects for errors in observed rainfall and discharge. The intensive rainstorm lasted for less than 10 min, while the logging interval of both, rainfall and discharge was also 10 min, which makes it likely that observed discharged is underestimated. Because the 'rain on water' and saturation overland flow is the main process causing the first discharge peak, a higher W_R could easily correct for these errors in the observations. Yet, the obtained value of 1.7 m seems realistic, since it is only slightly larger than the stream width itself.

Animation 2: Observed (black line) and simulated (grey line) temperature with hyporheic exchange (see Chapter 5).

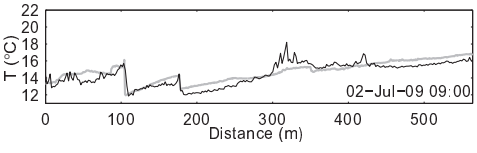

The temperature of the rain T_R is difficult to measure. As a first estimate air temperature was taken. However, the simulated in-stream temperature appeared to be too high during and just after the rainstorm, which was reason to decrease this temperature with 2.4°C. This corresponds with the wet bulb temperature obtained with a relative humidity of 80%, which is similar to the observed relative humidity in Ettelbruck (ca 6 km from the site).

We conclude that infiltration losses are relative to in-stream discharge, while gains of water are constant over time. We explain that with the fact that the whole catchment was relatively dry during the studied period and a 5 mm rainstorm is likely not enough to increase the groundwater level or to initiate runoff from the hillslopes. Infiltration losses, on the other hand, can be large under these conditions and can vary with discharge. When the width of the stream increases, the water can infiltrate in the initially dry part of the streambed.

Fig. 6.2, line *a* shows that when the infiltration loss between 60 and 77 m is taken constant over time, the peak in downstream discharge occurs 50 min too late. This indicates that the observed downstream discharge is not the same peak as the observed upstream peak, but that it originates from different water. This means that 1) the upstream discharge peak should disappear in-between the upstream and downstream V-notch weirs and 2) another source of water is responsible for the observed downstream discharge peak.

The second point can be easily explained by an increased amount of "rain on water": when increasing the stream width on which rain turns immediately into runoff to 1.7 m the observed downstream peak discharge was simulated correctly. To verify the first point, a location (or locations) has to be identified where the excess water infiltrates. The already existing infiltration loss between 60 and 77 m is a very likely place. Also because the simulated temperature anomaly caused by the lateral inflow at 104 m will be a factor 2 too small if the discharge peak is not reduced upstream of this point. This gives us confidence that the infiltration loss between 60 and 77 m is not constant but a function of stream discharge during these dry antecedent conditions.

The variability of the infiltration loss between 233 and 247 m is less clear. Assuming a constant loss here, would result in a downstream discharge peak lasting 15–20 min longer than observed, thus making the peak wider. Since the distinction between observed and simulated downstream discharge is less pronounced in case of a constant loss, we could not conclude with the same certainty that the excess water should have been infiltrated between 233 and 247 m. Nevertheless, a variable loss of 45% of upstream discharge gave the best results.

The different hyporheic exchange scenarios were tested during the second discharge peak because during the first discharge peak, the different scenarios did not lead to significantly different temperatures. This could be because the discharge peak was not long enough to influence the temperature in the hyporheic zone. The different scenarios during the second peak indicate that between 0 and 250 m q_{hyp} and A_{hz} are variable with varying discharge, while downstream of 250 m they remain constant with varying discharge (Fig. 6.4A). A possible explanation for this

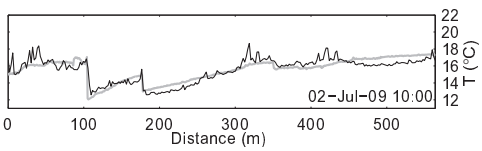

Animation 1: Observed (black line) and simulated (grey line) temperature without hyporheic exchange (see Chapter 5).

spatial variability is that between 0 and 250 m, the width of the stream increases a lot during peak discharge: about 1.7 times during the second discharge peak and between 75 and 90 m the width increases to 6 to 10 times the original width, compared to a factor 1 to 1.3 for the area downstream of 250 m. This results in a much higher contact area between the stream and hyporheic zone. Beside the increase in stream width, more upwelling groundwater could influence the hyporheic exchange as well [Harvey and Bencala, 1993; Harvey et al., 1996]. However, as stated before, the catchment was dry, so in our case an increase in upwelling groundwater is not so likely.

The main objective of this study is to see where and when discharge was generated. Here we tested three hypotheses about the location of the missing water to close the water balance. The tested locations were chosen after the first results of the reference simulation of the second peak. In principle, each location could be tested, but with knowledge of the field site, only three locations where considered feasible. The location of the diffuse source (250-350 m) was chosen, since it directly influences the in-stream temperature at this location. However, because the catchment was relatively dry and the the rainstorm small, this hypothesis is not so likely. The hypothesis of an increase of the excisting source at 178 m seems realistic, since only some extra water is needed to increase the lateral inflow. However, our model results (especially expressed in RMSE_L and Fig. 6.5) gave reasons to reject this hypothesis.

In the third scenario, we hypothesize that a bypass becomes active during the second discharge peak. An active bypass has been observed during higher flows, and therefore it is likely that it happened during this event as well. It also means that a significant amount of water that we accounted for as infiltration loss between 60 and 77 m, filled the dry bypass, and only when the whole bypass was saturated, it connected to the stream again. The initial wetting up of the bypass would also explain the time lag between the first discharge peak and the activation of the bypass. Overall, the third scenario seems the most likely one.

6.4.2 Limitation of method

Because temperature is used as a natural tracer, sufficient temperature fluctuations, both in space and time, are needed to be able to distinguish between different fluxes. Unfortunately, we therefore could only apply this method during a warm low flow period as we use natural heating via solar input. During winter, we observed temperature fluctuations that were too small to apply this method. Even during larger summer rainstorms, the spatial and temporal temperature fluctuations were not large enough to differentiate between different runoff fluxes. We have to conclude that during high water conditions, when subsurface stormflow becomes active and hydrologically it becomes more interesting, the method cannot rely on solar energy input, but sufficient additional energy has to be added to the stream with, for example, a powerful heat exchanger or by adding ice (we recognize that these methods also have their practical limitations). Another way would be to test this method downstream of reservoirs. For

Animation 2: Observed (black line) and simulated (grey line) temperature with hyporheic exchange (see Chapter 5).

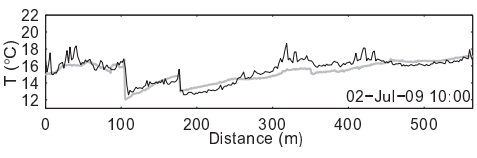

example: Toffolon et al. [2010] reported temperature increases of 3 to 4°C due to releases from a reservoir, with stream discharges in the order of 10 m^3s^{-1}.

Another interesting question was what would happen with the hyporheic exchange during non-steady state discharge conditions. The relation between hyporheic exchange and discharge or cross-sectional area is not known a priori. For reasons of simplicity, we only tested the linear relation between q_{hyp} and cross-sectional area as described by Runkel [1998], versus no relation at all, while A_{hz} was assumed to be linearly dependent with the wetted perimeter. Although these relationships are arbitrary, it gives a first estimate of how hyporheic exchange varies with discharge.

In our case study the spatial and temporal distribution of both hyporheic exchange and discharge had to be taken into account. In streams with limited hyporheic exchange, it is possible to focus only on the discharge distribution, making the method more reliable. The same is true when limited gains and losses are present in a stream. In such a case it may be possible to test more complex relations between hyporheic exchange and discharge.

6.5 Conclusions

In this paper we demonstrate a new method to identify spatial and temporal dynamics of in-stream discharge. We combined a routing model with an advection-dispersion model and an energy balance model, which we compared with both, discharge observations and high resolution temperature observations. This model was calibrated for steady state discharge by Westhoff et al. [2011 (*accepted*]. In the present study, it was used to unravel discharge dynamics during a small but intense summer rainstorm.

We used the model as a learning tool, where hypotheses were formulated, tested and rejected or accepted. We showed that during this rainstorm gains of water remained constant for the whole simulation period, while losses of stream water increase with increasing discharge. This resulted in large dampening of the observed upstream peak discharge. "Rain on water" and saturation overland flow in the riparian zone were likely the main processes responsible for the first discharge peak. For the second discharge peak, we conclude that most likely a bypass becomes active, which first had to be filled, before it was connected to the stream again.

Hyporheic exchange is likely to be variable with discharge in the upstream half of the stream, where the stream width increases significantly with increasing discharge, while in the downstream half temperature was better simulated if a constant hyporheic exchange was assumed.

Overall, the proposed method offers more detailed insight in spatial and temporal discharge dynamics while routing a small summer rainstorm to the stream. However, for now application of this method is limited, because a large amount of energy input is needed to create large enough temperature differences in both space and time. In our case, we used only natural temperature

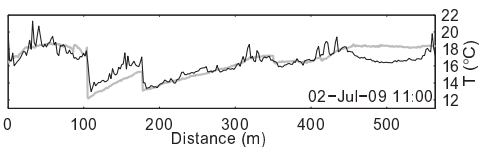

Animation 1: Observed (black line) and simulated (grey line) temperature without hyporheic exchange (see Chapter 5).

variations, which made this method only applicable for a small intensive summer rainstorm, during low initial discharge. To apply this method during higher discharge or less favorable meteorological circumstances, more (artificial) energy input is needed. A possible way forward may be to test this method downstream of a large dam or reservoir.

Animation 2: Observed (black line) and simulated (grey line) temperature with hyporheic exchange (see Chapter 5).

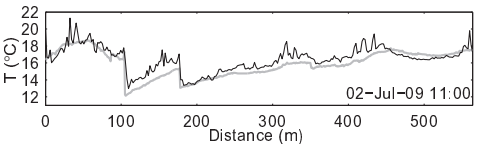

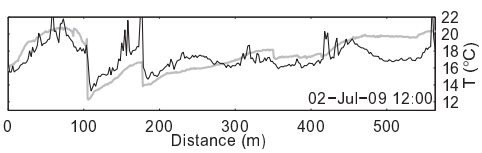

Animation 1: Observed (black line) and simulated (grey line) temperature without hyporheic exchange (see Chapter 5).

Chapter 7

Long term temperature simulations

7.1 Introduction

So far the method has only been applied for a short time frame of maximum two days. Reason for that was that the model was used as a learning tool while it was stepwise improved in an iterative way. To do that, simulation results had to be analysed in great detail and based on these analyses we adapted and reran the model several times. This is labour and time intensive and therefore only applied for short periods of time. Nevertheless, there may be interesting information in longer time series, without performing the detailed analyses as done so far.

In this section we therefore show results of extended simulation periods. Without further calibration two discharge scenarios were run for four different months, with the aim to show the capabilities of the model to simulate longer time series and higher flows and to show the effect of two different a priori determined discharge regimes.

The four different months were chosen based on data availability and quality while they should also present different periods of the year. The months were: March 2008, September 2008, December 2009 and May 2010. This time no calibration was performed and the dicharge profiles (also dynamic in time) were determined a priori: During low flow, when the stream is a net losing stream, the distribution of inflows is similar to the profile described in Chapter (6). During higher flows, when the stream becomes a net gaining stream, we tested two scenarios that differ from each other in the way the gained (difference between initial simulated and observed downstream discharge) water was distributed over the stream.

Scenario 1 The gained water was equally distributed over the four known major lateral inflows (at 104, 178, 350 and 414 m).

Scenario 2 The first lateral inflow (104 m) got 50% of the gained water, while the other three inflows received 16.7% of the gained water.

Animation 2: Observed (black line) and simulated (grey line) temperature with hyporheic exchange (see Chapter 5).

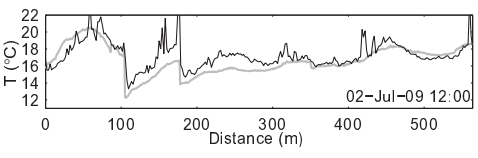

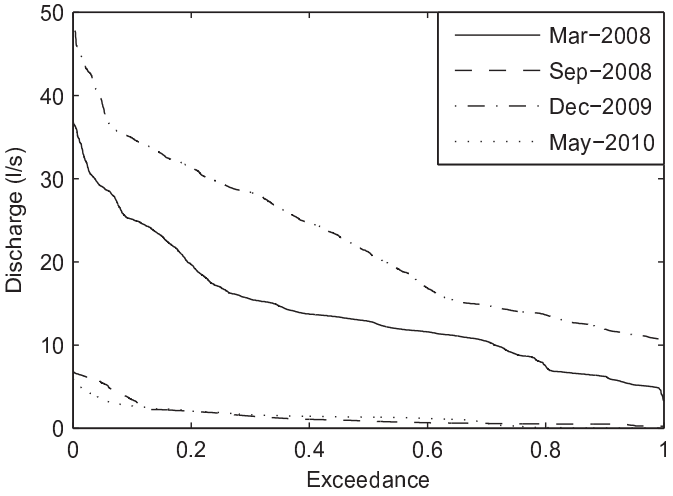

Figure 7.1: Flow duration curves of observed downstream discharge for four different months.

7.2 Comparing two different scenarios

The two months September 2008 and May 2010 both had similar (low) flow regimes (between 0.2 and 7 l s^{-1} as observed at the downstream V-notch weir), while discharge in March 2010 and December 2009 ranged between 3 and 37 l s^{-1} and 10 and 50 l s^{-1}, respectively (Fig. 7.1).

At the upstream and downstream end of the reach, there is no difference in discharge between the two scenarios, but only in-between the lateral inflows and only during periods that the stream was gaining. For all four months, the largest difference in simulated temperature between the two scenarios occured just upstream of the second lateral inflow at 178 m because differences in simulated discharge are largest between the first and second lateral inflow, and thus at the downstream end of this section the simulated temperature differences are the largest as well.

The maximum difference between the two scenarios was 0.3°C for March 2008, 1.0°C for September 2008, 1.3°C for December 2009 and 1.8°C for May 2010. The relatively small difference for the March 2008 simulation is caused by the small energy input during a relative large flow, resulting in small temperature variation over time. The September 2008 and May 2010 simulation show larger differences despite the fact that the discharge profiles between the two scenarios were relatively small. However, discharge was low, making the relative difference much higher. This was then combined with a relative large net energy flux, resulting in these larger differences.

The December 2009 simulation had much larger differences in discharge between the two scenarios, while one may expect small temperature differences due to a low net energy flux during this period. However, large temperature differences between the two scenarios occurred during this month as well. This was caused by the relative warm lateral inflow at 104 m, during a 10 day

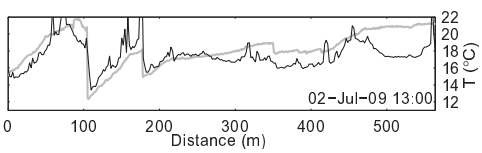

Animation 1: Observed (black line) and simulated (grey line) temperature without hyporheic exchange (see Chapter 5).

period of severe frost. A larger lateral inflow (as in scenario 2) influences the temperature just downstream of the inflow more than a smaller inflow. This caused the differences in simulated temperature: but only when the temperature of the inflow was much higher than the stream water temperature and when discharge from the lateral inflow was significantly different.

7.3 Comparing simulations with observations

Besides the sensitivity of the model to different discharge profiles, we also compared the simulated temperatures with the observed. For all months the RMSE was small (<0.2°C) and only slightly different for different scenarios (Table 7.1). These small differences are mainly caused by the fact that the RMSE is an average over the entire time series and stream length, while differences between the two scenarios are only present during gaining stream conditions and in-between the first and last lateral inflow (between 104 and 414 m). Because the RMSE for the two different scenarios are small, we only discuss temperature simulations obtained with scenario 1.

In Fig. 7.2, observed versus simulated temperature is plotted for all four months at four different locations along the stream. At 80 m, the simulated temperatures matches the observed well, except for the peak temperatures during May-2010 (and in a smaller extend during Sep-2008), which were simulated too high. At 170 m the simulated peak temperatures during May-2010 were too low, while the Dec-2009 simulations were simulated too high during minimum temperatures. At 340 and 540 m fom the upper V-notch weir, the simulated temperatures match the observed well for all months except for Dec-2009, during which the simulated temperatures were also too low in the colder range. Duration curves provide temporal signatures of the temperature and discharge (Fig. 7.3). The relatively large scatter in the high range at 80 and 170 m in May 2010 is less appearent here, indicating that these were biasses possibly linked to timing of peaks.

To explain the mismatches between simulated and observed temperature, one can think of several issues. The simulated discharge is either too high or too low. Small under-, or overestimated discharge has a large influence on temperature simulations, especially when discharge is small

Table 7.1: RMSE of simulated vs. observed temperatures. The RMSE is averaged over all observation points along the stream and over the whole month

	RMSE (°C) Scenario 1	RMSE (°C) Scenario 2
Mar-2008	0.064	0.066
Sep-2008	0.093	0.090
Dec-2009	0.181	0.190
May-2010	0.176	0.183

Animation 2: Observed (black line) and simulated (grey line) temperature with hyporheic exchange (see Chapter 5).

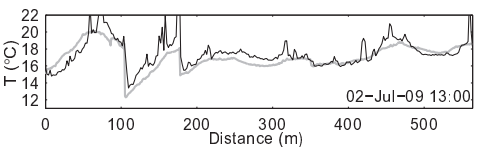

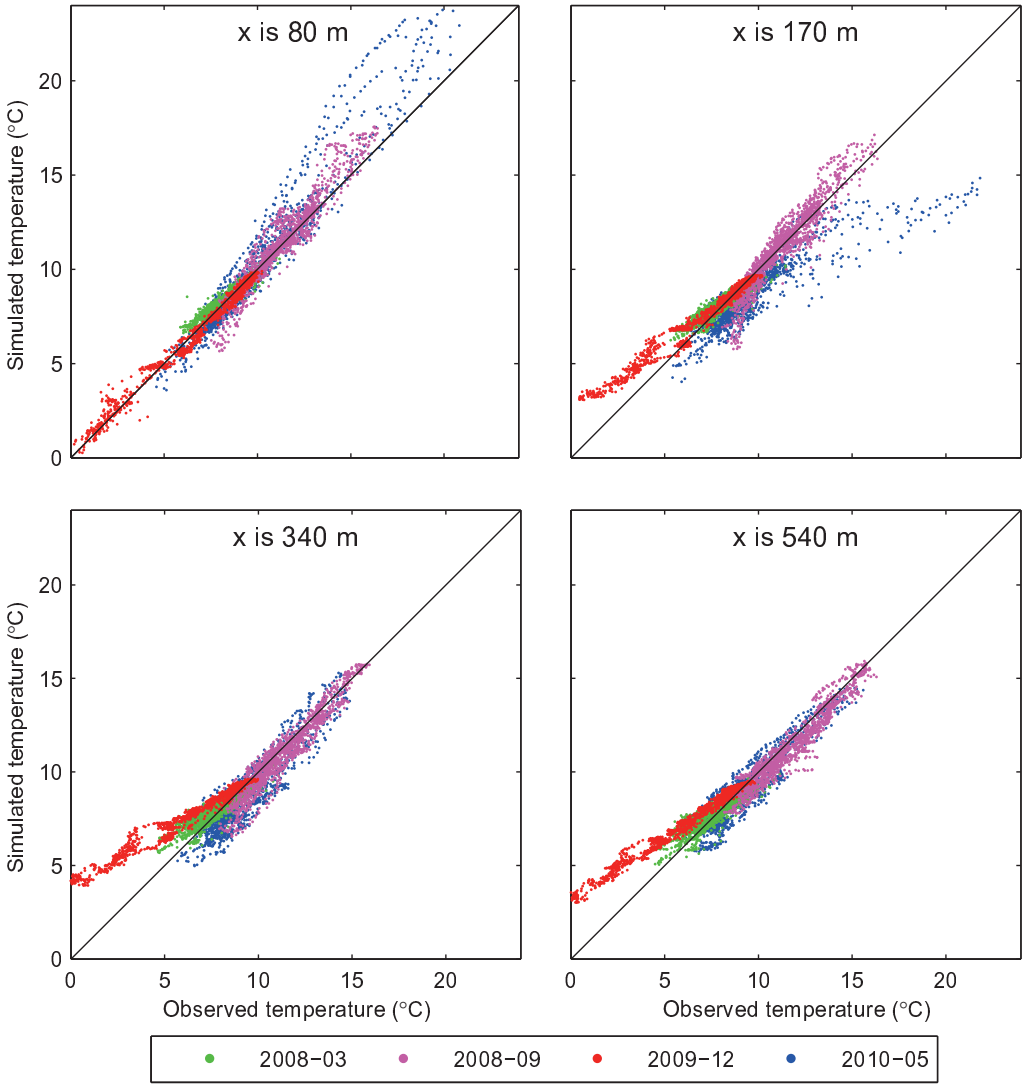

Figure 7.2: Scatter plots of observed vs. simulated temperature at four different locations along the stream for four different months

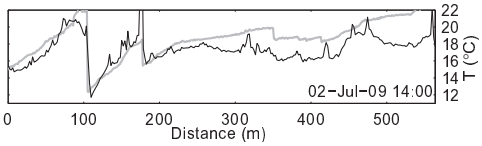

Animation 1: Observed (black line) and simulated (grey line) temperature without hyporheic exchange (see Chapter 5).

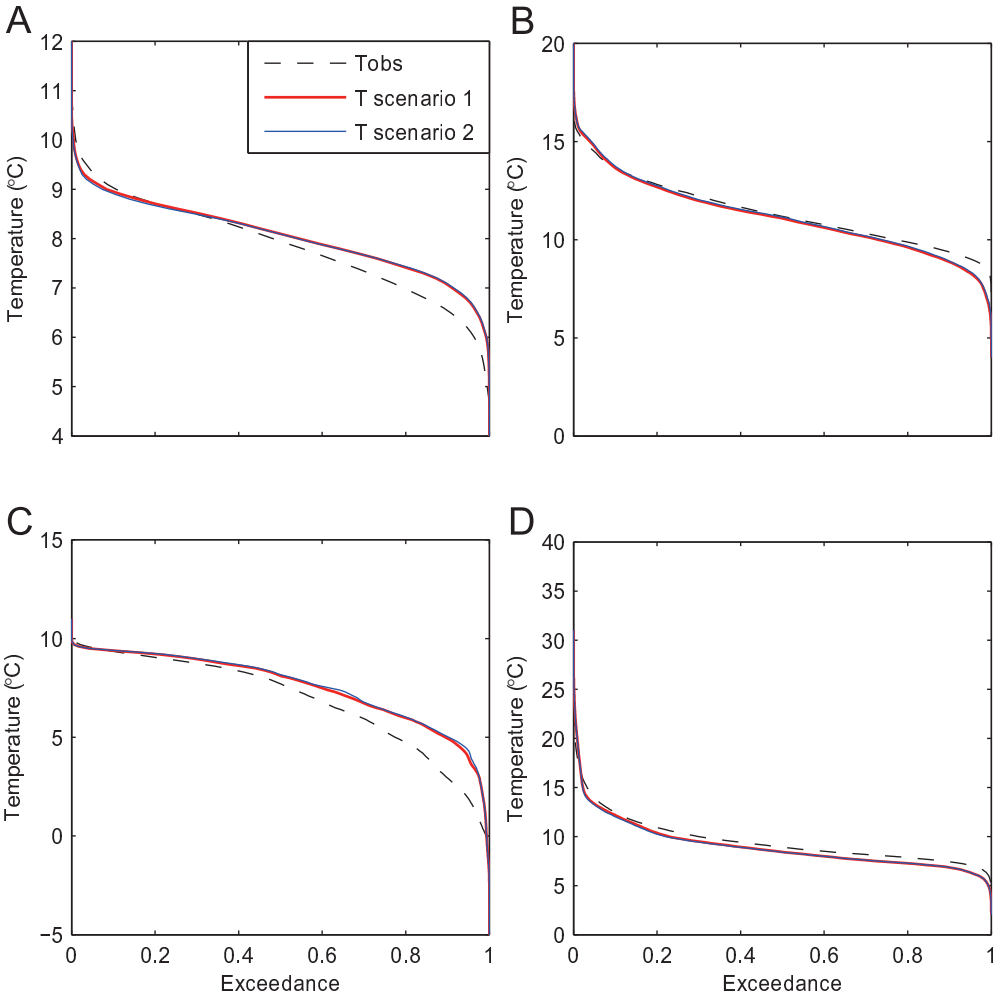

Figure 7.3: Duration curves of observed and simulated temperature for (A) March 2008, (B) September 2008, (C) December 2009 and (D) May 2010

Animation 2: Observed (black line) and simulated (grey line) temperature with hyporheic exchange (see Chapter 5).

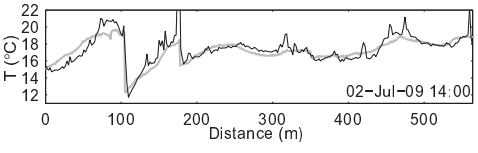

(as during May 2010 and Sep-2008). The overestimated temperature during Dec-2009 is likely caused by the fact that, as explained in Section 7.2, the discharge of the first lateral inflow (at 104 m) was simulated too high. During the cold spell between 12-Dec and 22-Dec the relative warm lateral inflow then results in too high temperatures downstream of this inflow.

There may also be errors in the energy balance. For example in the shadow calculations: there may have been less vegetation cover than the static description derived in August 2008 (as may be the case for May-2010), or in the soil heat flux: e.g. during the cold spell in Dec-2009, it seems that the temperature at 1 m depth was assumed too high.

It could also be that the cable was not submerged everywhere. This was likely the case during the May-2010 simulation, where it seems that at the upstream boundary the cable was not submerged, leading to high observed temperatures at this point that, in the simulations, propagate in downstream direction, but also during the Dec-2009 simulations during which the observed temperatures were below freezing point. In very shallow and slow flowing water it could also be that the cable is heated by direct solar radiation as may be the case during the May 2010 simulations.

Simulations of March 2008 showed the best simulation results in terms of RMSE, which is mainly caused by the fact that discharge was relatively high and energy fluxes were relatively low. This resulted in small temperature fluctuation over time and space which is relatively easy to simulate. However, not much about the hydrological functioning of the catchment can be learned using this methodology, since different water fluxes will only have a minor influence on the in-stream temperature (as shown in section 7.2).

Overall, this analysis shows that, especially when large differences between different scenarios or between observations and simulations occur, it is possible to formulate hypotheses (as we did here) to be able to learn something from the model. This can be about input parameters, such as shadow calculations that changes over the course of a year; quality of the observations, such as direct solar radiation heating the fibre optic cable, or periods when the cable was not submerged; processes the model cannot handle, such as freezing water; and quantification of lateral inflows over time and space, such as the too high lateral inflow at 104 m for the December 2009 simulations. To test these hypotheses, it is recommended to do the analyses on shorter simulation periods than one month, since most of these processes only influence a small period of the time series. This also reduces simulation times significantly.

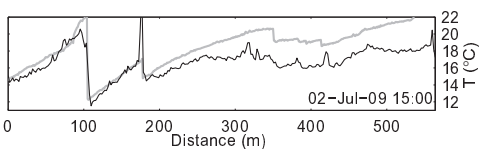

Animation 1: Observed (black line) and simulated (grey line) temperature without hyporheic exchange (see Chapter 5).

Chapter 8

Synthesis and discussion

Hydrology is to a large extent an empirical science, based on observations. Several scientific breakthroughs were triggered by either new measurement techniques or denser observation networks. For example, Anderson and Burt [1978] were one of the first using a network of soil moisture measurements and showed that the hillslope curvature plays an important role in subsurface stormflow. The capability to measure different chemical and isotope tracers led to the important conclusion that in many headwaters pre-event water dominates the hydrograph during peak flow [e.g. Sklash and Farvolden, 1979] while isotope measurements made it possible to estimate mean residence times of groundwater [e.g. McDonnell, 1988].

The new measurement device this thesis deals with is fibre optic Distributed Temperature Sensing (DTS). Although already developed in the 1980's, it was not until 2006 that John Selker introduced this technique in the field of hydrology. During approximately one month, five different hydrological applications were tested showing the large potential of DTS [Selker et al., 2006b].

The opportunities of DTS are large, since temperature contains information on many hydrological states and processes, such as soil moisture, evaporation, groundwater flow, infiltration and stream flow. Due to the high temporal and spatial resolution, it has many advantages above classical point measurements. Most temperature models are calibrated using only a couple of point measurements, while in our case, a single temperature profile shows a large spatial variation in temperature along the stream. For example, by using DTS, Roth et al. [2010] were able to calibrate different parameters in the energy balance model for different land use classes along a stream (such as shading effects and landcover longwave radiation), while classical studies had to use lumped parameters. Hoes et al. [2009] showed the advantage of using DTS for identifying seepage points of upwelling water in canals, since these seepage points are very local and only visible during periods when limited mixing with the canal water occurred.

While these studies were short term campaigns lasting for only a couple of days, we performed the first long term DTS measurements in hydrology, with the aim to quantify subsurface stormflow

Animation 2: Observed (black line) and simulated (grey line) temperature with hyporheic exchange (see Chapter 5).

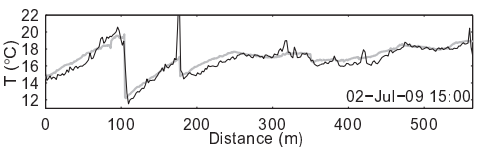

at high spatial and temporal resolution. The more specific objectives (as described in Chapter 1) were:

- To explore opportunities and limitations of DTS in the field of hydrology.
- To model all flow and energy processes (including hyporheic exchange) during steady state flow using combined transport and energy balance models.
- To quantify discharge dynamics during stormflow.

The largest part of this thesis focused on the last two objectives. However, many practical issues had to be solved as well, such as the kind of cable to use, how to calibrate the DTS and how to employ it in the field for a longer period of time. In this synthesis, we discuss some of these practical issues involved when using DTS and we summarize the findings of this thesis. By doing so, quantitative examples are given, to get a better feeling on how much temperature differences or energy exchanges are needed to answer hydrological questions for different stream sizes and accuracy levels.

8.1 Opportunities, set-backs and hands-on experience of DTS

This section describes more practical issues when employing DTS in a stream. Many of these issues came up during field experiments and were often solved by trial and error. Note that my experiences are limited to the Halo DTS device from Sensornet, U.K.

8.1.1 DTS calibration: some experiences

The DTS offers the oppurtunity to perform single-ended or double-ended measurements. Single-ended refers to a setup where only one end of the fibre optic cable is plugged into the DTS desktop computer, while double-ended refers to the case where the cable is looped and both ends are plugged in.

To calibrate the single-ended measurement a minimum of two independent temperature measurements have to be done, preferably at the beginning and at the end of the fibre optic cable. The DTS device offers the opportunity to do this a priori during a calibration run or to update it real-time with independent temperature sensors connected to the DTS device.

During a double-ended measurement, the laser pulse is sent in turn in both directions through the cable, and is then able to correct for the fact that a temperature trace obtained from a pulse sent into one direction should be the same as the trace obtained from a laser pulse send into the other direction. This is especially useful when one cable contains two fibres, which can be connected at the far end of the cable to make a loop. In this setup only a temperature correction has to be done at one place along the cable where temperature is independently measured. Disadvantage of the double-ended measurement is that close to the DTS desktop computer, the

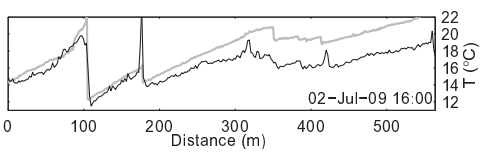

Animation 1: Observed (black line) and simulated (grey line) temperature without hyporheic exchange (see Chapter 5).

precision of the temperature observation is lower than for a single-ended measurement. This is because the cable is twice as long leading to lower precision at the far end of the cable. Since the cable is looped, the temperature at the far end of the cable will then be averaged with the temperature at the beginning of the cable (these are the same part of the cable, depending from which direction the laser pulse was send). However, the accuracy in the middle of the looped cable is higher. The reason why we used single-ended measurements was that the connection at the far end of the cable was poor (this was the point where the two glass fibres of the same cable were connected), resulting in a artificial anomaly in temperature, which resulted in a lower precision, for the double-ended measurement.

While the a priori calibration is sufficient when only relative temperatures are of importance, it is not recommended when absolute temperatures are needed. This is because the calibration parameters appear to vary over time (both for single-ended and double-ended measurements). First of all, the calibration parameters change when the cable is disconnected and connected again. Second, the temperature of the DTS desktop computer itself influences the observed temperature, and third, the difference between the 'true' temperature and the observed DTS temperature changes with higher absolute temperatures. The last issue was observed by comparing five independent temperature loggers (TidbiT), which were placed along the entire length of the cable: the difference between the DTS obtained temperature and the TidbiT obtained temperature varied with absolute temperature. Because of these three issues, it is recommended to calibrate a posteriori with at least two independent point observations of temperature.

At this moment, better ways of calibrating the temperature signal are available. Suárez et al. [2011] described in detail how to calibrate a single-ended measurement, using the Stokes and anti-Stokes signal. In the optimal setup, a cold and warm water bath is needed, where independent temperature sensors measure the temperature. Van de Giesen et al. [In prep.] describes in a similar way how to calibrate double-ended measurements, and how to deal with anomalies in the Stoke or anti-Stoke signal due to sharp bends or other small damages in the cable, which would overcome the problems we encountered when trying double-ended measurements for our setup. However, all data presented in this thesis, is calibrated using five TidbiT temperature sensors (as described in Chapter 2), which is less accurate than the method described by Suárez et al. [2011]. Reason to stay with this method was not to change the calibration method halfway the timeseries to be able to better compare different modelling results. we recognize that the obtained values of parameters such as α or A_{hz} can be slightly different when slightly different temperatures where used for calibrating these parameters, but that does not influence the validity of the used methodology. Nevertheless, in future applications it is advisable to calibrate according to Suárez et al. [2011] or Van de Giesen et al. [In prep.], since a higher accuracy in the observations leads to a more accurate determination of, for example, lateral inflows.

Animation 2: Observed (black line) and simulated (grey line) temperature with hyporheic exchange (see Chapter 5).

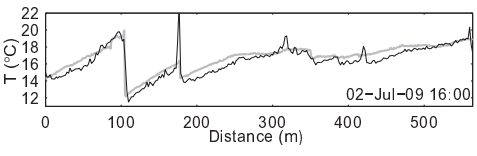

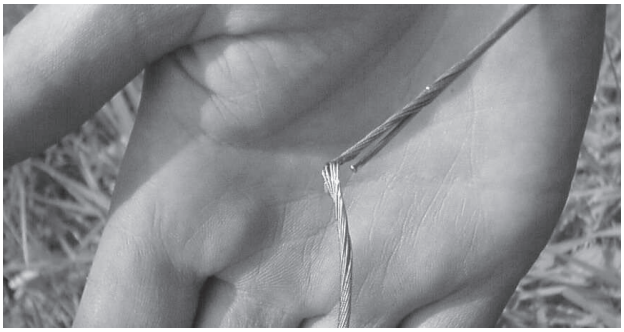

Figure 8.1: Picture of the broken, with stainless-steel inforced fiber optic cable, that was used during the first pilot study [Selker et al., 2006a,b]

8.1.2 Employment of fibre optic cables in the field

Most fibre optic cables are used as communication lines, and are situated underground. However, when employed in streams, requirements for cables are different. The cables should be well protected and preferably easy to handle. In this section some experiences with different cables are shared as well as experiences when maintaining long term measurement campaigns.

During the first pilot studies [Selker et al., 2006a,b], the cable was inforced by stainless-steel housing of 1 mm thickness and wrapped by stainless-steel wires. This cable was employed in a borehole before it was used in the stream. Due to its own weight the cable was slightly stretched and due to the fact that the cable was wrapped in only one direction, the cable tended to coil up automatically. This caused a kink in the cable, causing the solid steel to break, and with it the glass fibre (Fig. 8.1). Fortunately, this happened when removing the cable, just after the experiments had finished.

During the next employment of DTS in the Maisbich, we chose to use a cable without steel, to avoid the experiences we had before. However, to our astonishment, the cable was bitten by animals at a few locations where the cable was out of the water. This experience forced us to use the cable as described in Chapter (2), in which a steel spiral prevents animals from biting the cable, while at the same time the spiral prevents kinks in the cable. Others still use a cable similar to the one used during the first pilot studies, with the difference that the wrapping with steel wires is done in two directions to prevent coiling up of the cable. But the best type of cable also depends on its application. If there is no danger of animals biting the cable, a steel cover may not be needed. This may be the case when the cable is employed underground [e.g. Steele-Dunne et al., 2010] or completely under water [e.g. Roth et al., 2010]. However, a steel cover may be useful in these settings as well, to make the cable heavier or to be able to heat up the cable artificially. When the cable is fully exposed to solar radiation a white and thinner cable may be more feasible. When a higher spatial resolution is required, the cable can be wrapped

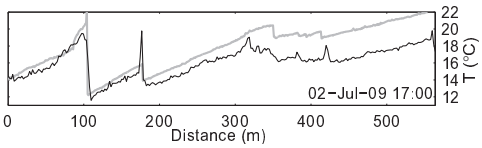

Animation 1: Observed (black line) and simulated (grey line) temperature without hyporheic exchange (see Chapter 5).

around a pole [e.g. Selker et al., 2006b; Vogt et al., 2010; Suárez et al., 2011]. For the same purpose, Brugg Cables, Switzerland, developed a cable in which 10 m of fibre is wrapped in 1 m cable, increasing the spatial resolution with a factor of 10. This is especially useful when employing the cable in a borehole.

In a stream as small as the Maisbich, a lot of maintenance is needed to keep the cable properly submerged. Especially after large discharge events, when relative large loads of rocks and sediment are transported, the cable can be exposed to the air or burried under the streambed sediments. It also happened that large parts of the stream completely dried up during summer, leaving no water in the stream to submerge the cable. Reaches where the cable was exposed to the air can be relatively easily determined since direct solar radiation heats up the cable very fast. As long as the cable is properly submerged, this effect is, according to Neilson et al. [2010] minimal and stays within tenths of degrees C depending on depth, turbidity and flow velocity. However, from my own experience, it appears there is some influence when the cable is in very shallow water (< a few cm). We suspect this because we have witnessed moments when the temperature dropped a few degrees within a few minutes after the stream was in the shadow again. In the cases we suspected this, we only looked if the timing of the increase in simulated temperature was correct and if the simulated temperature was correct just downstream of the stream segment exposed to solar radiation or just after the stream segment was in the shadow again. However, when the effect of direct solar radiation resulted in an observed temperature increase of only a few degrees C, this may have remained unnoticed. But since differences between observed and simulated temperature often exceeded a few tenths of degrees, this would not influence our finding significantly.

Due to the large maintenance needed to keep the cable properly submerged in such a small stream, a relatively large part of the three years timeseries is of poor quality (i.e. parts of the cable measures air temperature or temperature of the riverbed). Because a lot of data is needed for the temperature model, such as temperature of the lateral inflow, discharge and meteorological data, a gap in these observations reduces the total time frame suitable for further analyses. Other gaps in the data were caused by power failure of the DTS device itself. Although the DTS device automatically continues measuring after a power cut, we still encountered periods of many days where the device was (for some inexplicable reasons) switched off.

8.2 Quantifying all flow and energy processes during steady state flow

The second objective of this research was to model all flow and energy processes during steady state flow using a combined transport and energy balance model. Such a transport and energy balance model is needed to interpret the observed temperature signal correctly. In literature, these models have been well described [e.g. Brown, 1969; Sinokrot and Stefan, 1993; Foreman et al., 1997; Kim and Chapra, 1997; Webb and Zhang, 1997; Evans et al., 1998; Webb and Zhang,

Animation 2: Observed (black line) and simulated (grey line) temperature with hyporheic exchange (see Chapter 5).

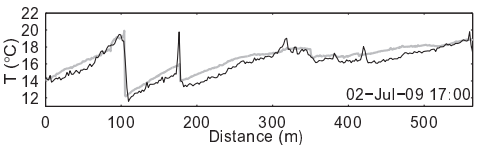

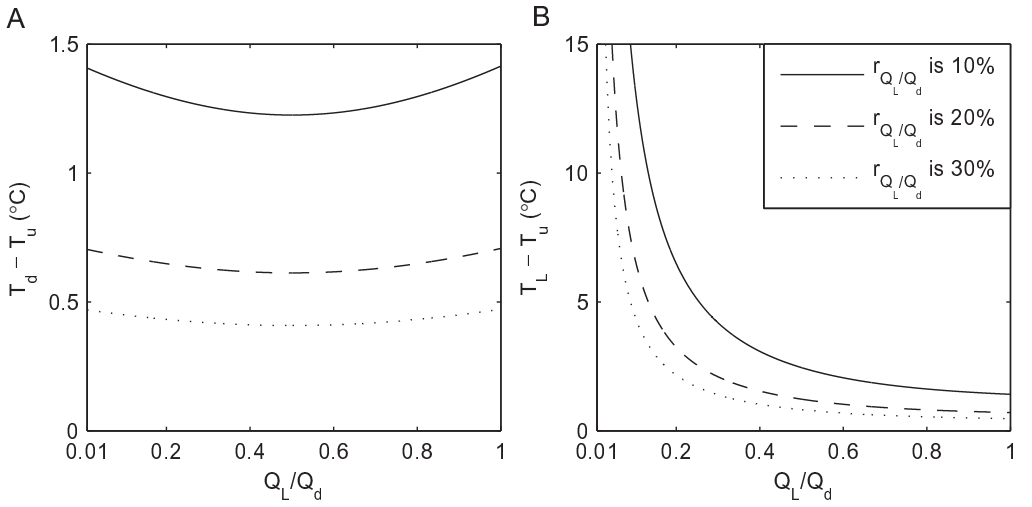

Figure 8.2: Absolute temperature difference between (A) T_d and T_u, and (B) T_L and T_u, that is needed to obtain a contribution of Q_L/Q_d with a relative error $r_{(Q_L/Q_d)}$ of 10, 20 and 30% for a standard deviation 0.1°C in the temperature observations

1999; Bartholow, 2000; Younus et al., 2000; Foreman et al., 2001; Bogan et al., 2003; Boyd and Kasper, 2003; Bogan et al., 2004; Caissie et al., 2007; Westhoff et al., 2007]. However, the high resolution DTS temperature observations require a more detailed and spatially distributed description of lateral inflows, losses or downwelling water, heat transport in the stream and hyporheic exchange fluxes. These issues are discussed in this section.

8.2.1 Quantification of lateral inflows

Lateral inflows can significantly influence in-stream temperature, especially during very warm days or very cold days. During such warm or cold moments, one DTS obtained temperature profile can localize the major lateral inflows, provided that they are large enough to influence the temperature of the stream. When the temperature of an inflow is known as well, the relative contribution of this inflow can be determined with a mass balance (Eq. 3.5), while the relative error (or uncertainty) can be estimated by dividing Eq. (3.6) by Eq. (3.5). As with any other tracer, the lateral inflow should cause a sufficient change in in-stream temperature (or concentration when other tracers are used) to be able to quantify this inflow relative to the downstream discharge with a certain error band.

For example, assuming a standard deviation in temperature observations of 0.1°C, the difference between T_{up} and T_d should be >0.47°C when a maximum relative error r_{Q_L/Q_d} of 30% is allowed (Fig. 8.2A). A relative error of 20% is obtained when the difference between T_{up} and T_d is >0.7°C, while a difference >1.4°C is needed to have relative errors <10%.

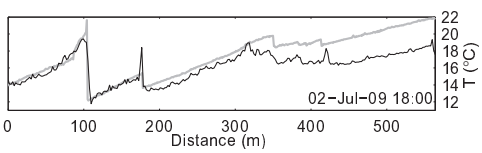

Animation 1: Observed (black line) and simulated (grey line) temperature without hyporheic exchange (see Chapter 5).

The differences between upstream and downstream temperature should be caused by differences between T_L and T_{up}. Fig. 8.2B shows that, to obtain a maximum relative error of 20% in Q_L/Q_d, the difference between T_L and T_{up} should be 14°C when $Q_L = 0.05Q_d$. For a contribution of $Q_L = 0.1Q_d$ this difference should be 6.7°C and a temperature difference of 3.2°C is needed for a contribution of $Q_L = 0.2Q_d$. When the error in the temperature observation are twice as large, the difference between T_L and T_{up} should also be twice as large to obtain the same error in Q_L/Q_d. During steady state discharge conditions, it is possible to identify the moment of largest temperature difference over a day, to reduce the error in Q_L/Q_d.

8.2.2 Quantifying losses of water

In this thesis, losses of water are defined as water that leaves the stream and model boundaries as downwelling water. Small scale hyporheic fluxes that stay within the first meter of the subsurface (as in Chapter 5) is not meant with this definition.

Losses of water are always difficult to identify, since they, in contrast to incoming water, do not influence the concentration or temperature of the water. However, in this thesis we were able to estimate these losses along the stream. An important requirement is that upstream discharge plus all gains and losses should match the observed downstream discharge. Since this requirement alone leads to many possible solutions, a first estimate is needed on where these losses occur. For this, knowledge of the field site is needed.

During the many field visits, two locations were found where the stream completely dried up during very low flow. Knowing the discharge upstream of these losses then gives a first estimate on the minimum water loss at that location. In Chapter (4), the losses were estimated by looking at the tracer recovery after releasing water from a small basin, in combination with mass balances for water and initial tracer concentrations (Eq. 4.7 - 4.9). However, this is only possible when an upstream reservoir with a concervative tracer is released.

Another method was used in Chapter (5). Making use of the fact that a small volume of water heats faster than a large volume, we were able to iteratively optimize the discharge within stream reaches of several tens of meters, where rapid heating of the water was observed when exposed to solar radiation. However, this method only works when enough energy input is available to heat up the stream rapidly. During the low flow conditions as in Chapter (5), the available solar radiation was large enough. However, when discharge increases, solar radiation may not be sufficient anymore.

Another stream loss we did not account for in this thesis is evaporation of stream water. However, this loss is minor: for example, during the relative warm days on 1 and 2-Jul-2009 (the study period used in Chapter 5), the maximum (simulated) loss due to evaporation was 0.013 l s^{-1} at the downstream end of the stream, which is smaller than the accuracy of the discharge

Animation 2: Observed (black line) and simulated (grey line) temperature with hyporheic exchange (see Chapter 5).

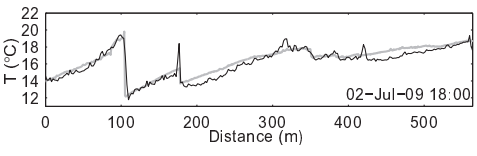

measurements. The change in RMSE of the temperature simulations during this period was <0.003°C.

8.2.3 Heat exchange with in-stream rock clasts

In Chapter (4), we showed that transport of heat was retarded compared to that of diluted salt. Hyporheic exchange and heat exchange with the streambed were not found to be sufficient to fully account for the observed retardation. Therefore we argued that heat exchange with in-stream rock clasts is partly responsible for the retardation. The many small rock clasts present in the stream exchange heat fast enough to assume that the temperature of the rock clasts always equals the stream water temperature, making it possible to simply sum up the cross-sectional area of water and rock clasts.

Abundant in-stream vegetation could have the same effect as in-stream rock clasts. They also store heat and the individual plants have a relative large surface area to exchange heat fast enough to adopt to the stream water temperature, but it will be difficult to measure their cross-sectiona area. However, if the water inbetween the plants is stagnant, one should model it as an extra transient storage. This may be the case is deeper low gradient channel with abundant plant growth. Disadvantage of such an extra transient storage are the more unknown model parameters leading to more equifinality. To limit these extra dregrees of freedom, one can measure these parameters in the field together with their temperatures [e.g. Briggs et al., 2009].

The influence of the in-stream rock clasts on the retardation of heat is most pronounced when there is a large longitudinal temperature gradient in the stream and when solar radiation inputs are relatively small. The longitudinal temperature gradient is needed because without a gradient it is not possible to see the advective velocity of heat. Solar radiation should be relatively low since large energy inputs also changes the water temperature, making it difficult to separate this influence from that of in-stream rock clasts.

In Chapter (4) the amount of rock clasts in the total cross-sectional area was not known a priori, while the cross-sectional area of the stream was simplified as a trapezoidal shape. At that stage in the research, we calibrated the relative amount of in-stream rock clasts of the total cross-sectional area as a constant fraction of 0.35. However, a higher discharge results in a lower fraction of in-stream rock clasts. Therefore, in the Chapters that followed, we used measured cross-sectional areas, including an estimate of the cross-sectional area of the in-stream rock clasts. This made it possible to quantify this fraction a priori for each discharge. In Fig. (8.3) the fraction of in-stream rock clasts is given as an average over the whole stream length for a range of discharge values. A discharge of 6 l s^{-1} corresponds with a fraction of 0.35. In Chapter (4), the pre-event discharge was between 3.2 and 7 l s^{-1} with a peak discharge 4 l s^{-1} higher. Thus the obtained calibrated value in Chapter (4) of 0.35 is in the same range as the a priori determined value using the detailed measurements of the cross-sectional areas (Fig. 8.3).

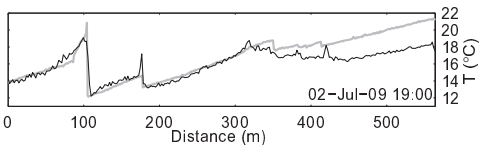

Animation 1: Observed (black line) and simulated (grey line) temperature without hyporheic exchange (see Chapter 5).

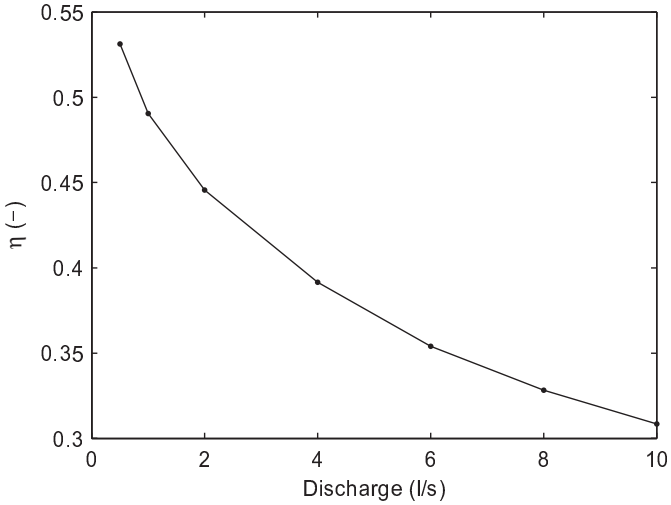

Figure 8.3: Fraction of rockclasts (η) averaged over the whole stream length, for different simulated stream discharges when measurements from the pin-meter are used. Note that the calibrated value of η in Chapter (4) is 0.35. Discharge during this study ranged from 3.2 untill 7 l s^{-1} during baseflow with peak flow $\sim$4 l s^{-1} higher.

8.2.4 Hyporheic exchange

The last water flux we determined during steady state was hyporheic exchange (see Chapter 5). This was done with a top-down approach, where in-stream temperature transport was used to quantify the retardation of heat due to hyporheic exchange. The principles of this method are the same as many other studies that analyze breakthrough curves of an artifically injected tracer [Haggerty et al., 2000, 2002; Gooseff et al., 2003, 2005; Zarnetske et al., 2007], but in our case, solar radiation was the (main) tracer input.

The advantage of using high resolution temperature observations is that the experimental design is more flexible. This is because a certain distance is needed between the location of tracer input and observation point since the timescale of advection should be in the same range as the timescale of hyporheic exchange. The Damkohler number, which is a dimensionless number describing the ratio between hyporheic exchange rate and advection, is used for this and should be between 0.5 and 5 for a good identifiability of hyporheic exchange parameters [Harvey and Wagner, 2000]. The distance between tracer input and observation point (which is one of the parameters in the Damkohler number) depends on experimental design. However, the range of optimal distances depends on hyporheic exchange. Thus only after analyzing the data, it is possible to see if the chosen distances between tracer injection point and observation points are sufficient. Because DTS gives temperatures every 2 m, there are always observation points at a sufficient distance from the tracer injection point.

Animation 2: Observed (black line) and simulated (grey line) temperature with hyporheic exchange (see Chapter 5).

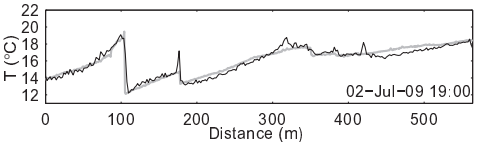

The non-conservative behaviour of temperature is often a disadvantage, but in this case it offers the opportunity to get more insight into the depth of the hyporheic zone below the surface. This is because the temperature of the hyporheic zone also changes over time due to heat conduction within the subsurface. A deeper hyporheic zone (which will then be connected with the stream through preferential flowpaths) will have less influence from surface temperature, and will thus have a more constant temperature than shallow hyporheic zones. Model results showed that most likely the hyporheic zones are located directly under the stream (Chapter 5). This has been assumed in other studies [e.g. Story et al., 2003; Neilson et al., 2009], but never been confirmed before.

The major limitations of the proposed model framework is that only small scale hyporheic exchange can be simulated (i.e. water fluxes that return to the stream within the length of one gridcell). Longer flowpaths have not been accounted for explicitly. Another assumption made is that the hyporheic zone is a well mixed reservoir. Although there are studies indicating that this assumption may be valid for some streams, we could not check it independently, since the model framework is not suitable for modelling other types of residence time distributions. Nevertheless, the proposed method gives a first estimate on hyporheic exchange and its spatial distribution.

8.3 Quantifying discharge dynamics during stormflow

In Chapter (6) we used the model that was calibrated for steady state discharge, to quantify spatial and temporal discharge dynamics during a short intensive summer rainstorm. During this storm a double discharge peak was observed of which the first peak occured during the rainfall, while the second peak started three to four hours later with peak discharge ∼8 hours after the rainstorm. To unravel the discharge dynamics during this stormflow, we used the model as a learning tool, during which we stepwise develloped, tested and either accepted or rejected hypotheses.

During this stormflow we show that the first peak discharge was mainly caused by ‘rain on water’; stream losses increased significantly with higher discharge and lateral inflows remained constant over time. We also show that the dew point temperature gives a good estimate for the temperature of the rain itself.

During the second discharge peak, which started four hours after the rainstorm, we showed that in-between the two V-notch weirs most likely no subsurface stormflow occurred, but that it is likely that a bypass (in this case a side channel) became active, after it had filled and connected to the stream.

The dynamics in hyporheic exchange were also investigated during this summer rainstorm. Best temperature simulation were obtained when between 0 and 250 m from the upstream V-notch weir, hyporheic exchange increases with increasing discharge, while downstream of this point

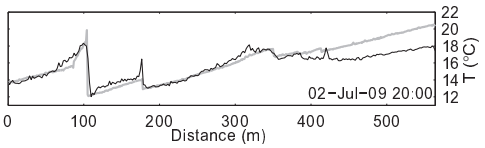

Animation 1: Observed (black line) and simulated (grey line) temperature without hyporheic exchange (see Chapter 5).

best model results were obtained when hyporheic exchange remained at pre-event level. This could be explained by the fact that during higher discharge, the width of the stream increased significantly in the upstream half of the stream, while downstream of 250 m the increase in stream width was less pronounced. In this study, we only tested a linear relationship between hyporheic fluxes and in-stream discharge versus no dynamics at all. We recongnize that a linear relation with in-stream discharge is only one out of many different relations, but it is the first attempt to give a first estimate on the dynamics in hyporheic exchange during a rain event.

Unraveling spatial and temporal discharge dynamics during stormflow is the long term objective of this thesis. However, we were only able to do this for a small summer storm during low flow conditions, where the stream was a net losing stream. During wetter pre-event conditions, or larger rainstorms, the stream becomes a net gaining stream, indicating that more water should come from the hillslopes as subsurface stormflow. Especially the subsurface stormflow during such high flow conditions were targeted in the long term objective. However, during these conditions temperature differences were not large enough to be able to locate and quantify this subsurface stormflow. This is one of the major limitations of our approach.

It would be interresting to see whether the proposed method also works for slightly larger headwaters, where minimum discharge is always larger than 10 l s^{-1}. This has the advantage that the cable will be better submerged, while the assumption of complete mixing over the cross-sectional area is not yet violated. The disadvantage of larger streams is that more energy is needed to heat up the stream to create the necessary temperature differences.

For example: to quantify a lateral inflow of $0.1Q_d$ with a relative error of 20%, a temperature difference between T_{up} and T_L should be $\sim$7°C (see Section 8.2.1). When this difference should be caused by changing the temperature of the main stream, enough energy should be available to do this. The required energy is given by $\Phi = \rho_w c_w Q \Delta T / W$ where Φ is expressed in W m^{-1} per unit stream width. Assuming a stream discharge of 10 l s^{-1} per unit stream width, 293 kW m^{-1} is needed to cause a 7°C temperature change. When solar radiation is used as the main energy source, which can be about 1200 W m^{-2} during summer, a stream length of 244 m should then be exposed to solar radiation. However, during winter or during cloudy conditions which always occur during rainstorms, much less solar radiation reaches the stream. When ice is used to cool down the stream water with 7°C, 0.88 kg s^{-1} of ice is needed. To reach a cold water plateau lasting for 10 min the amount of ice adds up to 530 kg.

8.4 Outlook

Over the last five years, DTS has found its way to the hydrological community. More and more people use it and many different hydrological applications have been found. In all these applications DTS has proven its value due to its high resolution and accuracy.

Animation 2: Observed (black line) and simulated (grey line) temperature with hyporheic exchange (see Chapter 5).

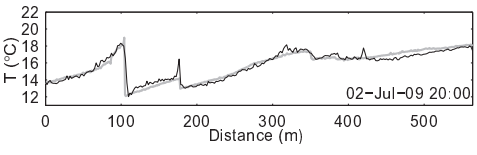

The aim of this research was to use DTS to unravel discharge dynamics in a small headwater. Therefore, we combined a coupled routing and temperature model with high resolution temperature observations. In this thesis, we successfully applied the presented model framework during low flows and warm days. However, temperature fluctuations were too small to apply this method during higher flows. To overcome this problem, improvements should be made in the accuracy in temperature observations or in artificially creating larger temperature fluctuations in the stream.

Already significant progress has been made in getting a higher temperature resolution and accuracy. DTS systems with a spatial resolution of 25 cm are already available while new calibration techniques improve the accuracy, which, in turn, makes it possible to quantify lateral inflows with higher accuracies as well. For example, Suárez et al. [2011] report a resolution of 0.035°C integrated over 5 min for a lab setup. For cables with small damages, as is often the case when employed in the field, Van de Giesen et al. [In prep.] work on calibration techniques that take these damages into account, and thus give more accurate temperature observations. However, this work is still in preparation.

Larger temperature fluctuations could be created by releasing cold or warm water upstream of the stream segment of interest. We described such an experiment in Chapter (4), but one may also think of larger permanent reservoirs: e.g. Toffolon et al. [2010] report temperature increases of 3 to 4°C due to releases from such a reservoir, with stream discharges in the order of 10 m^3 s^{-1}. However, such streams are often no headwater streams and the assumption of a well mixed cross-sectional area may be violated.

Instead of adding a large volume of hot or cold water, one could also try to heat or cool the water by, for example, a large heat exchanger. Because of the large amount of energy that will be needed, innovative ideas are needed to realize such a heat exchanger.

To move away from the disadvantages of temperature (i.e. not conservative and amount of available energy is a limiting factor), one could focus on other natural tracers. A new interesting tracer may be diatoms [Pfister et al., 2009], which are unicellular algea present in and around many fresh water bodies, while different species occur at different wetness levels in the riparian zone. Because they can be easily flushed out during a rainstorm, they can be used to understand spatial patterns in discharge generation. Up to now, it is still too labour intensive to apply this method at larger scale, but future developments may solve this problem.

Conventional tracers, such as ions or isotopes, are not out of play either, be it that they should be measured at higher spatial resolution than traditional studies that measure tracer concentrations at one or two locations along the stream. However, to our knowledge, no devices to measure at high spatial resolution along an entire stream are available yet, other than applying many independent loggers in the stream a few meters apart from each other, which will be very expensive as well as labour intensive. However, more and more devices become available to

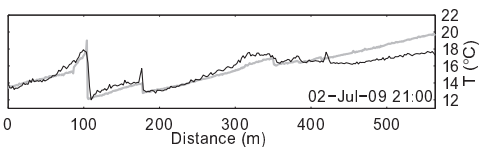

Animation 1: Observed (black line) and simulated (grey line) temperature without hyporheic exchange (see Chapter 5).

analyse chemical [e.g. Sandford et al., 2007; Van der Velde et al., 2010] or isotope [Berman et al., 2009] concentrations at high temporal resolution, making it possible to analyze many samples that may be collected at different places along the stream.

Overall, we believe that new breakthroughs in headwater hydrology will be triggered by high temporal, but especially by high spatial resolution observations. DTS provides such data in the form of temperature. But any other new technique providing high resolution tracer data is more than welcome, and should be tested right away!

Animation 2: Observed (black line) and simulated (grey line) temperature with hyporheic exchange (see Chapter 5).

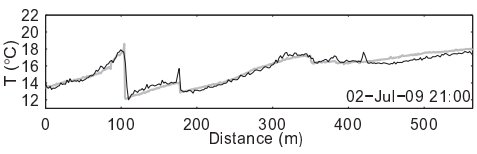

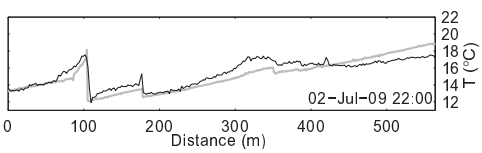

Animation 1: Observed (black line) and simulated (grey line) temperature without hyporheic exchange (see Chapter 5).

Appendix A

Numerical schemes

A.1 Numerical solution routing model

A staggered scheme is used for the numerical implementation of the routing model, where the state values are given at the centre of gridcell i, while the fluxes are determined between the border of two grid cells at e.g. $i + 1/2$. First we write the water balance equation (Eq. 3.1) in discrete form.

$$r_c \frac{V\left\langle \zeta_i^{n+1^{**}} \right\rangle - V\left\langle \zeta_i^{n} \right\rangle}{\Delta t} = Q_{i-1/2}^n - Q_{i+1/2}^n + Q_L^n$$

where V is a function of ζ, i is the current grid cell and n is the current time step at which all states and fluxes are known. Because the cross-section is not rectangular, the volume at the next timestep $V\left\langle \zeta_i^{n+1^{**}} \right\rangle$ should be determined iteratively, until $\zeta_i^{n+1^{**}} = \zeta_i^{n+1^{*}}$. Writing $V\left\langle \zeta_i^{n+1^{**}} \right\rangle$ as $V\left\langle \zeta_i^{n+1^{**}} - \zeta_i^{n+1^{*}} + \zeta_i^{n+1^{*}} \right\rangle$ and writing all states and fluxes at timestep n at the right hand side gives

$$r_c V\left\langle \zeta_i^{n+1^{**}} - \zeta_i^{n+1^{*}} + \zeta_i^{n+1^{*}} \right\rangle = r_c V\left\langle \zeta_i^{n} \right\rangle + \left(Q_{i-1/2}^n - Q_{i+1/2}^n + Q_L^n \right) \Delta t$$

writing $\zeta_i^{n+1^{**}} - \zeta_i^{n+1^{*}}$ as $\Delta\zeta$ yields:

$$r_c V\left\langle \Delta\zeta + \zeta_i^{n+1^{*}} \right\rangle = r_c V\left\langle \zeta_i^{n} \right\rangle + \left(Q_{i-1/2}^n - Q_{i+1/2}^n + Q_L^n \right) \Delta t$$

substituting $V\langle\Delta\zeta\rangle$ by $\Delta\zeta \mathrm{dV}\left\langle \zeta_{\mathrm{i}}^{\mathrm{n+1^{*}}} \right\rangle / \mathrm{d}\zeta$ gives:

$$r_c V\left\langle \zeta_i^{n+1^{*}} \right\rangle + r_c \Delta\zeta \frac{\mathrm{dV}\left\langle \zeta_{\mathrm{i}}^{\mathrm{n+1^{*}}} \right\rangle}{\mathrm{d}\zeta} = r_c V\left\langle \zeta_i^{n} \right\rangle + \left(Q_{i-1/2}^n - Q_{i+1/2}^n + Q_L^n \right) \Delta t$$

when $\mathrm{dV}\left\langle \zeta_{\mathrm{i}}^{\mathrm{n+1^{*}}} \right\rangle / \mathrm{d}\zeta$ is substituted by $A_o\left\langle \zeta_i^{n+1^{*}} \right\rangle$ gives

$$r_c V\left\langle \zeta_i^{n+1^{*}} \right\rangle + r_c \left(\zeta_i^{n+1^{**}} - \zeta_i^{n+1^{*}} \right) A_o\left\langle \zeta_i^{n+1^{*}} \right\rangle = r_c V\left\langle \zeta_i^{n} \right\rangle + \left(Q_{i-1/2}^n - Q_{i+1/2}^n + Q_L^n \right) \Delta t$$

Animation 2: Observed (black line) and simulated (grey line) temperature with hyporheic exchange (see Chapter 5).

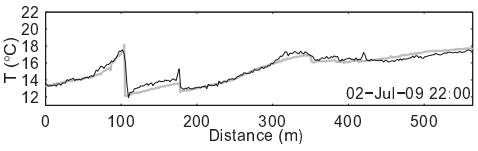

Now we bring $\zeta_i^{n+1^{**}}$ to the left hand side:

$$\zeta_i^{n+1^{**}} = \zeta_i^{n+1^*} + \frac{V\left\langle\zeta_i^n\right\rangle - V\left\langle\zeta_i^{n+1^*}\right\rangle}{A_o\left\langle\zeta_i^{n+1^*}\right\rangle} + \frac{Q_{i-1/2}^n - Q_{i+1/2}^n + Q_L^n}{r_c A_o\left\langle\zeta_i^{n+1^*}\right\rangle}\Delta t \tag{A.1}$$

For $u > 0$, the discharge Q is given by

$$Q_{i-1/2}^n = A\left\langle\zeta_{i-1}^n\right\rangle u_{i-1/2}^{n+\theta} \qquad Q_{i+1/2}^n = A\left\langle\zeta_i^n\right\rangle u_{i+1/2}^{n+\theta} \tag{A.2}$$

where $u^{n+\theta}$ is the 'theta' rule, meaning $\theta u^{n+1} + (1-\theta)u^n$ where θ varies between 0 and 1; a value of 0 results in a fully explicit scheme, a value of 1 results in a fully implicit scheme.

The relation between u and ζ is given by the Saint Venant Equation (Eq. 3.2). In discrete form this becomes [Stelling and Duinmeijer, 2003]

$$\frac{u_{i+1/2}^{n+1} - u_{i+1/2}^n}{\Delta t} + g\frac{\zeta_{i+1}^{n+\theta} - \zeta_i^{n+\theta}}{\Delta x} + C_f\frac{\left|u_{i+1/2}^n\right| u_{i+1/2}^{n+1}}{\overline{R}_{i+1/2}^n} = D_u \tag{A.3}$$

$$D_u = \begin{cases} -\dfrac{1/2u_{i+1/2}^{n^2} - 1/2u_{i-1/2}^{n^2}}{\Delta x} & \text{for } u_{i+1/2} - u_{i-1/2} > \epsilon \\ -\dfrac{1}{\overline{A}_{i+1/2}^n}\left(\dfrac{\overline{Q}_{i+1}^n u_{i+1/2}^n - \overline{Q}_i^n u_{i-1/2}^n}{\Delta x} - u_{i+1/2}^n\dfrac{\overline{Q}_{i+1}^n - \overline{Q}_i^n}{\Delta x}\right) & \text{for } u_{i+1/2} - u_{i-1/2} \le \epsilon \end{cases}$$

where ϵ is an arbitrary value [m/s]. Because A is not known at i+1/2 and Q is not known at i+1, average values are taken ($\overline{A}$ and $\overline{Q}$) which are the averages of the values of half a grid cell upstream and downstream. Applying the theta rule and reorganizing Eq. (A.3) results in

$$u_{i+1/2}^{n+1} = r_{u_{i+1/2}} - a_{u_{i+1/2}}\zeta_i^{n+1} - c_{u_{i+1/2}}\zeta_{i+1}^{n+1} \tag{A.4}$$

with

$$a_{u_{i+1/2}} = \frac{-g\dfrac{\theta}{\Delta x}}{\dfrac{1}{\Delta t} + C_f\dfrac{\left|u_{i+1/2}^n\right|}{\overline{R}_{i+1/2}^n}} \qquad c_{u_{i+1/2}} = \frac{g\dfrac{\theta}{\Delta x}}{\dfrac{1}{\Delta t} + C_f\dfrac{\left|u_{i+1/2}^n\right|}{\overline{R}_{i+1/2}^n}}$$

$$r_{u_{i+1/2}} = \frac{D_u\dfrac{u_{i+1/2}^n}{\Delta t} - \dfrac{(1-\theta)\left(\zeta_{i+1}^n - \zeta_i^n\right)}{\Delta x}}{\dfrac{1}{\Delta t} + C_f\dfrac{\left|u_{i+1/2}^n\right|}{\overline{R}_{i+1/2}^n}}$$

Combining Eq. (A.1), (A.2) and (A.4) gives

$$\zeta_i^{n+1^{**}} = a_{\zeta_i}\zeta_{i-1}^{n+1^*} + b_{\zeta_i}\zeta_i^{n+1^*} + c_{\zeta_i}\zeta_{i+1}^{n+1^*} + C_1 \tag{A.5}$$

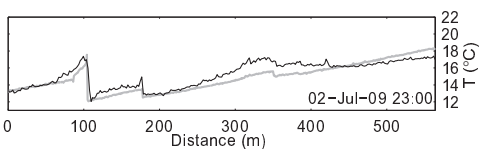

Animation 1: Observed (black line) and simulated (grey line) temperature without hyporheic exchange (see Chapter 5).

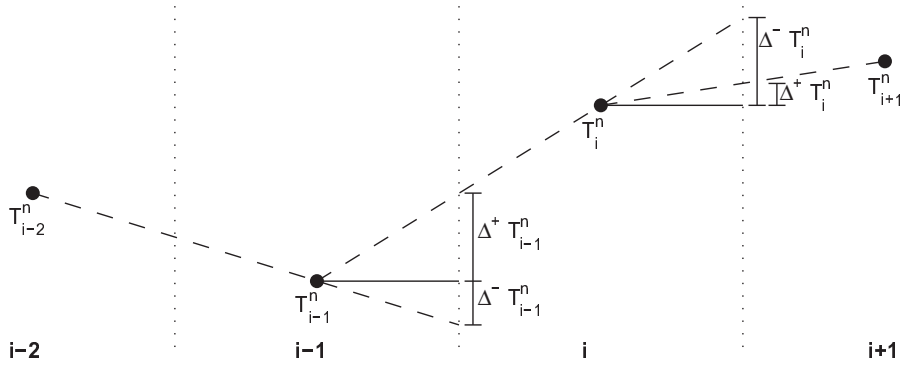

Figure A.1: Visualization of $\Delta^+ T_{i-1}^n$ and $\Delta^- T_{i-1}^n$

with

$$
\begin{aligned}
a_{\zeta_i} &= -\frac{A\left\langle\zeta_{i-1}^n\right\rangle \theta\Delta t}{r_c A_o \left\langle\zeta_i^{n+1^*}\right\rangle} a_{u_{i-1/2}} \\
b_{\zeta_i} &= -\frac{A\left\langle\zeta_{i-1}^n\right\rangle \theta\Delta t}{r_c A_o \left\langle\zeta_i^{n+1^*}\right\rangle} c_{u_{i-1/2}} + \frac{A\left\langle\zeta_i^n\right\rangle \theta\Delta t}{r_c A_o \left\langle\zeta_i^{n+1^*}\right\rangle} a_{u_{i+1/2}} + 1 \\
c_{\zeta_i} &= \frac{A\left\langle\zeta_i^n\right\rangle \theta\Delta t}{r_c A_o \left\langle\zeta_i^{n+1^*}\right\rangle} a_{u_{i-1/2}} \\
C_1 &= \frac{V\left\langle\zeta_i^n\right\rangle - V\left\langle\zeta_i^{n+1^*}\right\rangle}{A_o \left\langle\zeta_i^{n+1^*}\right\rangle} + \frac{A\left\langle\zeta_{i-1}^n\right\rangle \left(\theta r_{u_{i-1/2}} + (1-\theta) u_{i-1/2}^n\right)}{r_c A_o \left\langle\zeta_i^{n+1^*}\right\rangle}\Delta t \\
&\quad - \frac{A\left\langle\zeta_i^n\right\rangle \left(\theta r_{u_{i+1/2}} + (1-\theta) u_{i+1/2}^n\right)}{r_c A_o \left\langle\zeta_i^{n+1^*}\right\rangle}\Delta t + \frac{Q_L}{r_c A_o \left\langle\zeta_i^{n+1^*}\right\rangle}\Delta t
\end{aligned}
$$

When ζ and the cross-sectional profiles are known, Q, u, V, A_o, W and P can be solved with Eq. (A.1), (A.2) and (A.4). Note that the upstream boundary condition $Q_{(i=-1/2)}$ should already be determined in Eq. (A.1).

A.2 Numerical solution transport model

The transport model was solved with an explicit scheme. Writing Eq. (3.3) in discrete form gives

$$
\begin{aligned}
\frac{V_i^{n+1} T_i^{n+1} - V_i^n T_i^n}{\Delta t} &= Q_{i-1/2}^n T_{i-1/2}^n - Q_{i+1/2}^n T_{i+1/2}^n + A_{i-1}^n D \frac{T_{i-1}^n - T_i^n}{\Delta x} \\
&\quad - A_i^n D \frac{T_i^n - T_{i+1}^n}{\Delta x} + \sum Q_{L_i}^n T_{L_i}^n + \frac{W_i^n x_i \Phi_{atm\,i}^n}{\rho_w c_w} + \frac{P_i^n x_i \Phi_{cond\,i}^n}{\rho_w c_w}
\end{aligned}
\tag{A.6}
$$

Animation 2: Observed (black line) and simulated (grey line) temperature with hyporheic exchange (see Chapter 5).

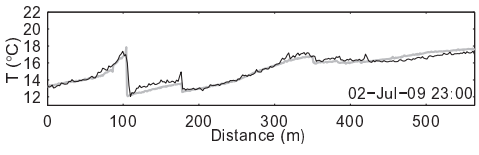

For $Q > 0$, $T^n_{i-1/2}$ and $T^n_{i+1/2}$ are given by:

$$T^n_{i-1/2} = T^n_{i-1} + \Delta T^n_{i-1} \qquad \text{and} \qquad \mathrm{T^n_{i+1/2}} = \mathrm{T^n_i} + \Delta \mathrm{T^n_i} \tag{A.7}$$

where ΔT^n_{i-1} and ΔT^n_i are the temperature gradients between section i and the downstream and upstream section, respectively. They are given by [Van Leer, 1974]:

$$\Delta T^n_{i-1} = \frac{\max(0, \Delta^+ T^n_{i-1}\ \Delta^- T^n_{i-1})}{\Delta^+ T^n_{i-1} + \Delta^- T^n_{i-1}} \qquad \text{and} \qquad \Delta \mathrm{T^n_i} = \frac{\max(0, \Delta^+ \mathrm{T^n_i}\ \Delta^- \mathrm{T^n_i})}{\Delta^+ \mathrm{T^n_i} + \Delta^- \mathrm{T^n_i}}$$

where $\Delta^+ T^n_{i-1}$ and $\Delta^- T^n_{i-1}$ are the interpolated and extrapolated gradients of the downstream and upstream node of section $i-1$ while $\Delta^+ T^n_i$ and $\Delta^- T^n_i$ are the interpolated and extrapolated gradients of the downstream and upstream node of section i (Fig. A.1). Combining Eq. (A.6) and (A.7) gives

$$\begin{aligned} T^{n+1}_i = {} & \frac{V^n_i}{V^{n+1}_i} T^n_i + \frac{Q^n_{i-1/2} T^n_{i-1} - Q^n_{i+1/2} T^n_i}{V^{n+1}_i} \Delta t \\ & + \frac{Q^n_{i-1/2} \Delta T^n_{i-1} - Q^n_{i+1/2} \Delta T^n_i}{V^{n+1}_i} (1 - C_{FL}) \Delta t + \frac{A^n_{i-1} D}{V^{n+1}_i} \frac{T^n_{i-1} - T^n_i}{\Delta x} \Delta t \\ & - \frac{A^n_i D}{V^{n+1}_i} \frac{T^n_i - T^n_{i+1}}{\Delta x} \Delta t + \frac{\sum Q^n_{L\,i} T^n_{L\,i}}{V^{n+1}_i} \Delta t + \frac{W^n_i x_i \Phi^n_{atm\,i}}{\rho_w c_w V^{n+1}_i} \Delta t + \frac{P^n_i x_i \Phi^n_{cond\,i}}{\rho_w c_w V^{n+1}_i} \Delta t \end{aligned}$$

where $C_{FL} = u\mathrm{d}t/\mathrm{d}x$ is the Courant number.

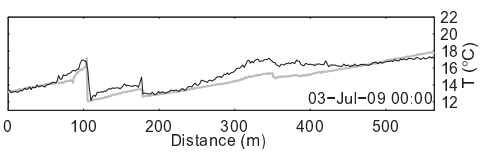

Animation 1: Observed (black line) and simulated (grey line) temperature without hyporheic exchange (see Chapter 5).

References

References

Anderson, J. K., Wondzell, S. M., Gooseff, M. N., Haggerty, R., 2005. Patterns in stream longitudinal profiles and implications for hyporheic exchange flow at the H.J. Andrews Experimental Forest, Oregon, USA. Hydrol. Processes 19 (15), 2931–2949.

Anderson, M. G., Burt, T. P., 1978. The role of topography in controlling throughflow generation. Earth Surface Processes 3 (4), 331–344, http://dx.doi.org/10.1002/esp.3290030402.

Bartholow, J. M., 2000. The Stream Segment and Stream network Temperature Models: A Self-Study Course. US Dept. of the Interior, US Geological Survey, Open-File Report 99-112, (US).

Bartolino, J. R., 2003. The Rio Grande - Competing demands for a desert river. Heat as a Tool for Studying the Movement of Ground Water Near Streams, ed. DA Stonestrom and J. Constantz, 8–16.

Becker, M. W., Georgian, T., Ambrose, H., Siniscalchi, J., Fredrick, K., 2004. Estimating flow and flux of ground water discharge using water temperature and velocity. J. Hydrol. 296 (1-4), 221–233.

Bencala, K. E., Walters, R. A., 1983. Simulation of solute transport in a mountain pool-and-riffle stream: a transient storage model. Water Resour. Res. 19 (3), 718–724.

Berman, E. S. F., Gupta, M., Gabrielli, C., Garland, T., McDonnell, J. J., 2009. High-frequency field-deployable isotope analyzer for hydrological applications. Water Resour. Res. 45 (10), W10201.

Beven, K., 2006. Searching for the holy grail of scientific hydrology: $Q_t = \mathrm{H}(\mathrm{S}, \mathrm{R}, \Delta t)\mathrm{A}$ as closure. Hydrol. Earth Syst. Sci. 10 (5), 609–618, http://www.hydrol-earth-syst-sci.net/10/609/2006/.

Beven, K., Freer, J., 2001. Equifinality, data assimilation, and uncertainty estimation in mechanistic modelling of complex environmental systems using the GLUE methodology. J. Hydrol. 249 (1-4), 11–29.

Bicknell, B. R., Imhoff, J. C., Kittle, J. L., Donigian, A. S., Johanson, R. C., 1997. Hydrological simulation program Fortran: User's manual for version 11 EPA. U.S. Environmental Protection Agency, National Exposure Research Laboratory, Athens, Ga., EPA/600/R-97/080.

Bishop, K., Buffam, I., Erlandsson, M., Fölster, J., Laudon, H., Seibert, J., Temnerud, J., 2008. Aqua incognita: the unknown headwaters. Hydrol. Processes 22 (8), 1239–1242, http://dx.doi.org/10.1002/hyp.7049.

Bishop, K. H., 1991. Episodic increases in stream acidity, catchment flow pathways and hydrograph separation. University of Cambridge.

Blasch, K., Constantz, J., Stonestrom, D. A., 2007. Thermal methods for investigating groundwater recharge. U.S. Geol. Surv. Prof. Pap. 1703, 353 – 376.

Boano, F., Revelli, R., Ridolfi, L., 2007. Bedform-induced hyporheic exchange with unsteady flows. Adv. Water Resour. 30 (1), 148–156.

Boderie, P., Dardengo, L., 2003. Warmtelozing in oppervlaktewater en uitwisseling met de atmosfeer. Report Q3315, WL— Delft Hydraulics.

Bogan, T., Mohseni, O., Stefan, H. G., 2003. Stream temperature-equilibrium temperature relationship. Water Resour. Res. 39 (9), 1245.

Bogan, T., Stefan, H. G., Mohseni, O., 2004. Imprints of secondary heat sources on the stream temperature/equilibrium temperature relationship. Water Resour. Res. 40 (12), W12510.

Bonell, M., 1998. Selected challenges in runoff generation research in forests from the hillslope to headwater drainage basin scale. J. Am. Water Resour. Assoc. 34 (4), 765–785.

Boyd, M., Kasper, B., 2003. Analytical methods for dynamic open channel heat and mass transfer: Methodology for heat source model Version 7.0. Oregon Department of Environmental Quality, Portland, Oregon, http://www.heatsource.info/HeatSourcev7.0.pdf.

Briggs, M. A., Gooseff, M. N., Arp, C. D., Baker, M. A., 2009. A method for estimating surface transient storage parameters for streams with concurrent hyporheic storage. Water Resour. Res. 45, W00D27.

Brookfield, A. E., Sudicky, E. A., Park, Y. J., Conant, B., 2009. Thermal transport modelling in a fully integrated surface/subsurface framework. Hydrol. Processes 23 (15), 2150–2164.

Brown, G. W., 1969. Predicting temperatures of small streams. Water Resour. Res. 5 (1), 68–75.

Burkholder, B. K., Grant, G. E., Haggerty, R., Khangaonkar, T., Wampler, P. J., 2008. Influence of hyporheic flow and geomorphology on temperature of a large, gravel-bed river, Clackamas River, Oregon, USA. Hydrol. Processes 22 (7), 941–953.

Caissie, D., Satish, M. G., El-Jabi, N., 2007. Predicting water temperatures using a deterministic model: Application on Miramichi River catchments (New Brunswick, Canada). J. Hydrol. 336 (3-4), 303–315.

Cardenas, M. B., 2008. Surface water-groundwater interface geomorphology leads to scaling of residence times. Geophys. Res. Lett. 35 (8), L08402.

Cardenas, M. B., 2009. Stream-aquifer interactions and hyporheic exchange in gaining and losing sinuous streams. Water Resour. Res. 45 (6), W06429.

Chanson, H., 2004. Hydraulics of Open Channel Flow (2nd Ed.). ButterworthHeinemann.

Chen, Y. D., Carsel, R. F., McCutcheon, S. C., Nutter, W. L., 1998a. Stream temperature

simulation of forested riparian areas: I. Watershed-scale model development. J. Environ. Eng. 124, 304.

Chen, Y. D., McCutcheon, S. C., Norton, D. J., Nutter, W. L., 1998b. Stream temperature simulation of forested riparian areas: II. Model application. J. Environ. Eng. 124 (4), 316–328.

Choi, J., Harvey, J. W., Conklin, M. H., 2000. Characterizing multiple timescales of stream and storage zone interaction that affect solute fate and transport in streams. Water Resour. Res. 36 (6), 1511–1518.

Constantz, J., 1998. Interaction between stream temperature, streamflow, and groundwater exchanges in alpine streams. Water Resour. Res. 34 (7), 1609–1615.

Constantz, J., 2008. Heat as a tracer to determine streambed water exchanges. Water Resour. Res. 44, W00D10.

Constantz, J., Cox, M. H., Sarma, L., Mendez, G., 2003. The Santa Clara river - the last natural river of Los Angeles. Heat as a Tool for Studying the Movement of Ground Water Near Streams, edited by: Stonestrom DA and Constantz J., USGS Circular 1260, 21–27.

Constantz, J., Thomas, C. L., 1996. The use of streambed temperature profiles to estimate the depth, duration, and rate of percolation beneath arroyos. Water Resour. Res. 32 (12), 3597–3602.

Cozzetto, K., McKnight, D., Nylen, T., Fountain, A., 2006. Experimental investigations into processes controlling stream and hyporheic temperatures, Fryxell Basin, Antarctica. Adv. Water Resour. 29 (2), 130–153.

D'angelo, D. J., Webster, J. R., Gregory, S. V., Meyer, J. L., 1993. Transient storage in Appalachian and Cascade mountain streams as related to hydraulic characteristics. J. N. Am. Benthol. Soc., 223–235.

Dunne, T., Black, R. D., 1970. Partial area contributions to storm runoff in a small New England watershed. Water Resour. Res. 6 (5), 1296–1311.

Evans, E. C., McGregor, G. R., Petts, G. E., 1998. River energy budgets with special reference to river bed processes. Hydrol. Processes 12 (4), 575–595.

Fenicia, F., McDonnell, J. J., Savenije, H. H. G., 2008. Learning from model improvement: On the contribution of complementary data to process understanding. Water Resour. Res. 44 (6), W06419.

Findlay, S., 1995. Importance of surface-subsurface exchange in stream ecosystems: the hyporheic zone. Limnol. Oceanogr. 40 (1), 159–164.

Foreman, M. G. G., James, C. B., Quick, M. C., Hollemans, P., Wiebe, E., 1997. Flow and temperature models for the Fraser and Thompson Rivers. Atmos. Ocean 35 (1), 109–134.

Foreman, M. G. G., Lee, D. K., Morrison, J., Macdonald, S., Barnes, D., Williams, I. V., 2001. Simulations and retrospective analyses of Fraser watershed flows and temperatures. Atmos. Ocean 39 (2), 89–105.

Genereux, D., 1998. Quantifying uncertainty in tracer-based hydrograph separations. Water Resour. Res. 34 (4), 915–919.

Gillham, R. W., 1984. The capillary fringe and its effect on water-table response. J. Hydrol. 67 (1-4), 307 – 324, http://www.sciencedirect.com/science/article/B6V6C-487DBRD-60/2/5031b1ce683f5a5dbc0ae6e0d0d56920.

Gomi, T., Sidle, R. C., Miyata, S., Kosugi, K., Onda, Y., 2008. Dynamic runoff connectivity of overland flow on steep forested hillslopes: Scale effects and runoff transfer. Water Resour. Res. 44 (8), W08411.

Gooseff, M. N., Anderson, J. K., Wondzell, S. M., LaNier, J., Haggerty, R., 2006. A modelling study of hyporheic exchange pattern and the sequence, size, and spacing of stream bedforms in mountain stream networks, Oregon, USA. Hydrol. Processes 20 (11), 2443–2457.

Gooseff, M. N., Hall, R. O., Tank, J. L., 2007. Relating transient storage to channel complexity in streams of varying land use in Jackson Hole, Wyoming. Water Resour. Res. 43 (1), W01417.

Gooseff, M. N., LaNier, J., Haggerty, R., Kokkeler, K., 2005. Determining in-channel (dead zone) transient storage by comparing solute transport in a bedrock channel - alluvial channel sequence, Oregon. Water Resour. Res. 41 (6), W06014.

Gooseff, M. N., Wondzell, S. M., Haggerty, R., Anderson, J., 2003. Comparing transient storage modeling and residence time distribution (RTD) analysis in geomorphically varied reaches in the Lookout Creek basin, Oregon, USA. Adv. Water Resour. 26 (9), 925–937.

Günther, T., Rücker, C., Spitzer, K., 2006. Three-dimensional modelling and inversion of dc resistivity data incorporating topography – II. Inversion. Geophysical Journal International 166 (2), 506–517, http://dx.doi.org/10.1111/j.1365-246X.2006.03011.x.

Ha, K., Koh, D. C., Yum, B. W., Lee, K. K., 2008. Estimation of river stage effect on groundwater level, discharge, and bank storage and its field application. Geosci. J. 12 (2), 191–204.

Habel, F., Bagtzoglou, A. C., 2005. Wave induced flow and transport in sediment beds. J. Am. Water Resour. Assoc. 41 (2), 461–476.

Haggerty, R., McKenna, S. A., Meigs, L. C., 2000. On the late-time behavior of tracer test breakthrough curves. Water Resour. Res. 36 (12), 3467–3479.

Haggerty, R., Wondzell, S. M., Johnson, M. A., 2002. Power-law residence time distribution in the hyporheic zone of a 2nd-order mountain stream. Geophys. Res. Lett. 29 (13), 1640.

Hart, D. R., Mulholland, P. J., Marzolf, E. R., DeAngelis, D. L., Hendricks, S. P., 1999. Relationships between hydraulic parameters in a small stream under varying flow and seasonal conditions. Hydrol. Processes 13 (10), 1497–1510.

Harvey, J., Conklin, M., Koelsch, R., 2003. Predicting changes in hydrologic retention in an evolving semi-arid alluvial stream. Adv. Water Resour. 26 (9), 939–950.

Harvey, J., Wagner, B., Bencala, K., 1996. Evaluating the reliability of the stream tracer approach to characterize stream-subsurface water exchange. Water Resour. Res. 32, 2441–2451.

Harvey, J. W., Bencala, K. E., 1993. The effect of streambed topography on surface-subsurface water exchange in mountain catchments. Water Resour. Res. 29 (1), 89–98.

Harvey, J. W., Wagner, B. J., 2000. Quantifying hydrologic interactions between streams and their subsurface hyporheic zones. Streams and Ground Waters, 344.

Hatch, C. E., Fisher, A. T., Revenaugh, J. S., Constantz, J., Ruehl, C., 2006. Quantifying surface water - groundwater interactions using time series analysis of streambed thermal records: Method development. Water Resour. Res. 42 (10), W10410.

Healy, R. W., 2008. Simulating water, solute, and heat transport in the subsurface with the VS2DI software package. Vadose Zone J. 7 (2), 632.

Hjelmfelt Jr., A. T., Burwell, R. E., 1984. Spatial variability of runoff. J. Irrig. Drain. Eng. 110 (1), 46–54.
URL http://link.aip.org/link/?QIR/110/46/1

Hoes, O. A. C., Luxemburg, W. M. J., Westhof, M. C., van de Giesen, N. C., Selker, J., 2009. Identifying seepage in ditches and canals in ploders in The Netherlands by distributed temperature sensing. Lowland Technology International 11 (2), 21–26.

Jothityangkoon, C., Sivapalan, M., Farmer, D. L., 2001. Process controls of water balance variability in a large semi-arid catchment: downward approach to hydrological model development. J. Hydrol. 254 (1-4), 174–198.

Keery, J., Binley, A., Crook, N., Smith, J. W. N., 2007. Temporal and spatial variability of groundwater-surface water fluxes: Development and application of an analytical method using temperature time series. J. Hydrol. 336 (1-2), 1–16.

Kim, K. S., Chapra, S. C., 1997. Temperature model for highly transient shallow streams. J. Hydraul. Eng. 123 (1), 30–40.

Kirchner, J. W., 2003. A double paradox in catchment hydrology and geochemistry. Hydrol. Processes 17 (4), 871–874, http://dx.doi.org/10.1002/hyp.5108.

Kirkby, M. J., Chorley, R. J., 1967. Throughflow, overland flow and erosion. Hydrol. Sci. J. 12 (3), 5–21.

Klemeš, V., 1983. Conceptualization and scale in hydrology. J. Hydrol. 65 (1-3), 1–23.

Kobayashi, D., 1985. Separation of the snowmelt hydrograph by stream temperatures. J. Hydrol. 76, 155–165.

Kobayashi, D., Ishii, Y., Kodama, Y., 1999. Stream temperature, specific conductance and runoff processes in mountain watersheds. Hydrol. Processes 13, 865–876.

Koberg, G. E., 1964. Methods to compute long-wave radiation from the atmosphere and reflected solar radiation from a water surface. U.S. Geol. Surv. Prof. Pap.

Krause, S., Hannah, D. M., Fleckenstein, J. H., Heppell, C. M., Kaeser, D., Pickup, R., Pinay, G., Robertson, A. L., Wood, P. J., 2010. Inter-disciplinary perspectives on processes in the hyporheic zone. Ecohydrology, In Presshttp://dx.doi.org/10.1002/eco.176.

Kwaad, F. J. P. M., Mücher, H. J., 1977. The evolution of soils and slope deposits in the luxembourg ardennes near wiltz. Geoderma 17 (1), 1 – 37, http://www.sciencedirect.com/science/article/B6V67-489YMBG-27/2/be7d2ad489f938ccbbd9169ce36fd7fa.

Lal, A. M. W., 2001. Modification of canal flow due to stream-aquifer interaction. J. Hydraul. Eng. 127 (7), 567–576.

Lapham, W. W., 1989. Use of temperature profiles beneath streams to determine rates of vertical ground-water flow and vertical hydraulic conductivity. U.S. Geol. Surv. Water-Supply Pap. 2337.

Legrand-Marcq, C., Laudelout, H., 1985. Longitudinal dispersion in a forest stream. J. Hydrol. 78 (3-4), 317–324.

Loheide II, S. P., Gorelick, S. M., 2006. Quantifying stream - aquifer interactions through the analysis of remotely sensed thermographic profiles and in situ temperature histories. Environ. Sci. Technol. 40 (10), 3336–3341.

Lowry, C. S., Walker, J. F., Hunt, R. J., Anderson, M. P., 2007. Identifying spatial variability of groundwater discharge in a wetland stream using a distributed temperature sensor. Water Resour. Res. 43 (10), 10408.

Maxwell, R. M., Chow, F. K., Kollet, S. J., 2007. The groundwater-land-surface-atmosphere connection: Soil moisture effects on the atmospheric boundary layer in fully-coupled simulations. Adv. Water Resour. 30 (12), 2447–2466.

McDonnell, J. J., 1988. The age, origin and pathway of subsurface stormflow in a steep humid headwater catchment. Ph.D. thesis, University of Canterbury. Department of Geography, http://hdl.handle.net/10092/3746.

McDonnell, J. J., 1990. A rationale for old water discharge through macropores in a steep, humid catchment. Water Resour. Res. 26 (11), 2821–2832.

McDonnell, J. J., 2003. Where does water go when it rains? Moving beyond the variable source area concept of rainfall-runoff response. Hydrol. Processes 17 (9), 1869–1875, http://dx.doi.org/10.1002/hyp.5132.

Meier, W., Bonjour, C., West, A., Reichert, P., 2003. Modeling the effect of water diversion on the temperature of mountain streams. J. Environ. Eng. 129, 755.

Moffett, K. B., Tyler, S. W., Torgersen, T., Menon, M., Selker, J. S., Gorelick, S. M., 2008. Processes controlling the thermal regime of saltmarsh channel beds. Environ. Sci. Technol. 42 (3), 671–676.

Monteith, J. L., 1981. Evaporation and surface temperature. Q. J. R. Meteorolog. Soc. 107 (451), 1–27.

Morin, G., Cluis, D., Couillard, D., Jones, G., Gauthier, J., 1983. Modélisation de la température de l'eau à l'aide du modèle quantité-qualité CEQUEAU. Tech. rep., Scientific Report 153, Sainte-Foy: Que: INRS-Eau.

Morrice, J. A., Valett, H. M., Dahm, C. N., Campana, M. E., 1997. Alluvial characteristics, groundwater-surface water exchange and hydrological retention in headwater streams. Hydrol. Processes 11 (3), 253–267.

Neilson, B. T., Hatch, C. E., Ban, H., Tyler, S. W., 2010. Solar radiative heating of fiber-optic cables used to monitor temperatures in water. Water Resour. Res. 46, W08540.

Neilson, B. T., Stevens, D. K., Chapra, S. C., Bandaragoda, C., 2009. Data collection methodology for dynamic temperature model testing and corroboration. Hydrol. Processes 23 (20), 2902–2914.

Niswonger, R. G., Prudic, D. E., Pohll, G., Constantz, J., 2005. Incorporating seepage losses into the unsteady streamflow equations for simulating intermittent flow along mountain front streams. Water Resour. Res. 41 (6), W06006.

Noell, U., Wießner, C., Ganz, C., Westhoff, M., 2011. Direct observations of surface water-groundwater interaction using electrical resistivity tomography. IAHS Publ. 345, 42–47.

Pfister, L., McDonnell, J. J., Wrede, S., Hlúbiková, D., Matgen, P., Fenicia, F., Ector, L., Hoffmann, L., 2009. The rivers are alive: on the potential for diatoms as a tracer of water source and hydrological connectivity. Hydrol. Processes 23 (19), 2841–2845, http://dx.doi.org/10.1002/hyp.7426.

Poole, G. C., Berman, C. H., 2001. An ecological perspective on in-stream temperature: natural heat dynamics and mechanisms of human-caused thermal degradation. Environmental Management 27, 787–802.

Ragan, R. M., 1968. An experimental investigation of partial area contributions. Proc Berne Symp, Int Assoc Sci Hydrol Publ.

Retter, M., Kienzler, P., Germann, P. F., 2006. Vectors of subsurface stormflow in a layered hillslope during runoff initiation. Hydrol. Earth Syst. Sci. 10 (3), 309–320, hESS.

Rice, K. C., Hornberger, G. M., 1998. Comparison of hydrochemical tracers to estimate source contributions to peak flow in a small, forested, headwater catchment. Water Resour. Res. 34 (7), 1755–1766.

Roth, T. R., Westhoff, M. C., Huwald, H., Huff, J. A., Rubin, J. F., Barrenetxea, G., Vetterli, M., Parriaux, A., Selker, J. S., Parlange, M. B., 2010. Stream temperature response to three riparian vegetation scenarios by use of a distributed temperature validated model. Environ. Sci. Technol. 44 (6), 2072–2078.

Rothuizen, R., 2010. From rainfall to runoff: Hydrological processes resulting in threshold behaviour and low rainwater contribution in rapid subsurface flow. Master's thesis, Delft Universtiy of Technology, http://www.citg.tudelft.nl/live/pagina.jsp?id=50e40a94-07c2-4ccc-a3e9-849c85ecbfd0&lang=en.

Rücker, C., Günther, T., Spitzer, K., 2006. Three-dimensional modelling and inversion of dc resistivity data incorporating topography – i. Modelling. Geophysical Journal International 166 (2), 495–505.
URL http://dx.doi.org/10.1111/j.1365-246X.2006.03010.x

Runkel, R. L., 1998. One-dimensional transport with inflow and storage (OTIS): A solute transport model for streams and rivers. U.S. Geol. Surv. Water-Resources Investigation Report 98, 4018.

Sandford, R., Exenberger, A., Worsfold, P., 2007. Nitrogen cycling in natural waters using in situ, reagentless UV spectrophotometry with simultaneous determination of nitrate and nitrite.

Environ. Sci. Technol. 41 (24), 8420–8425, http://www.scopus.com/inward/record.url?eid=2-s2.0-37249038613&partnerID=40&md5=5b070fb05104f854d1365692cacfcb49.

Savenije, H. H. G., 2010. HESS Opinions"Topography driven conceptual modelling (FLEX-topo)". Hydrol. Earth Syst. Sci. 14 (12), 2681–2692, http://www.hydrol-earth-syst-sci.net/14/2681/2010/.

Schmid, B. H., 2008. Can longitudinal solute transport parameters be transferred to different flow rates? J. Hydrol. Eng. 13 (6), 505–509.

Schmid, B. H., Innocenti, I., Sanfilippo, U., 2010. Characterizing solute transport with transient storage across a range of flow rates: The evidence of repeated tracer experiments in Austrian and Italian streams. Adv. Water Resour. 33 (11), 1340 – 1346.

Seibert, J., McDonnell, J. J., 2002. On the dialog between experimentalist and modeler in catchment hydrology: Use of soft data for multicriteria model calibration. Water Resour. Res. 38 (11), 1241.

Selker, J., van de Giesen, N., Westhoff, M., Luxemburg, W., Parlange, M. B., 2006a. Fiber optics opens window on stream dynamics. Geophys. Res. Lett. 33 (24), L24401.

Selker, J. S., Thvenaz, L., Huwald, H., Mallet, A., Luxemburg, W., van de Giesen, N., Stejskal, M., Zeman, J., Westhoff, M., Parlange, M. B., 2006b. Distributed fiber-optic temperature sensing for hydrologic systems. Water Resour. Res. 42 (12), W12202.

Shanley, J. B., Peters, N. E., 1988. Preliminary observations of streamflow generation during storms in a forested Piedmont watershed using temperature as a tracer. J. Contam. Hydrol. 3, 349–365.

Silliman, S. E., Ramirez, J., McCabe, R. L., 1995. Quantifying downflow through creek sediments using temperature time series: one-dimensional solution incorporating measured surface temperature. J. Hydrol. 167 (1-4), 99–119.

Sinokrot, B. A., Stefan, H. G., 1993. Stream temperature dynamics: Measurements and modeling. Water Resour. Res. 29 (7), 2299–2312.

Sivapalan, M., Blöschl, G., Zhang, L., Vertessy, R., 2003. Downward approach to hydrological prediction. Hydrol. Processes 17 (11), 2101–2111.

Sklash, M. G., Farvolden, R. N., 1979. The role of groundwater in storm runoff. J. Hydrol. 43 (1-4), 45 – 65.

St-Hilaire, A., Morin, G., El-Jabi, N., Caissie, D., 2000. Water temperature modelling in a small forested stream: implication of forest canopy and soil temperature. Can. J. Civ. Eng. 27, 1095–1108.

Stallman, R. W., 1965. Steady one-dimensional fluid flow in a semi-infinite porous medium with sinusoidal surface temperature. J. Geophys. Res. 70, 2821–2827.

Steele-Dunne, S. C., Rutten, M. M., Krzeminska, D. M., Hausner, M., Tyler, S. W., Selker, J., Bogaard, T. A., van de Giesen, N. C., 2010. Feasibility of soil moisture estimation using passive distributed temperature sensing. Water Resour. Res. 46 (3), W03534.

Stelling, G. S., Duinmeijer, S. P. A., 2003. A staggered conservative scheme for every Froude

number in rapidly varied shallow water flows. Int. J. Numer. Methods Fluids 43 (12), 1329–1354.

Story, A., Moore, R. D., Macdonald, J. S., 2003. Stream temperatures in two shaded reaches below cutblocks and logging roads: downstream cooling linked to subsurface hydrology. Can. J. For. Res. 33 (8), 1383–1396.

Suárez, F., Aravena, J. E., Hausner, M. B., Childress, A. E., Tyler, S. W., 2011. Assessment of a vertical high-resolution distributed-temperature-sensing system in a shallow thermohaline environment. Hydrol. Earth Syst. Sci. 15 (3), 1081–1093, urlhttp://www.hydrol-earth-syst-sci.net/15/1081/2011/.

Taniguchi, M., Sharma, M. L., 1990. Solute and heat transport experiments for estimating recharge rate. J. Hydrol. 119 (1-4), 57–69.

Toffolon, M., Siviglia, A., Zolezzi, G., 2010. Thermal wave dynamics in rivers affected by hydropeaking. Water Resour. Res. 46 (8), W08536.

Tromp-van Meerveld, H. J., James, A. L., McDonnell, J. J., Peters, N. E., 2008. A reference data set of hillslope rainfall-runoff response, Panola Mountain Research Watershed, United States. Water Resour. Res. 44 (6), W06502.

Tromp-van Meerveld, H. J., McDonnell, J. J., 2006a. Threshold relations in subsurface stormflow: 1. A 147-storm analysis of the Panola hillslope. Water Resour. Res. 42 (2), W02410.

Tromp-van Meerveld, H. J., McDonnell, J. J., 2006b. Threshold relations in subsurface stormflow: 2. The fill and spill hypothesis. Water Resour. Res. 42 (2), W02411.

Tyler, S. W., Selker, J. S., Hausner, M. B., Hatch, C. E., Torgersen, T., Thodal, C. E., Schladow, S. G., 2009. Environmental temperature sensing using Raman spectra DTS fiber-optic methods. Water Resour. Res. 45, W00D23.

Uchida, T., Tromp-van Meerveld, I., McDonnell, J. J., 2005. The role of lateral pipe flow in hillslope runoff response: an intercomparison of non-linear hillslope response. J. Hydrol. 311 (1-4), 117–133.

Uhlenbrook, S., Hoeg, S., 2003. Quantifying uncertainties in tracer-based hydrograph separations: a case study for two-, three- and five-component hydrograph separations in a mountainous catchment. Hydrol. Processes 17 (2), 431–453, http://dx.doi.org/10.1002/hyp.1134.

Van de Giesen, N., Hatch, C., Tyler, S., Selker, J., Janssen, J., Hoes, O., de Jong, S., In prep. Field calibration of distributed temperature sensing for environmental applications. Sensors.

Van den Bos, R., Pfister, L., Matgen, P., 2006. Conceptual modelling of individual HRU's as a trade-off between bottom-up and top-down modelling, a case study. In: Proceedings of the iEMSs Third Biennial Meeting: "Summit on Environmental Modelling and Software". International Environmental Modelling and Software Society, Burlington, USA. http://www.iemss.org/iemss2006/papers/s12/9_vandenBos_3.pdf.

Van der Velde, Y., Rozemeijer, J. C., de Rooij, G. H., van Geer, F. C., Broers, H. P., 2010. Field-scale measurements for separation of catchment discharge into flow route contribu-

tions. Vadose Zone J. 9 (1), 25–35, http://www.scopus.com/inward/record.url?eid=2-s2.0-77349107667&partnerID=40&md5=bb4acc1519c434a66c01d9af73aa5b51.

Van Leer, B., 1974. Towards the ultimate conservative difference scheme. II. Monotonicity and conservation combined in a second-order scheme. J. Comput. Phys. 14 (4), 361–370.

Vogt, T., Schneider, P., Hahn-Woernle, L., Cirpka, O. A., 2010. Estimation of seepage rates in a losing stream by means of fiber-optic high-resolution vertical temperature profiling. J. Hydrol. 380 (1-2), 154 – 164, http://www.sciencedirect.com/science/article/pii/S0022169409006921.

Voss, C., Provost, A., 2002. SUTRA - a model for saturated-unsaturated variable-density ground-water flow with solute or energy transport. U.S. Geol. Surv. Water-Resources Investigation Report 2002-4231.

Ward, A. S., Gooseff, M. N., Singha, K., 2010. Imaging hyporheic zone solute transport using electrical resistivity. Hydrol. Processes 24 (7), 948–953.

Webb, B. W., Zhang, Y., 1997. Spatial and seasonal variability in the components of the river heat budget. Hydrol. Processes 11 (1), 79–101.

Webb, B. W., Zhang, Y., 1999. Water temperatures and heat budgets in Dorset chalk water courses. Hydrol. Processes 13 (3), 309–321.

Weiler, M., Naef, F., Leibundgut, C., 1998. Study of runoff generation on hillslopes using tracer experiments and a physically-based numerical hillslope model. IAHS Publ. 248, 353–362.

Westhoff, M. C., Bogaard, T. A., Savenije, H. H. G., 2010. Quantifying the effect of in-stream rock clasts on the retardation of heat along a stream. Adv. Water Resour. 33 (11), 1417–1425.

Westhoff, M. C., Bogaard, T. A., Savenije, H. H. G., 2011. Quantifying spatial and temporal discharge dynamics of an event in a first order stream, using distributed temperature sensing. Hydrol. Earth Syst. Sci. 15 (6), 1945–1957, http://www.hydrol-earth-syst-sci.net/15/1945.

Westhoff, M. C., Gooseff, M. N., Bogaard, T. A., Savenije, H. H. G., 2011 (*accepted*). Quantifying hyporheic exchange at high spatial resolution using natural temperature variations along a first order stream. Water Resour. Res.

Westhoff, M. C., Savenije, H. H. G., Luxemburg, W. M. J., Stelling, G. S., van de Giesen, N. C., Selker, J. S., Pfister, L., Uhlenbrook, S., 2007. A distributed stream temperature model using high resolution temperature observations. Hydrol. Earth Syst. Sci. 11 (4), 1469–1480, http://www.hydrol-earth-syst-sci.net/11/1469.

Wondzell, S. M., 2006. Effect of morphology and discharge on hyporheic exchange flows in two small streams in the Cascade Mountains of Oregon, USA. Hydrol. Processes 20 (2), 267–287, http://dx.doi.org/10.1002/hyp.5902.

Wondzell, S. M., LaNier, J., Haggerty, R., 2009. Evaluation of alternative groundwater flow models for simulating hyporheic exchange in a small mountain stream. J. Hydrol. 364 (1-2), 142–151.

Woods, R., Rowe, L., 1996. The changing spatial variability of subsurface flow across a hillside. J. Hydrol. (N.Z.) 35 (1), 51–86.

Wörman, A., Wachniew, P., 2007. Reach scale and evaluation methods as limitations for transient storage properties in streams and rivers. Water Resour. Res. 43 (10), W10405.

Wroblicky, G. J., Campana, M. E., Valett, H. M., Dahm, C. N., 1998. Seasonal variation in surface-subsurface water exchange and lateral hyporheic area of two stream-aquifer systems. Water Resour. Res. 34 (3), 317–328.

Younus, M., Hondzo, M., Engel, B. A., 2000. Stream temperature dynamics in upland agricultural watersheds. J. Environ. Eng. 126 (6), 518–526.

Zarnetske, J. P., Gooseff, M. N., Brosten, T. R., Bradford, J. H., McNamara, J. P., Bowden, W. B., 2007. Transient storage as a function of geomorphology, discharge, and permafrost active layer conditions in Arctic tundra streams. Water Resour. Res. 43 (7), W07410.

Zehe, E., Sivapalan, M., 2009. Threshold behaviour in hydrological systems as (human) geo-ecosystems: manifestations, controls, implications. Hydrol. Earth Syst. Sci. 13 (7), 1273–1297, http://www.hydrol-earth-syst-sci.net/13/1273/2009/.

Acknowledgments

During the course of my PhD, many people helped me either directly or indirectly. They helped me with fieldwork, modelling, writing, developing ideas. Sometimes they just listened to the problems I was facing or they just gave joy to my life by being a good friend or colleague.

First of all I would like to thank Huub and Thom. Huub: you gave me the opportunity to do a PhD. You supported (most) of my ideas and let me free to chose my own way. Your enthusiasm inspired me and you always had, or made, time for me when I needed it. You always asked the right questions when I got stuck and the suggestions you made were extremely useful. Besides being an excellent supervisor, I also enjoyed the beers we drank together, and the stories about history, politics or anything else.

Thom: you joined our group shortly after I started my PhD and became my co-supervisor. During my PhD, you were my first help line. I enjoined the discussions about how to do my fieldwork or how to construct my results into a paper. These discussions were often longer than intended and you always listened carefully to my arguments - a quality that many people (especially politicians) miss. You helped me with several field campaigns with great enthusiasm while sweat was dropping from your nose. They say that PhD students start looking like their supervisor. I am not sure if this is true, but I would be happy if it were you to look like!

Although Huub was my supervisor, it was Nick who introduced the fibre optic DTS to me. Nick: many thanks for that and for all other help, ideas trips and cynical jokes. It was all a pleasure to me.

I would also like to thank Wim and Miriam. You both joined me many times during fieldwork. Wim: you already introduced me to the fieldwork in Luxembourg during my BSc thesis and this was the first time it crossed my mind that science could be fun. I will remember the many rides with you to Luxembourg and the fun we always had. Miriam: you also helped me a lot with fieldwork. Especially in the beginning of my PhD, when I did not have my own car, you drove so often to the Maisbich that I had to buy my own car to save our friendship and any other help. During the visits in Luxembourg we spent many nights together in a caravan where we exchanged all gossips and jokes. Although some people complain that we always make the same jokes, I am sure that I shall miss them.

I am also very grateful to Mike Gooseff. After we met for only one day, you agreed to host me at Penn State for two months. The many discussions with you on how to include hyporheic exchange into my model really pushed my research forward. Also many thanks to Adam, Alisha, Christa, George, Joe, Keith and Tom for showing me around in State College.

Jeff McDonnell and John Selker: thanks for all your input and advice during the course of my PhD and already during my MSc. Your enthusiasm and energy are unbeatable. It inspired me a lot!

Nuria, you were also good company in Luxembourg. You invited me to BBQs or other events in Luxembourg and I abused your large hospitality by inviting myself to sleep on your sofa. Your presence made my stays in Luxembourg more colourful.

I would also like to thank the whole Geohydrosystems and land-use management group of the CRP Gabriel Lippmann. Many times I borrowed equipment and your doors were always open for me to work a day in the office or to quickly check my email. Laurent, Hugo, Rudi, Mara, Sebastian, Jeff, Saskia: your hospitality made me feel at home.

My temperature model wouldn't have been the way it is without the help of Guus Stelling. You helped me at an early stage with the numerical implementation of my model and taught me about limiters and 'theta' methods. Due to your help, numerical schemes are no magic to me anymore.

Also many thanks to the municipality of Ettelbruck for allowing us to use the house at the Rückhaltebecken to store our equipment. And a special thanks to Guy Backendorf for always being very helpful. I am also grateful to Jean-Paul Meyrer for allowing us to install all kind of equipment on his field.

Furthermore I would like to thank all my colleagues in Delft for the informal but excellent working environment. Hanneke and Betty: thanks for being my first help advisor for all kinds of paperwork. Martine, Dominica, Cai, Meng, Kazmi and Faisal for sharing an office with. I am sorry for all the curses I shouted out while struggling with Matlab. And many thanks to all who helped me in the field. The list will be too long (and the risk too high to forget someone) to publish here.

And last but not least I would like to thank my girlfriend. Chantal: thank you for your love and unconditional support. Even during the struggles with my last chapters, a single thought about you made me smile. I am happy and proud to have you by my side during my new job in Karlsuhe.

About the author

Martijn Westhoff was born on February 9, 1981 in Zwolle, the Netherlands. After finishing high school, he came to Delft University of Technology to study Civil Engineering where he received his BSc in 2005. During his MSc he specialized in the field of hydrology and received his MSc degree in 2006. During his entire study period he was an active member of the International Association of Civil Engineering Students (IACES), of which 3 years as a board member. He has done his internship in Ghana, where he looked for solutions to store water for agricultural use. For his MSc thesis he spend two months in Luxembourg at the Centre de Recherge Public - Gabriel Lippmann. During this thesis he was one of the first in the hydrological community to use Distributed Temperature Sensing to measure stream water temperature. For his thesis he built a distributed temperature model which he compared with the high resolution temperature observations obtained with this new technique.

Immediately after Martijn received his MSc degree he started his PhD on the same topic as his MSc thesis, with the aim to use temperature as tracer to distinguish between different runoff processes. During his PhD he carried out abundant fieldwork in the Maisbich in Luxembourg, and he did field experiments in Lausanne, Switzerland and Wagga Wagga, Australia. He spent two months at Penn State university, PA, USA, where he worked on determining hyporheic exchange using temperature as tracer. He followed a field work course at Oregon State University, a masterclass on rainfall runoff processes, and two short courses on 'Tracer Hydrology' and 'How to write (and publish) a scientific paper in hydrology'. He visited several international conferences such as EGU, AGU, ERB and HydroPredict. In 2008 he won the Young Scientist Outstanding Poster Prize (YSOPP) at the EGU, Vienna.

Since 2006, Martijn was one of the supervisors of the yearly fieldwork course in Luxembourg, where MSc students learned to perform hydrological measurements. Every year he was guest lecturer for the MSc courses 'Hydrological measurements' and 'Water quality management' and he supervised several students during their BSc or MSc thesis.

After finalizing his PhD, Martijn will join the group of Erwin Zehe, KIT Karlsruhe, where he will work on implementing the principle of 'maximum entropy production' as a self organizing principle into hydrological models.

Publications

Westhoff, M. C., Gooseff, M. N., Bogaard, T. A., Savenije, H. H. G., 2011 (*accepted*). Quantifying hyporheic exchange at high spatial resolution using natural temperature variations along a first order stream. Water Resour. Res

Noell, U., Wießner, C., Ganz, C., Westhoff, M., 2011. Direct observations of surface water-groundwater interaction using electrical resistivity tomography. IAHS Publ. 345, 42–47

Westhoff, M. C., Bogaard, T. A., Savenije, H. H. G., 2011. Quantifying spatial and temporal discharge dynamics of an event in a first order stream, using distributed temperature sensing. Hydrol. Earth Syst. Sci. 15 (6), 1945–1957, `http://www.hydrol-earth-syst-sci.net/15/1945`

Westhoff, M. C., Bogaard, T. A., Savenije, H. H. G., 2010. Quantifying the effect of in-stream rock clasts on the retardation of heat along a stream. Adv. Water Resour. 33 (11), 1417–1425

Roth, T. R., Westhoff, M. C., Huwald, H., Huff, J. A., Rubin, J. F., Barrenetxea, G., Vetterli, M., Parriaux, A., Selker, J. S., Parlange, M. B., 2010. Stream temperature response to three riparian vegetation scenarios by use of a distributed temperature validated model. Environ. Sci. Technol. 44 (6), 2072–2078

Hoes, O. A. C., Luxemburg, W. M. J., Westhof, M. C., van de Giesen, N. C., Selker, J., 2009. Identifying seepage in ditches and canals in ploders in The Netherlands by distributed temperature sensing. Lowland Technology International 11 (2), 21–26

Westhoff, M. C., Savenije, H. H. G., Luxemburg, W. M. J., Stelling, G. S., van de Giesen, N. C., Selker, J. S., Pfister, L., Uhlenbrook, S., 2007. A distributed stream temperature model using high resolution temperature observations. Hydrol. Earth Syst. Sci. 11 (4), 1469–1480, `http://www.hydrol-earth-syst-sci.net/11/1469`

Selker, J., van de Giesen, N., Westhoff, M., Luxemburg, W., Parlange, M. B., 2006a. Fiber optics opens window on stream dynamics. Geophys. Res. Lett. 33 (24), L24401

Selker, J. S., Thvenaz, L., Huwald, H., Mallet, A., Luxemburg, W., van de Giesen, N., Stejskal, M., Zeman, J., Westhoff, M., Parlange, M. B., 2006b. Distributed fiber-optic temperature sensing for hydrologic systems. Water Resour. Res. 42 (12), W12202

Graphic design: josestolk.nl